

Selenium isotope and S-Se-Te elemental systematics along the Pacific-Antarctic ridge: Role of mantle processes

Aierken Yierpan ^{a,*}, Stephan König ^a, Jabrane Labidi ^{a,b}, Ronny Schoenberg ^{a,c}

^a Isotope Geochemistry, Department of Geosciences, Eberhard Karls University of Tübingen, Wilhelmstrasse 56, 72074 Tübingen, Germany

^b Department of Earth, Planetary, and Space Sciences, University of California Los Angeles, Los Angeles, CA, USA

^c Department of Geology, University of Johannesburg, P.O. Box 524, Auckland Park 2006, South Africa

* Corresponding author (*E-mail*: aierken.yierpan@uni-tuebingen.de; *Tel.*: +49-(0)7071-29-78907)

Abstract

The selenium stable isotope system emerges as a new potential tracer of volatile origin and evolution in the terrestrial planets. Accurate determination of the mantle Se isotope composition requires an assessment of Se isotopic behavior in magmatic processes and potential variations across all mantle reservoirs. Here we report the first high-precision Se isotope compositions and Se–Te abundances of a suite of basaltic glasses from the Pacific–Antarctic ridge. These MORBs display a narrow range in $\delta^{82/76}\text{Se}$ values (deviation of $^{82}\text{Se}/^{76}\text{Se}$ relative to NIST SRM 3149) between $-0.30 \pm 0.09\text{‰}$ and $-0.05 \pm 0.09\text{‰}$, with an average of $-0.16 \pm 0.13\text{‰}$ (2 s.d., $n = 27$). We quantify the main processes relevant to MORB petrogenesis in order to better understand the Se–Te elemental behavior in the mantle and investigate if these are systematically related to Se isotope variations.

We show that both Se isotopes and S–Se–Te abundances of MORB melts remain unaffected by assimilation of high-temperature hydrothermal fluids and sulfides, whereas the latter has been shown to overprint the $^{34}\text{S}/^{32}\text{S}$ ratios. MORB differentiation involving sulfide segregation (sulfide liquid and monosulfide solid solution) significantly fractionates Se and Te (Se/Te ratio ~ 45 to 190), with no systematic Se isotope variation. The Se–Te contents of the primary MORB melt corrected for magmatic differentiation can be successfully reproduced by near-fractional decompression melting of a mantle with 170–200 $\mu\text{g g}^{-1}$ S (as sulfide liquid), which has either (1) “fertile lherzolite-like” Se–Te contents (80 ± 17 and $11 \pm 1.7 \text{ ng g}^{-1}$, respectively; 1 s.d.) or (2) distinctly lower Se ($49 \pm 11 \text{ ng g}^{-1}$) and Te ($3.5 \pm 1.3 \text{ ng g}^{-1}$) contents depending on the choice of experimental partition coefficients published by different studies. Regardless, our model shows that Se–Te systematics of “fertile” lithospheric peridotites preserve little primary melt depletion signatures and reflect significant, if not complete, metasomatic overprinting. Finally, based on the observed negligible Se isotopic fractionation between sulfide phase and silicate melt, we suggest that MORBs preserve their mantle source isotopic signature ($\delta^{82/76}\text{Se} = -0.16 \pm 0.13\text{‰}$). Our MORB average is similar within uncertainty to chondritic values but

35 significantly lighter than previously published $\delta^{82/76}\text{Se}$ data for basalts from a variety of geodynamic settings.
36 The subtle but significant Se isotope variation observed within the investigated MORB suite (up to $\sim 0.25\%$) and
37 between other mantle samples analyzed so far may reflect intrinsic source heterogeneity and potential isotopic
38 differences across various mantle reservoirs.

39 **1. Introduction**

40 The current primitive mantle (PM) abundances of the moderately volatile and chalcophile elements
41 Se ($\sim 80 \text{ ng g}^{-1}$) and Te ($\sim 11 \text{ ng g}^{-1}$) are 35–45 times lower compared to the Earth's general volatile depletion
42 trend (McDonough and Sun, 1995; Allègre et al., 2001; McDonough, 2003; Wang and Becker, 2013; Palme and
43 O'Neill, 2014). Because extrapolation of metal–silicate partitioning experiments at 1–19 GPa to core formation
44 conditions predicts near-complete Se–Te removal from the silicate mantle (Rose-Weston et al., 2009), the mantle
45 abundances of Se–Te, together with that of S, have been explained to be established by a chondritic late veneer
46 addition after core formation (Morgan, 1986; McDonough and Sun, 1995; Rose-Weston et al., 2009; Wang and
47 Becker, 2013). However, the non-chondritic $^{34}\text{S}/^{32}\text{S}$ ratio of the mantle and recent S partitioning experiments
48 suggest that a major fraction of mantle S budget reflects metal–silicate equilibration (Labidi et al., 2013; Suer et
49 al., 2017). Meanwhile, it has been debated whether the broadly-chondritic relative abundances of S–Se–Te in
50 lherzolites are representative of the PM composition (Wang and Becker, 2013) since these samples from the
51 lithospheric mantle are often considered metasomatized, especially by Se–Te-rich base metal sulfides and
52 associated platinum-group minerals (Lorand and Alard, 2010; Lorand et al., 2003, 2004, 2010; Luguet et al.,
53 2003, 2004, 2015; König et al., 2014, 2015; Harvey et al., 2015). In this context, mantle-derived melts such as
54 mid-ocean ridge basalts (MORBs) may provide a complementary and broader picture regarding the composition
55 of the asthenospheric mantle, provided that Se–Te elemental behavior in mantle processes is well constrained.

56 There are only few studies concerning Se and/or Te elemental systematics in MORB (Hertogen et al., 1980;
57 Yi et al., 2000; Jenner et al., 2010, 2015; Lissner et al., 2014). Because of their strong partitioning into base
58 metal sulfides (Guo et al., 1999; Hattori et al., 2002; Peach et al., 1990; Barnes et al., 2009; Patten et al., 2013;
59 Brenan, 2015; Kiseeva et al., 2017), Se–Te abundances and ratios in basaltic melts are strongly controlled by
60 sulfide phase–silicate melt partitioning (Hertogen et al., 1980; Lissner et al., 2014). Hertogen et al. (1980) first
61 observed distinctly higher Se/Te ratios and broadly similar Te contents in worldwide MORBs compared to
62 mantle rocks and suggested a higher apparent compatibility of Te relative to Se during partial melting. This
63 appears consistent with observations from lherzolites, pyroxenites (Wang et al., 2013; Wang and Becker, 2013,
64 2015a), and sulfides in sub-arc mantle xenoliths (Hattori et al., 2002) but inconsistent with observations from
65 refractory harzburgites and platinum group minerals (König et al., 2012, 2014, 2015). Lissner et al. (2014)
66 investigated the Se–Te systematics in enriched- and depleted-MORBs from a restricted section of the southern
67 Mid-Atlantic Ridge and suggested an incompatible behavior of both elements and a higher incompatibility of Te
68 during partial melting. This relative partitioning seems to be reversed during magmatic differentiation (Lissner

69 et al., 2014). These observations might be partly attributed to contrasting relative partitioning of Se–Te in
70 different sulfide phases and platinum-group minerals (e.g., Helmy et al., 2010; Liu and Brenan, 2015; Brenan,
71 2015; König et al., 2015) during different mantle processes. Previous evidence for Se and Te behavior in MORB
72 petrogenesis remains ambiguous and warrants further work.

73 On the other hand, Se isotopes might provide new perspectives on the origin of S–Se–Te as well as other
74 highly siderophile or volatile elements on Earth. Due to analytical difficulties (e.g., Yierpan et al. 2018), only
75 few studies reported Se isotope composition ($\delta^{82/76}\text{Se}$; deviation of $^{82}\text{Se}/^{76}\text{Se}$ relative NIST SRM 3149) of mantle
76 rocks/melts, which are limited to geological reference materials (Rouxel et al., 2002; Kurzawa et al., 2017;
77 Yierpan et al., 2018). Compared to the chondrite average $\delta^{82/76}\text{Se}$ of $-0.30 \pm 0.39\%$ (Vollstaedt et al., 2016) and
78 $-0.21 \pm 0.31\%$ (2 s.d.; Labidi et al., 2018), previously analyzed basalts ($n = 9$) and one peridotite show heavier
79 $\delta^{82/76}\text{Se}$ with some marginal overlap. Labidi et al. (2018) reported resolvable mass-dependent Se isotope
80 variations among main chondrite groups, ranging between $-0.40 \pm 0.07\%$ (enstatite chondrite) and $-0.01 \pm 0.09\%$
81 (CI-chondrite). Recent high-precision Se isotope analyses on a small number of different basalts show a rather
82 restricted range in $\delta^{82/76}\text{Se}$ ($+0.21 \pm 0.15\%$, $n = 4$; Kurzawa et al., 2017; Yierpan et al., 2018). These rocks
83 originate from a variety of geodynamic settings and cover a wide range of Se contents ($\sim 15\text{--}170 \text{ ng g}^{-1}$) and
84 Se/Te ratios ($\sim 3\text{--}65$), indicating various mantle sources and/or igneous differentiation histories (Yierpan et al.,
85 2018). It thus remains unclear whether their $\delta^{82/76}\text{Se}$ values readily represent a mantle source signature.

86 In this study, we present the first Se isotope compositions and new Se–Te abundances for a total of 27 fresh
87 MORB glasses collected from the Pacific–Antarctic ridge (65–56°S and 53–41°S). Compared to the sampling
88 areas in previous Se–Te studies (Hertogen et al., 1980; Lissner et al., 2014), these ridge sections are free of
89 plume influence and represent melts derived from a source with first-order major element homogeneity (Vlastélic
90 et al., 2000; Moreira et al., 2008; Hamelin et al., 2010). It is thus an ideal sample set for (1) better understanding
91 Se–Te elemental behavior during mantle processes using recently published experimental sulfide–silicate melt
92 partitioning data and (2) investigating effects of such processes on potential Se isotope fractionation in order to
93 constrain the isotopic composition of the depleted mantle.

94 **2. Samples and geological background**

95 We have analyzed 27 on-axis MORB glasses from two sections of the Pacific–Antarctic ridge (PAR): 65–
96 56°S ($n = 10$) and 53–41°S ($n = 17$) (Supplementary Fig. S1). These samples were collected from the PAR by
97 the French research vessel *L'Atalante* during the cruises PACANTARCTIC 1 (65–56°S; Géli et al., 1997;
98 Vlastélic et al., 1999) and PACANTARCTIC 2 (53–41°S; Klingelhoefer et al., 2006; Moreira et al., 2008;
99 Hamelin et al., 2010). The PAR extends southward from the southern end of the Juan Fernandez microplate at
100 35°S, 110°W (Francheteau et al., 1987) to the Macquarie triple junction at 62°S, 161°E (Falconer, 1972). The
101 studied ridge sections are located to the north of the Vacquier Fracture Zone (FZ; $\sim 53^\circ\text{S}$) and south of Udintsev
102 FZ ($\sim 56\text{--}57^\circ\text{S}$; Supplementary Fig. S1), respectively, with the Eltanin FZ System in between (Watts et al., 1988;

103 Géli et al., 1997; Castillo et al., 1998). The northern section is separated by the Menard FZ (~50°S), which is the
104 major geological feature along the sampling area (Hamelin et al., 2010). Two ridge sections have half-spreading
105 rates of 46–50 mm/year between 52 and 42°S (Lonsdale, 1994) and 27–37 mm/year between 65 and 55°S
106 (Hamelin et al., 2010). The northern ridge section is one of the fastest spreading mid-ocean ridges (Moreira et
107 al., 2008) and, therefore, shows a uniform axial high morphology along the crest (Klingelhoefer et al., 2006). In
108 contrast, the southern section (slow to intermediate spreading ridge) displays variable axis morphologies, ranging
109 from axial valley to axial high (Vlastélic et al., 2000; Ondréas et al., 2001). The oceanic crust beneath the PAR
110 is estimated to be 6–7 km (Adams, 1964).

111 Previous analyses of He, Sr, Nd, Hf, and Pb isotopes show that the studied PAR sections are free from any
112 plume-ridge interactions and reflect a regional-scale first-order mantle source homogeneity (Vlastélic et al., 1999,
113 2000; Moreira et al., 2008; Hamelin et al., 2010, 2011). However, the ridge sections display clear latitudinal
114 variations of radiogenic isotopes, with gradually increasing recycled crust component northwards (Hamelin et
115 al., 2011). This is interpreted to be a subtle yet intrinsic source heterogeneity resulting from progressive mixing
116 of a depleted MORB mantle and recycled oceanic crust. Besides, almost all PAR samples have experienced
117 contamination by Cl-rich brines and/or hydrothermally altered crust during low-pressure magmatic
118 differentiation, which results in significantly heavier S isotope composition if it is associated with hydrothermal
119 sulfide assimilation (Clog et al., 2013; Labidi et al., 2014; Bezaud et al., 2016).

120 **3. Analytical methods**

121 **3.1. Selenium isotope and Se–Te elemental analyses**

122 Most of the studied PAR basalts are in the form of fresh glass fragments. A few samples have plagioclase
123 phenocrysts (<3 mm) and slightly altered yellowish crusts. After they were crushed, fresh chips (1–5 mm) were
124 picked, washed with 18.2 MΩ·cm water in an ultrasonic bath and ground to fine powders. At least 2.5 g sample
125 was used for grinding in order to preclude any potential effect of sample heterogeneity (Wang et al., 2015;
126 Yierpan et al., 2018). One sample (PAC2 DR01-1) is represented by both glass rims and pillow interior, which
127 were processed and analyzed separately.

128 All analyses were conducted at the University of Tübingen. Selenium isotope and Se–Te concentrations
129 were determined from the same sample digest. Details of the chemistry and instrumental procedures are given
130 in Kurzawa et al. (2017) and Yierpan et al. (2018). Briefly, Se contents of most sample unknowns were first
131 determined via isotope dilution by estimating a spike–sample ratio of ~1 based on a general Se vs MgO or S
132 trend previously shown for MORB (Lissner et al., 2014). For this procedure, only ~0.025 g of sample was
133 digested and analyzed directly after separating Fe (see below; but with 2.5 mL resin and 6 N HCl). After Se
134 content was determined, ~0.15–0.4 g of sample was mixed with ⁷⁴Se–⁷⁷Se double spike and ¹²⁵Te single spike
135 to yield Se and Te spike–sample ratios of ~1 and ~0.6–1, respectively. Samples were then digested in a HF–
136 HNO₃ mixture at 85°C and evaporated at 65°C. This is followed by heating in 6 N HCl at 130°C and complete

137 evaporation at 85°C. In order to remove Ge while minimizing evaporative Se losses, samples were additionally
 138 dissolved and dried down twice with 10.5 N HCl at 85°C in the presence of rock matrix. Selenium was purified
 139 by a two-stage column chemistry using 7 mL of Eichrom AG1-X8 and AG 50W-X8 (both 100–200 mesh) ion
 140 exchange resins (collected in 4 N HCl and 0.1 N HNO₃, respectively). The dry Se cuts were subsequently
 141 dissolved and evaporated in 10.5 N HCl. Tellurium was collected in 0.4 N HCl from the first column after eluting
 142 Se and most matrix elements with 4 N HCl and Fe with a 2 N HCl–5 N HF mixture. Finally, the dry Se and Te
 143 fractions were taken up in 1 mL 2 N HCl for analysis. Total procedural recoveries of Se and Te for MORBs are
 144 systematically ~85–95%, higher than that for reference materials (~80%; Yierpan et al., 2018). Procedural blanks
 145 (n = 5) yield signal intensities for each isotope indistinguishable from the background (2 N HCl), which are
 146 equivalent to ~0.05 and 0.01 ng for Se and Te, respectively.

147 Selenium isotopes were measured on a ThermoFisher Scientific NeptunePlus multi-collector inductively
 148 coupled plasma mass spectrometer (MC-ICP-MS) connected to a HGX-200 hydride generator. The double spike
 149 method was used to correct for isotopic fractionation during the chemistry and instrumental analysis. Each
 150 analysis was bracketed by 30 ng mL⁻¹ spiked NIST SRM 3149 standard. The Se isotope composition is
 151 expressed using δ-notation relative to the international reference material NIST SRM 3149 following:

$$152 \quad \delta^{82/76}\text{Se}_{\text{Sample}} = \frac{(^{82}\text{Se}/^{76}\text{Se})_{\text{Sample}}}{(^{82}\text{Se}/^{76}\text{Se})_{\text{NIST SRM 3149}}} - 1 \quad (1)$$

153 δ^{82/76}Se values are reported in ‰ units by multiplication with a factor of 1,000. In order to fully eliminate
 154 residual Ge that represents a significant isobaric interference (Stüeken et al., 2013; Pogge von Strandmann et al.,
 155 2014), post-chemistry Se fractions were additionally evaporated (1–2 times) in HCl at 85–90°C and monitored
 156 for Ge using sample aliquots before analysis (Luais, 2012; Yierpan et al., 2018). Each analyzed sample has
 157 ⁷²Ge/⁸²Se < 0.0002 (with <~10% evaporative Se loss). Hydride interferences of Se, Br, and ArAr are generally
 158 insignificant owing to the methane addition (Floor et al., 2011; Kurzawa et al., 2017) and associated corrections
 159 (mainly SeH) on δ^{82/76}Se are typically ≤ 0.04‰. For most sample analyses, ~20–40 ng Se was used and the
 160 internal error (2 standard error, 2 s.e.) of a single measurement over 40 cycles is mostly < 0.05‰. Analytical
 161 accuracy and precision were monitored by analyses of inter-laboratory standard MH-495 (30 ng mL⁻¹;
 162 Supplementary Table S1) and three reference materials (Table 1; Fig. 1). The MH-495 yields an average δ^{82/76}Se
 163 of -3.24 ± 0.07‰ (2 s.d., n = 20), in excellent agreement with literature values (Zhu et al., 2008; Kurzawa et al.,
 164 2017; Labidi et al., 2018; Yierpan et al., 2018). The δ^{82/76}Se values of BHVO-2 (+0.10 ± 0.11‰; 2 s.d., n = 4)
 165 and W-2a (0.00 ± 0.04‰; 2 s.e., n = 1) are comparable to the previously reported values of +0.18 ± 0.10‰ (2
 166 s.d., n = 8) and -0.09 ± 0.11‰ (2 s.d., n = 6), respectively (Yierpan et al., 2018; Fig. 1). Two BCR-2 digestions
 167 yield δ^{82/76}Se values (+0.18 ± 0.09‰ and +0.15 ± 0.07‰; 2 s.e.) that are identical to the average value from
 168 Kurzawa et al. (2017) (+0.18 ± 0.11‰; 2 s.d., n = 3) but somewhat lower than that from Yierpan et al. (2018)
 169 (+0.29 ± 0.10‰; 2 s.d., n = 5; Fig. 1). BCR-2 yields an overall average δ^{82/76}Se of +0.23 ± 0.14‰ (2 s.d., n =

170 10), whose uncertainty is slightly higher than a typical external reproducibility of 0.10 to 0.12‰ (2 s.d.) on other
171 reference materials (Fig. 1; Yierpan et al., 2018). Note that all these analyses were performed in the same lab
172 (Fig. 1). Considering potentially smaller sample heterogeneity in a glass matrix relevant to this study, the external
173 reproducibility for MORB was assessed by replicate analyses of a randomly selected moderately evolved sample
174 (PAC2 DR33-1; 6.63 wt.% MgO) with different sample amounts (0.15–0.4 g; Table 1). We obtain a 2 s.d.
175 uncertainty of 0.09‰ from 7 digestions and 9 measurements (4 different sessions over 6 months).

176 The isotope dilution concentrations for Te (and when necessary, also for Se; Table 2) were determined on
177 a ThermoFisher Scientific iCAP-Qc quadrupole ICP-MS connected to an ESI hydride ICP hydride generator.
178 Only ~0.1–0.3 ng Te and 0.5–1 ng Se (in 1 mL 2 N HCl) were used for each analysis. The analytical precision
179 of our method was previously reported to be ~2–3% r.s.d. (relative standard deviation) for both Se and Te. All
180 reference materials yield Se–Te concentrations that are in general agreement with the recently published data
181 (Table 1; Lissner et al., 2014; Wang et al., 2015; Yierpan et al., 2018). The Se concentrations of MORBs obtained
182 by double spike inversion and isotope dilution are always comparable within 2% and both reproduce at ~2% r.s.d.
183 (Tables 1 and 2).

184 **3.2. Trace element analysis**

185 Only a few trace element data have been published for the PAC1 samples (latitude 65–56°S), whereas the
186 data for PAC2 samples (latitude 53–41°S) are relatively complete (Supplementary Table S2; Vlastélic et al.,
187 2000; Hamelin et al., 2010; Clog et al., 2013; Labidi et al., 2014; Bezard et al., 2016). To fully characterize the
188 samples, we report a more complete set of trace element data (43 elements). The measurements were performed
189 at the University of Tübingen by solution ICP-MS following the method previously described by Babechuk et
190 al. (2010) and Albut et al. (2018). About 0.02 g of sample powder was digested and diluted with 2% HNO₃
191 containing an internal standard solution (⁶Li, In, Re, and Bi) to the analyte solution with a final dilution factor
192 of ~10,000. Reproducibility and accuracy of trace element determinations were evaluated from the average data
193 of BHVO-2 (quality control standard) from 14 analyses of 6 separate digestions (4 digested together with the
194 PAR samples). Our BHVO-2 results (Supplementary Table S3) show uncertainties better than ~5% r.s.d. for all
195 elements except for Mo, Sb, W, and Tl (~8–20%). Most data agree within ~5% with previously reported values
196 (GeoReM; Jochum et al., 2005).

197 **4. Results**

198 **4.1. Major/trace element composition**

199 The trace element concentrations determined here, together with all available major/trace element,
200 radiogenic/stable isotope data, are compiled in Supplementary Table S2. All samples are typical N-MORB
201 (normal MORB) with (La/Sm)_N ratios of 0.461–0.965 (normalized to PM; McDonough and Sun, 1995), except
202 PAC2 DR27-1 ((La/Sm)_N = 1.227), which is the most evolved sample (4.52 wt.% MgO) and dredged from a

203 seamount-ridge transition zone (Hamelin et al., 2010). The PM-normalized trace element patterns of PAR glasses
204 are similar to that of the average N-MORB compiled by Gale et al. (2013) (Supplementary Fig. S2). Variations
205 in major element compositions of the studied samples span the entire spectrum observed in PAR basalts from
206 65–56°S and 53–41°S, with MgO content from 8.85 to 4.52 wt.% (Supplementary Fig. S3). This MgO range is
207 larger than that of MORBs previously investigated for Se–Te systematics (7.02–9.23 wt.%; Hertogen et al., 1980;
208 Lissner et al., 2014). The most evolved glasses (MgO <5 wt.%; n = 3) have experienced titanomagnetite
209 fractionation, evidenced by a decrease in Ti and Fe from the general trend after 5 wt.% MgO (Supplementary
210 Fig. S3; Vlastélic et al., 2000; Hamelin et al., 2010). Similar abrupt drops are also consistently observed for
211 concentrations of Zn, Ga, Mn (not shown), V, Sc, and Co in these evolved samples (e.g., Supplementary Fig. S2),
212 probably resulted from the magnetite saturation and/or the induced sulfide segregation due to their strong
213 partitioning into these phases (Nielsen et al., 1994; Toplis and Corgne, 2002; Righter et al., 2006; Dare et al.,
214 2012, 2014; Labidi et al., 2014; Jenner et al., 2010, 2012, 2015).

215 4.2. Selenium isotope composition and Se–Te abundances

216 The selenium isotope composition and Se–Te concentrations of the studied PAR samples are reported in
217 Table 2 together with S (Labidi et al., 2014) and selected major element data. The uncertainties on $\delta^{82/76}\text{Se}$ and
218 Se–Te abundances throughout the text are given in 2 and 1 s.d., respectively. The PAR glasses display $\delta^{82/76}\text{Se}$
219 values ranging between $-0.30 \pm 0.09\text{‰}$ and $-0.05 \pm 0.09\text{‰}$, with an average of $\delta^{82/76}\text{Se} = -0.16 \pm 0.13\text{‰}$ (n =
220 27; Fig. 2 and 3). The differences in $\delta^{82/76}\text{Se}$ between sample duplicates (n = 12) never exceeded the 2 s.d.
221 external reproducibility of 0.09‰ (Table 1). The glassy rim and pillow interior of PAC2 DR01-1 that were
222 analyzed separately yield identical $\delta^{82/76}\text{Se}$ values within uncertainty ($-0.13 \pm 0.09\text{‰}$ and $-0.18 \pm 0.09\text{‰}$,
223 respectively; Table 2). However, small but resolvable isotopic variations (up to $0.25 \pm 0.13\text{‰}$ in $\delta^{82/76}\text{Se}$) are
224 observed between different samples (e.g., between PAC1 DR06-g and PAC2 DR29-1, with $\delta^{82/76}\text{Se}$ of $-0.30 \pm$
225 0.09‰ and $-0.05 \pm 0.09\text{‰}$, respectively). These variations are not systematically related to the sample latitude
226 or ridge axial depth (Fig. 2a and b). The average $\delta^{82/76}\text{Se}$ of the two PAR sections (Fig. 2a) are identical within
227 uncertainty: $-0.14 \pm 0.12\text{‰}$ north of the Vacquier FZ (n = 17) and $-0.19 \pm 0.14\text{‰}$ south of the Udintsev FZ
228 (n = 10). $\delta^{82/76}\text{Se}$ values of the samples are fairly constant over the wide range of Se abundances observed (158–
229 219 ng g⁻¹; Fig. 2c).

230 The MORBs show systematic offset towards lighter Se isotope composition compared to all previously
231 analyzed basalts (average $\delta^{82/76}\text{Se}$ between $+0.21 \pm 0.15\text{‰}$ and $+0.30 \pm 0.32\text{‰}$; n = 9) and one peridotite ($+0.24$
232 $\pm 0.32\text{‰}$), with some marginal overlap with the latter (Fig. 3; Rouxel et al., 2002, 2004; Kurzawa et al., 2017;
233 Yierpan et al., 2018; this study). The MORB average $\delta^{82/76}\text{Se}$ ($-0.16 \pm 0.13\text{‰}$) lies in the range of chondritic
234 values of $-0.30 \pm 0.39\text{‰}$ (n = 14; Vollstaedt et al., 2016) and $-0.21 \pm 0.31\text{‰}$ (n = 20; Labidi et al., 2018) (Fig.
235 3). Specifically, it is similar within uncertainty to $\delta^{82/76}\text{Se}$ values of ordinary chondrites ($-0.21 \pm 0.10\text{‰}$; n = 9)
236 and CO ($-0.19 \pm 0.07\text{‰}$; n = 2), CV ($-0.25 \pm 0.12\text{‰}$; n = 2), and CI ($-0.01 \pm 0.09\text{‰}$; n = 2) carbonaceous
237 chondrites, but distinct from that of enstatite chondrites ($-0.40 \pm 0.07\text{‰}$; n = 3; Labidi et al., 2018; Fig. 3).

238 Fig. 4 presents the variation of Se, Te, S, and Cu abundances and/or their ratios versus MgO contents of
239 PAR basalts. The generally negative correlation of Se (from 158 ± 1 to 219 ± 4 ng g⁻¹) and positive correlations
240 Te (from 4.10 ± 0.12 to 1.16 ± 0.03 ng g⁻¹) with MgO show their apparently contrasting compatibilities (Fig. 4a
241 and b), which result in significant Se/Te fractionation (increasing from 42.9 ± 1.1 to 188.8 ± 4.7 with decreasing
242 MgO content; Fig. 4c). Selenium in PAR MORBs seems to behave as an apparently incompatible element,
243 opposite to observations from the southern Mid-Atlantic Ridge (SMAR) basalts (Lissner et al., 2014). At a given
244 MgO, PAR MORBs tend to have higher Se content than SMAR N-MORBs (Fig. 4a). Two samples from the
245 Indian ocean have anomalously high Se contents (~ 330 ng g⁻¹) compared to the range in PAR and SMAR, but
246 these samples have probably been affected by assimilation of wall-rock sulfide cumulates (Fig. 4a; Hertogen et
247 al., 1980). Tellurium displays similarly apparent compatibility in a global context (Fig. 4b; Hertogen et al., 1980;
248 Yi et al., 2000; Lissner et al., 2014). It is noteworthy, however, that Te contents in SMAR E-MORBs (i.e.,
249 enriched- and transitional-type MORBs) are generally higher than in N-MORBs, attributed to Te enrichment
250 (relative to Se) in an E-MORB mantle source (Lissner et al., 2014). This is in agreement with the distinctly lower
251 Se/Te and S/Te ratios of E-MORBs compared to N-MORBs over almost the entire melt evolution in both PAR
252 and SMAR (Fig. 4c and e). Besides, the S/Se variations in these settings (Fig. 4d) appear to follow two distinct
253 trends, with Se being more compatible relative to S in the SMAR melts than in PAR melts. The Cu/Se ratios in
254 both PAR and SMAR for MgO contents above ~ 7 – 7.5 wt.% remain fairly constant and identical (418 ± 24 and
255 408 ± 22 , respectively; Fig. 4f). The constant Cu/Se ratios were previously interpreted to reflect a similar
256 geochemical behavior of these elements based on a relatively small data set (MgO ~ 7 – 9 wt.%; Lissner et al.,
257 2014). Below ~ 7 wt.% MgO, the Cu/Se ratios of PAR basalts smoothly decrease from 346 to 178, indicating an
258 overall higher compatibility of Cu.

259 **5. Discussion**

260 **5.1. Effects of non-magmatic processes on Se isotopes and S–Se–Te abundances**

261 Non-magmatic processes that may potentially affect the S–Se–Te systematics of MORB melts generally
262 include eruption-related degassing and assimilation of hydrothermal fluids during and/or after MORB
263 differentiation in crustal magma chambers (Jenner et al., 2010; Floor and Román-Ross, 2012; Labidi et al., 2014;
264 Lissner et al., 2014). All the studied PAR glasses are sulfide saturated as evidenced by the systematically
265 observed immiscible sulfide droplets and the correlation between S and FeO contents (Labidi et al., 2014). The
266 latter, together with the lack of correlation between S content and eruption depth (~ 2220 – 2950 m; Supplementary
267 Table S2), also argues against eruptive S degassing (Moore and Fabbi, 1971; Moore and Schilling, 1973; Mathez,
268 1976; Wallace and Edmonds, 2011; Labidi et al., 2014). Little is known about the Se–Te gaseous species and
269 their formation conditions in igneous systems. Similar to S, Se and Te are possibly dissolved in a silicate melt
270 as Se²⁻ and Te²⁻ and/or Se⁴⁺ and Te⁴⁺ depending on the prevailing oxygen fugacity (e.g., Nagamori and Mackey,
271 1977; Fang and Lynch, 1987; Choi and Cho, 1997; Wykes et al., 2011). In the case of (PAR) MORB, S occurs

272 almost exclusively as reduced S^{2-} and retained in the glass during submarine quenching (Labidi et al., 2014).
273 Since transition of selenide and telluride to oxyanions requires higher redox potential relative to sulfide
274 ($Se > Te > S$ at a given temperature and pH; Yamamoto 1976; Brookins, 1988; McPhail, 1995; Johnson, 2004;
275 König et al., 2019), we suggest that Se and Te are dissolved in MORB melts in the form of Se^{2-} and Te^{2-} and
276 are (also) unlikely to degas during submarine eruption (also see Yi et al., 2000; Jenner et al., 2010; Lissner et al.,
277 2014). This would be in accordance with the lack of a systematic variation of Se isotopes (Fig. 2b) and Se–Te
278 contents (not shown) with the ridge axial depth (>2220 m).

279 The majority of PAR basalts have experienced interaction with chlorine-rich brines and/or hydrothermally
280 altered materials during magmatic differentiation (Clog et al., 2013; Labidi et al., 2014). We have examined the
281 potential effect of hydrothermal fluid contamination on Se isotopes and Se–Te concentrations using Cl/K ratio
282 as an indicator of the extent of chlorine contamination because Cl and K are not fractionated during magmatic
283 processes (Fig. 5; Michael and Cornell, 1998; Clog et al., 2013; Labidi et al., 2014). Previous studies on PAR
284 samples show that this process did not significantly affect D/H ratios and stable Mo isotope compositions (Clog
285 et al., 2013; Bezaud et al., 2016), but systematically shifted the S isotope compositions towards heavier values
286 ($> -0.5\%$ in $\delta^{34}S_{V-CDT}$) when the chlorine contamination was associated with high-temperature ($>300^\circ C$)
287 hydrothermal sulfide assimilation (Fig. 5a; Labidi et al., 2014). Volcanogenic massive sulfides from sediment-
288 starved environments (such as hydrothermal systems at mid-ocean ridges) show highly variable and mostly
289 negative $\delta^{82/76}Se$ values from -4.75% to $+0.7\%$ (Rouxel et al., 2002, 2004; Layton-Matthews et al., 2013).
290 However, we do not observe any systematic deviations in $\delta^{82/76}Se$ values of the samples that show variable S
291 assimilation (i.e., $\delta^{34}S_{V-CDT}$ heavier than -0.5% ; $n = 7$) from the general variation trend along Cl/K or $\delta^{34}S_{V-CDT}$
292 (Fig. 5b and d). The sample PAC2 DR20-1 with the highest $\delta^{34}S_{V-CDT}$ value of $+0.60 \pm 0.10\%$ (1 s.d.;
293 Supplementary Table S2), which represents the highest amount of S assimilation, shows “typical” $\delta^{82/76}Se$ of
294 $-0.15 \pm 0.09\%$ (Table 2; Fig. 5d). Average $\delta^{82/76}Se$ values of the two sample subsets (i.e., with and without
295 sulfide assimilation) are identical within 2 s.d. uncertainty ($-0.14 \pm 0.12\%$ and $-0.16 \pm 0.14\%$, respectively).
296 Also, there is no clear covariation between the Se isotope composition and degree of Cl contamination (Fig. 5b).

297 On the other hand, there seems to be an apparent increase in S/Se ratio with Cl/K from 0.06 to 0.41 (Fig.
298 5c). Highest S/Se ratios ($\sim 8,000$) are also observed in two samples (PAC2 DR20-1 and PAC2 DR27-1) that have
299 experienced S assimilation (Fig. 4d and 5c). Compared to MORBs ($\sim 3,800$ – $9,200$; Fig. 4d; Lissner et al., 2014;
300 this study) and magmatic sulfides ($\sim 2,700$ – $8,700$; Patten et al., 2013, 2016), massive sulfides from sediment-
301 starved hydrothermal systems have much more variable S/Se ratios (500 – $500,000$), with lower values typical for
302 sulfides near mid-ocean ridges due to the formation of selenide or Se-rich sulfides at high temperature conditions
303 (Rouxel et al., 2004; Hannington et al., 2002; Layton-Matthews et al., 2008, 2013; Keith et al., 2016). Sulfur
304 assimilation would not increase S abundance (hence S/Se ratio) of the melt due to sulfide saturation (Labidi et
305 al., 2014; also see Section 5.2.2), but it may potentially increase the Se abundance because a MORB melt with
306 ~ 8 – 14 wt.% FeO can dissolve ~ 0.15 – 0.25 wt.% Se (Wykes et al., 2015). Labidi et al. (2014) show that the

307 highest $\delta^{34}\text{S}_{\text{V-CDT}}$ value ($+0.60 \pm 0.10\%$; 1 s.d.) can be reproduced by mixing a MORB melt having $1,000 \mu\text{g g}^{-1}$
308 S and $\delta^{34}\text{S}_{\text{V-CDT}} = -1\%$ with a maximum of 3.5 wt.% wall-rock having $10,000 \mu\text{g g}^{-1}$ S and $\delta^{34}\text{S}_{\text{V-CDT}} = +5\%$.
309 Assuming that the original melt has $\sim 168 \text{ ng g}^{-1}$ Se (at $1,000 \mu\text{g g}^{-1}$ S; from the general S–Se covariation), a
310 final melt with the lowest S/Se = 5,867 ($\delta^{34}\text{S}_{\text{V-CDT}} = -0.31\%$) observed in the contaminated samples (Fig. 5a
311 and c) would require only $\sim 3 \text{ ng g}^{-1}$ increase in Se concentration to be associated with an assimilation of
312 ~ 1.35 wt.% wall-rock. Note that a typical uncertainty of MORB Se concentration is also $\sim 3 \text{ ng g}^{-1}$ (Table 2).
313 Therefore, we argue that the observed variation in S/Se ratios of PAR basalts (Fig. 5c) are not influenced by
314 high-temperature hydrothermal sulfide assimilation but rather reflects magmatic differentiation (Fig. 4d; see
315 below). Note that Cl contamination broadly scales with the degree of magmatic differentiation (Labidi et al.,
316 2014), which readily accounts for the seemingly increasing S/Se with increasing Cl/K (Fig. 5c). The same
317 conclusion may be reached for S/Te ratios (not shown) and hence the observed Te abundances. Lastly, alteration
318 by seawater after the eruption (e.g., Lissner et al., 2014) or during magmatic differentiation are not likely to
319 influence the Se isotope or Se–Te elemental systematics of MORBs because of extremely low Se and Te
320 concentrations in modern seawater at relevant depths (~ 200 and $\sim 0.2 \text{ ng kg}^{-1}$, respectively; Cutter and Bruland,
321 1984; Cutter and Cutter, 2001; Lee and Edmond, 1985; Measures and Burton, 1980).

322 **5.2. Se–Te elemental systematics during MORB differentiation**

323 As chalcophile elements, Se and Te, together with S and Cu, are sensitive to progressive MORB
324 differentiation involving a concurrent precipitation of immiscible sulfides (Fig. 4). This process accounts for the
325 observed abundances and relative fractionation of Se–Te–S–Cu (Fig. 4) because these elements are all highly
326 incompatible in silicate minerals but show different partitioning into sulfides (Barnes et al., 2009; Patten et al.,
327 2013; Labidi et al., 2014; König et al., 2015; Brenan, 2015; Wang and Becker, 2015a; Kiseeva et al., 2017). Our
328 data shows a relative compatibility into sulfides (prior to magnetite saturation; see below) in the order of
329 $\text{Te} > \text{Cu} > \text{Se} > \text{S}$ (Fig. 4; Cu/Te ratio increases with decreasing MgO; not shown), consistent with earlier studies.
330 The difference in the relative compatibility of Se and Cu above and below ~ 7 wt.% MgO (see Section 4.2 and
331 Fig. 4f) may be attributed to different FeO content of the silicate melt (Brenan, 2015).

332 All these elements are affected by magnetite saturation-triggered sulfide segregation after ~ 5 wt.% MgO
333 (Fig. 4; also see Section 4.1), as previously observed for S in PAR MORB (Fig. 6a; Labidi et al., 2014) and other
334 chalcophile elements in glasses from worldwide arc settings (Jenner et al., 2010, 2012, 2015) and Kilauea Iki
335 lava lake (Greaney et al., 2017). One exception is PAC2 DR27-1, which is the most evolved sample (MgO
336 4.52 wt.%; Table 2) yet remains largely unaffected (Labidi et al., 2014). Compared to the extrapolated general
337 differentiation trends prior to 5 wt.% MgO, there is a consistent decrease in S–Se and increase in Te
338 concentrations in samples that have experienced magnetite-induced sulfide segregation (Fig. 4a, 4b, and 6a;
339 Supplementary Fig. S3). This is amplified by consistent and abrupt decrease in Se/Te and S/Te (Fig. 4c and e).

340 Selenium and tellurium likely segregate from the silicate melt as Fe–Se and Fe–Te complexes analogous
341 to Fe–S and thus their abundances in the melt should (also) be directly related to the FeO content. This is
342 evidenced by the significant effect of FeO on the Se solubility in silicate melts (Fang and Lynch, 1987; Wykes
343 et al., 2015) and on the partitioning of Se–Te between sulfide and silicate melts (Choi and Cho, 1997; Brenan,
344 2015; Kiseeva et al., 2017). Indeed, PAR MORBs display strong covariations between FeO_T and Se–Te contents
345 (Fig. 6b and c), similar to that observed for S (Labidi et al., 2014). Note that FeO_T monotonically increases with
346 decreasing MgO prior to magnetite saturation (Supplementary Fig. S3). In the following sections, we first model
347 Se–Te variations during MORB differentiation using FeO_T content as an index of crystal fractionation. We then
348 estimate the primary melt Se–Te contents by correcting the observed concentrations for crystal + sulfide
349 fractionation.

350 5.2.1. Modelling Se–Te variations and implications for chalcophile element partitioning

351 Details of the model calculations are given in Supplementary Material. Major element variations were
352 modelled by alphaMELTS (fractional crystallization; Ghiorso and Sack, 1995; Smith and Asimow, 2005). The
353 model curves for FeO_T yield the best match with the observed variation at 3 kbar and the resulting parameters
354 were used subsequently (Supplementary Fig. S3). Bulk partition coefficients of Se and Te ($D_{\text{Se or Te}}^{\text{bulk}}$) were
355 calculated using the mean sulfide fraction in the bulk segregated minerals ($X_{\text{sulf}}^{\text{bulk min}} = 0.14 \pm 0.04$ wt.%; based
356 on S systematics; Labidi et al., 2014) and two sets of experimentally determined sulfide liquid–silicate melt
357 partition coefficients ($D_{\text{Se or Te}}^{\text{sulf liq-sil}}$) considering the range of FeO contents of our samples: 450–650 for Se and
358 2600–3200 for Te (Kiseeva et al., 2017) and 1560 ± 410 – 1035 ± 360 for Se and 14430 ± 1680 – 9570 ± 1150 for
359 Te (1 s.d.; $D_{\text{Se or Te}}^{\text{sulf liq-sil}}$ decreases with increasing FeO; Brenan, 2015). The Se–Te variations were then modelled
360 by a combination of the fractional and batch crystallization laws because partitioning of a chalcophile element
361 between the fractionated sulfide and silicate melt is probably an intermediate (between pure fractional and batch)
362 equilibrium process (Rehkämper et al., 1999; Bézoz et al., 2005; Yang et al., 2014; Lissner et al., 2014; Kiseeva
363 and Wood, 2015). The partitioning mode is described by the parameter S_b , which is the mass fraction of sulfide
364 displaying batch partitioning (Rehkämper et al., 1999).

365 Dependency of the modelled Se–Te variations on the mode of sulfide–silicate melt partitioning (i.e., S_b) is
366 relatively small compared to that of other highly chalcophile elements (e.g., Rehkämper et al., 1999). This is
367 indicated by similar observed sulfide phase–silicate melt partition coefficients ($D_{\text{Se or Te}}^{\text{sulf-sil}}$) at S_b of 0 and 1 (by
368 inversion; Supplementary Material Eq. 2, 4, and 5; also see Bézoz et al., 2005; Lissner et al., 2014), which yields
369 $D_{\text{Se}}^{\text{sulf-sil}}$ of $\sim 560 \pm 190$ and 530 ± 180 and $D_{\text{Te}}^{\text{sulf-sil}}$ of $\sim 1600 \pm 600$ and 2200 ± 950 , respectively (1 s.d.). With
370 $S_b = 0.5$ and $D_{\text{Se or Te}}^{\text{sulf liq-sil}}$ from Kiseeva et al. (2017), the calculated trends well reproduce the observed Se–Te
371 variations across the PAR magmatic differentiation (Fig. 6b and c). On the other hand, the modelled trends using
372 $D_{\text{Se or Te}}^{\text{sulf liq-sil}}$ from Brenan (2015) predict much higher $D_{\text{Se or Te}}^{\text{bulk}}$ and cannot properly describe the observed patterns

373 with any S_b values (not shown). Based on the experiments of Brenan (2015), a lower apparent $D_{Te}^{sulf-sil}$ can be
 374 predicted if a significant fraction of the segregating sulfides is crystalline monosulfide solid solution (MSS) in
 375 which Te is significantly more incompatible relative to sulfide liquid ($D_{Te}^{MSS-sulf liq} \approx 0.02-0.08$ and $D_{Te}^{MSS-sil} = 729$;
 376 also see Helmy et al., 2010; Liu and Brenan, 2015); in this case, our observed $D_{Te}^{sulf-sil}$ at $S_b = 1$ would require
 377 $87 \pm 6\%$ of the sulfide phase to be MSS using an average $D_{Te}^{sulf liq-sil} = 11960 \pm 1400$ (see above). Such a high
 378 MSS fraction is however unlikely. At a pressure–temperature (P–T) range relevant to MORB differentiation
 379 (e.g., from ~ 1280 to 1160°C at 2–5 kbar until $\sim 70\%$ crystallization in most PAR melts; Fig. 7), segregated sulfide
 380 is at its liquidus near $\sim 1050-1125^\circ\text{C}$ according to sulfide melting experiments (Bockrath et al., 2004; Zhang Z.
 381 and Hirschmann, 2016) and empirical approximations on natural sulfides in MORB glasses (Patten et al., 2012).
 382 Although there is geochemical evidence that a certain proportion of MSS needs to be present in fractionating
 383 sulfides to explain the variations of some chalcophile elements (Li and Audétat, 2012), sulfide liquid is still the
 384 main (if not dominant) sulfide phase during much of MORB differentiation that occurs above the sulfide liquidus
 385 (e.g., Bézoz et al., 2005; Jenner et al., 2010; Li and Audétat, 2012; Lissner et al., 2014; Brenan, 2015). Besides,
 386 the fact that the observed Se–Te variations are well reproduced with $D_{Se or Te}^{sulf liq-sil}$ from Kiseeva et al. (2017) argues
 387 against a significant control of MSS fractionation on Se–Te systematics of PAR glasses. Another alternative
 388 explanation for the observed low $D_{Te}^{sulf-sil}$ compared to $D_{Te}^{sulf liq-sil}$ from Brenan (2015) could be poor equilibration
 389 between sulfides and silicate melt (i.e., $R_{eff} < 1$) as previously proposed for partitioning of platinum-group
 390 elements in MORBs (Rehkämper et al., 1999; Bézoz et al., 2005; Yang et al., 2014). However, the extent of
 391 sulfide–silicate equilibration in our case might not be properly assessed due to the difference in the experimental
 392 $D_{Se or Te}^{sulf liq-sil}$ published by Brenan (2015) and Kiseeva et al. (2017) for the range of FeO content of PAR basalts.

393 Finally, only for the highly evolved MORB melts (PAC1 DR10-1g and PAC2 DR20-1) that have
 394 experienced $>70\%$ crystallization and magnetite-triggered sulfide segregation (Fig. 6a; Supplementary Fig. S3),
 395 we suggest crystalline MSS to be the dominant fractionating sulfide phase to account for the observed abrupt
 396 drop in Se/Te (and S/Te) ratios (Fig. 4), considering $D_{Se}^{sulf liq-sil} < D_{Te}^{sulf liq-sil}$ and $D_{Se}^{MSS-sil} > D_{Te}^{MSS-sil}$ (Brenan, 2015).
 397 This was previously proposed for sulfide-saturated arc magmas based on Cu–Ag systematics (Jenner et al., 2010,
 398 2012, 2015).

399 5.2.2. Primary melt Se–Te contents: Consideration of sulfide saturation

400 The primary melt major element composition was calculated following Lee et al. (2009) by adding liquidus
 401 olivine back into primitive samples with MgO $> \sim 8.5$ wt.% ($n = 10$; Vlastélic et al., 2000; Hamelin et al., 2010)
 402 until the melts reach equilibrium with mantle olivine containing $Mg\# = 0.90$ ($Mg\#$: molar $Mg/(Mg + Fe^{2+})$).
 403 Assuming the glasses have $Fe^{2+}/\Sigma Fe = 0.87$ (e.g., Bézoz and Humler, 2005; Zhang H. L. et al., 2018), we obtain
 404 an average primary melt composition of ~ 11.8 wt.% MgO and ~ 8.8 wt.% FeO_T at ~ 10.2 kbar and $\sim 1325^\circ\text{C}$ after
 405 $\sim 8.7\%$ olivine addition. For the Se–Te contents, we applied a two-step correction. Considering all studied glasses

406 are sulfide-saturated, based on the strong covariation paths of Se–Te with FeO_T (Fig. 6b and c) and FeO_T with
407 MgO (Supplementary Fig. S3), the Se–Te contents were first corrected to FeO_T content (8.49 wt.%) of the most
408 primitive sample (PAC1 DR12-1g; 8.85 wt.% MgO) following a linear regression scheme previously used for
409 other elements (e.g., Klein and Langmuir, 1987; Bézous et al., 2005; Kelley et al., 2006; Lissner et al., 2014).
410 This yields 164 ± 8 and $3.4 \pm 0.4 \text{ ng g}^{-1}$ Se and Te, respectively (melts experiencing magnetite saturation were
411 excluded; see Fig. 4 and Supplementary Fig. S2 and S3). Further corrections (from 8.85 to 11.8 wt.% MgO)
412 along some linear slope with MgO or Mg# depend on whether the more primitive melts are sulfide-saturated.
413 Several global MORBs with MgO >9 wt.% (Jenner and O'Neill, 2012; Jenner et al., 2015) seem to display a
414 clear absence of fractionation between chalcophile elements that have quite different $D^{\text{sulf liq-sil}}$ (e.g., Cu, As, Se,
415 Ag, In, Sn, Tl, and Pb; Li and Audétat, 2012; Patten et al., 2013; Kiseeva and Wood, 2015; Kiseeva et al., 2017),
416 which might indicate a sulfide undersaturation in high-MgO basalts (also see Ding and Dasgupta, 2017).

417 In this regard, we calculated the S solubilities of the primary PAR melts at their last equilibration with the
418 mantle (see above) using the recent sulfur content at sulfide saturation (SCSS) model of Smythe et al. (2017)
419 while taking into account the effect of equilibrium sulfide chemistry (Fig. 6a). It shows that, with a wide range
420 of sulfide compositions (42–51 wt.% Fe, 9–18 wt.% Ni, and 0.4–10 wt.% Cu; Bockrath et al., 2004; Patten et
421 al., 2013; Kiseeva and Wood, 2015; Zhang Z. and Hirschmann, 2016; Keith et al., 2017), SCSS of the primary
422 melts range from 1117 ± 44 to $1394 \pm 55 \text{ } \mu\text{g g}^{-1}$, which decreases with decreasing X_{Fe} in sulfides ($X_{\text{Fe}} = \text{Fe}/(\text{Fe}$
423 $+ \text{Ni} + \text{Cu})$ molar ratio). Even the lowest SCSS seems to be still higher than the S contents of the primitive PAR
424 glasses (932–968 $\mu\text{g g}^{-1}$; Labidi et al., 2014), implying that primary melts might be sulfide-undersaturated. The
425 modelled SCSS (Smythe et al., 2017) across the entire magmatic evolution (with $X_{\text{Fe}} = 0.65$ at 3 kbar and $f\text{O}_2$ of
426 FMQ – 0.18; Supplementary Material) shows that MORBs may have reached sulfide saturation during early
427 differentiation (P from ~10.2 to 3 kbar and T from ~1325 to 1248°C; Fig. 7) due to the decreasing S solubility
428 as well as olivine crystallization; they then remained sulfide-saturated, which also matches the model of Ariskin
429 et al. (2013, 2018) that considers the effect of sulfide chemistry using Ni contents of the silicate melts (Fig. 6a).
430 Both predictions are consistent with the observed sulfide saturation in the PAR as well as global spreading-ridge
431 glasses (Jenner et al., 2012, 2015; Labidi et al., 2014; Smythe et al., 2017; but see Shimizu et al., 2016). Although
432 primitive basalts (MgO >9–10 wt.%) were also suggested to be S undersaturated based on a variety of S solubility
433 models, these models can result in significant differences in SCSS (up to 1,000 $\mu\text{g g}^{-1}$) at a given condition (Saal
434 et al., 2002; Ding and Dasgupta, 2017; and references therein). The model of Smythe et al. (2017), which we
435 applied for our model primary melts, also carries large uncertainties (~25%). Here, we tentatively assume that
436 parental PAR melts (MgO >8.85wt.%) are sulfide undersaturated and accordingly the Se–Te concentrations after
437 the first-step correction were further corrected for ~8.7% olivine fractionation only. This yields average Se and
438 Te concentrations of 150 ± 8 and $3.1 \pm 0.4 \text{ ng g}^{-1}$, respectively, for PAR primary melts (Se/Te = 48.4 ± 6.8 ; n =
439 24; Fig. 6b and c). This Se/Te ratio would represent an upper limit if the primary melts are S saturated. These
440 estimates are significantly lower than for the SMAR N-MORB primary melts (230–254 and 9.0–11.3 ng g^{-1} ,

441 respectively; Se/Te = 22–26; Lissner et al., 2014). This discrepancy may be attributed to the difference in the
442 observed Se–Te variations (Fig. 4a, b, and c; Section 4.2) as well as the correction approach used between two
443 studies. Additional uncertainties may also result from other complexities during MORB differentiation (e.g.,
444 Coogan and Dosso, 2016; Lissenberg and MacLeod, 2016; O'Neill and Jenner, 2012). Most importantly, the
445 clear negative slope in Te versus MgO in PAR MORBs is not resolved in SMAR N-MORBs (Lissner et al.,
446 2014) due to the smaller MgO range of the latter (Fig. 4b). A wider compositional range of N-MORB now proves
447 to be more appropriate (this study) than coupled N- and E-MORB arrays (Lissner et al., 2014) in order to
448 adequately correct for differentiation and recover the primary melt Se–Te contents.

449 **5.3. Role of partial melting on Se–Te systematics and inferences on composition of the upper** 450 **mantle**

451 5.3.1 Partitioning behavior of Se–Te during mantle melting

452 In the upper mantle, Se and Te are mainly hosted by Fe–Ni–Cu base metal sulfides and platinum-group
453 minerals (Guo et al., 1999; Hattori et al., 2002; Lorand and Alard, 2010; König et al., 2015; Lorand and Luguët,
454 2016). The behavior of Se–Te during mantle melting is thus predominantly controlled by fractionation between
455 these phases and silicate melt. However, their absolute and relative partitioning during melting has been debated.
456 Based on the apparent variation in Se–Te abundances of peridotites, some authors suggest a slightly more
457 incompatible behavior of Se compared to Te, with both being moderately incompatible (Wang and Becker, 2013;
458 Wang et al., 2013). This relative partitioning is however opposite to observations from highly depleted
459 harzburgites (König et al., 2012, 2014, 2015; Luguët et al., 2015). Hertogen et al. (1980), from the MORB
460 perspective, suggest that Se is much more incompatible than Te during melting, with Te being rather compatible.
461 This was based on the observed lack of clear Se/Te fractionation during magmatic differentiation and distinctly
462 higher Se/Te ratios of global MORBs compared to mantle rocks (Hertogen et al., 1980; and references therein).
463 In fact, as shown for PAR and SMAR MORBs (Fig. 4c), significant Se/Te fractionation occurs during MORB
464 differentiation. This was not evident from the relatively small sample suite of Hertogen et al. (1980) probably
465 due to (1) different source composition (Section 4.2) and (2) different mode and rate of sulfide fractionation
466 during low-P magmatic differentiation in different spreading ridges (e.g., Bézoz et al., 2005; Yang et al., 2014;
467 Lissner et al., 2014), which may result in different apparent fractionation of Se/Te among genetically unrelated
468 samples. Lissner et al. (2014) propose that both Se–Te are apparently incompatible during melting, with Te being
469 more incompatible, although the empirical $D_{Se\ or\ Te}^{sulf\ liq-sil}$ they applied for modelling seem to suggest the opposite at
470 low- to moderate-degree melting. Besides, both PAR and SMAR MORB data show that Te is much more
471 compatible than Se during magmatic differentiation (Fig. 4c; Section 5.2.1), in accordance with experimental or
472 empirical constraints (Peach et al., 1990; Patten et al., 2013; Lissner et al., 2014; Brennan, 2015; Wang and Becker,
473 2015a; Kiseeva et al., 2017).

474 These discrepancies have been explained by the presence of different equilibrium sulfide assemblages
475 (sulfide liquid and crystalline MSS) during MORB differentiation and mantle melting, which involve sulfide
476 liquid–silicate melt partitioning and MSS–sulfide liquid/silicate melt partitioning, respectively (Lorand and
477 Alard, 2010; Lissner et al., 2014; König et al., 2014, 2015; Brenan, 2015). This is because Te is much more
478 incompatible in MSS relative to sulfide liquid than Se (with $D_{Se\ or\ Te}^{MSS-sulf\ liq}$ of $\sim 0.56\text{--}0.75$ and $\sim 0.02\text{--}0.08$ for Se
479 and Te, respectively; Helmy et al., 2010; Liu and Brenan, 2015; Brenan, 2015). The presence of MSS in the
480 MORB mantle was also experimentally shown and used to explain the partitioning behavior of chalcophile and
481 highly siderophile elements during melting (e.g., Bockrath et al., 2004; Bézos et al., 2005; Ballhaus et al., 2006;
482 Fischer-Gödde et al., 2011; Brenan, 2015). However, the sulfide liquidus (Fig. 7) determined by Bockrath et al.
483 (2004) has been questioned (Hart and Gaetani, 2006; Fonseca et al., 2012; Mungall and Brenan, 2014; Zhang Z.
484 and Hirschmann, 2016). Recent sulfide melting experiments using the same sulfide composition as in Bockrath
485 et al. (2004) show that crystalline MSS is not stable in the convecting upper mantle (Fig. 7; Zhang Z. and
486 Hirschmann, 2016; Zhang Z. et al., 2018), which indicates that behavior of chalcophile elements during the
487 partial melting might be entirely controlled by sulfide liquid–silicate melt partitioning, in favour of earlier
488 conclusions based on Cu–Ag systematics of mantle rocks and melts (Wang and Becker, 2015b; Jenner et al.,
489 2015).

490 5.3.2 Melting model

491 In order to further understand the role of partial melting on the Se–Te systematics of MORB melts and
492 mantle residues, we modelled the behavior of Se–Te in a triangular passive-flow near-fractional melting regime,
493 which was previously used to explain the Se–Te and highly siderophile element systematics of MORBs (e.g.,
494 Rehkämper et al., 1999; Lissner et al., 2014; Brenan, 2015). The modelling procedures and parameters are
495 detailed in Supplementary Material and summarized in Table 3. Briefly, the melt major element compositions
496 and P–T conditions for calculating the SCSS (Smythe et al., 2017) and $D_{Se\ or\ Te}^{sulf\ liq-sil}$ (as a function of FeO; Brenan,
497 2015; Kiseeva et al., 2017) were modelled with alphaMELTS front end (pMELTS mode; Ghiorso et al., 2002;
498 Smith and Asimow, 2005) at a mantle potential temperature of 1350°C following a similar approach used by
499 Ding and Dasgupta (2017) (Fig. 6). The depleted mantle composition was taken from Salters and Stracke (2004)
500 assuming 0.2 wt.% Fe₂O₃ (e.g., Cottrell and Kelley, 2011). The average melting degree (F_B ; Langmuir et al.,
501 1992; Plank et al., 1995) of the samples was estimated using differentiation-corrected incompatible trace element
502 concentrations by (1) solving the simple batch melting equation for F_B (e.g., Kelley et al., 2006) and (2)
503 comparing the concentrations to the result from pMELTS (near-fractional melting). These two approaches yield
504 consistent F_B of $\sim 6.6\text{--}11.7\%$ (average $8.5 \pm 1.5\%$) and $6.5\text{--}9.5\%$ (Supplementary Fig. S4), respectively, in
505 agreement with the previous estimates for global MORBs (e.g., Klein and Langmuir, 1987; Salters and Stracke,
506 2004; Workman and Hart, 2005; Kimura et al., 2017). Three different upper mantle sulfide compositions were
507 considered when calculating the SCSS of the partial melts ($X_{Fe} = 0.44\text{--}0.74$ and $Ni/(Fe + Ni) = 0.25\text{--}0.53$ at a
508 constant $(Fe + Ni + Cu)/S = 0.93$; Supplementary Fig. S5). Considering a large number of input parameters in

509 our model, in order to assure an internal consistency and reliability of our MORB mantle Se–Te estimates, we
510 first modelled the variation of S and Cu during partial melting (Fig. S5) because their mantle abundances
511 (McDonough and Sun, 1995; Salters and Stracke, 2004; Lorand et al., 2013; Lorand and Lugué, 2016; Palme
512 and O'Neill, 2014; Wang and Becker, 2013, 2015b) and behavior during mantle melting are relatively well
513 established (e.g., Lee et al., 2009; Li and Audétat, 2012; Kiseeva and Wood, 2013, 2015; Ding and Dasgupta,
514 2017).

515 Our result shows that the PAR primary melt S concentrations are well reproduced for the estimated F_B of
516 the samples using a range of source S content from “PM-like” $200 \mu\text{g g}^{-1}$ (e.g., Palme and O'Neill, 2014; Wang
517 and Becker, 2013) to slightly lower $150 \mu\text{g g}^{-1}$ as estimated for the depleted MORB mantle (e.g., Lugué et al.,
518 2003; Bézou et al., 2005; Nielsen et al., 2014; Lorand and Lugué, 2016) in combination with the SCSS model
519 of Smythe et al. (2017) and equilibrium “sulfide B” (Fig. S5a). Note that this sulfide chemistry is typical for
520 lherzolite-hosted sulfides (e.g., Lorand and Lugué, 2016; Kiseeva et al., 2017) and consistent with the suggested
521 range of Ni/(Fe + Ni) value for a shallow mantle Cu-free sulfide liquid (0.4–0.6) by recent experiments (Zhang
522 Z. et al., 2018) at the range of melting depth (~ 50 – 20 km; Fig. 7) and $f\text{O}_2$ (\sim FMQ; Cottrell and Kelley, 2011;
523 Zhang H. L. et al., 2018) estimated for the PAR basalts. The corresponding model curves also show an excellent
524 fit to the primary melt Cu concentrations with 170 – $200 \mu\text{g g}^{-1}$ S and 30 (or 24) $\mu\text{g g}^{-1}$ Cu in the source (Fig. S5b
525 and c).

526 5.3.3 Modelling Se–Te variations in mantle melts and residues

527 Fig. 8 and Fig. 9a show that the Se–Te systematics of PAR primary melts (150 ± 8 and $3.1 \pm 0.4 \text{ ng g}^{-1}$ Se
528 and Te, respectively; $\text{Se/Te} = 48.4 \pm 6.8$; $n = 24$) can be successfully reproduced by melting of a sulfide liquid-
529 bearing MORB mantle which has “fertile lherzolite-like” Se and Te contents (80 and 11 ng g^{-1} , respectively;
530 estimated at $3.52 \text{ wt.}\% \text{ Al}_2\text{O}_3$; Wang and Becker, 2013) using experimental $D_{\text{Se or Te}}^{\text{sulf liq-sil}}$ from Brenan (2015)
531 calculated at each 1% equilibrium melting (Table 3). With the same SCSS, the polybaric aggregate melts reach
532 S-undersaturation at F_B from $\sim 9.5\%$ to 11.5% , increasing with increasing initial S content from 170 to $200 \mu\text{g g}^{-1}$
533 (also see Supplementary Fig. S5a). This corresponds to an extent of melting F from $\sim 19\%$ to 23% in the central
534 melting column (i.e., F_{max} ; Supplementary Material) and is consistent with the conclusion of previous studies
535 using other empirical or experimental SCSS models (Lugué et al., 2003; Bézou et al., 2005; Lee et al., 2012;
536 Lissner et al., 2014; Brenan, 2015). In the case of $180 \mu\text{g g}^{-1}$ S, a mantle column becomes sulfide-exhausted
537 after $\sim 20\%$ melting. At any stage before sulfide exhaustion, Se is apparently much more incompatible than Te,
538 with contrasting $D_{\text{Se or Te}}^{\text{bulk}}$ values of ~ 0.69 – 0.01 and ~ 6.38 – 0.11 for Se and Te, respectively (decreasing with
539 ongoing partial melting). Therefore, a large Se/Te fractionation occurs between the melt and residue as long as
540 sulfide liquid is present in the system (Fig. 8c). The estimated F_B for PAR MORBs (~ 6.6 – 11.7%) indicates that
541 the primary aggregate melt is a mixture of melt increments derived from both sulfide-bearing (low- F) and
542 sulfide-exhausted (high- F) mantle columns (also see Ding and Dasgupta, 2017), and therefore, the observed

543 Se/Te fractionation in primary melts with respect to their source is largely accounted for by melting. This is in
544 contrast to the observations from the primary SMAR melts, in which the relative partitioning of Se and Te is
545 suggested to have played a minor role on the observed Se–Te variation (Lissner et al., 2014). This is because the
546 SMAR partial melts are mostly derived from sulfide-free mantle owing to the relatively high F_B (12.8–17.2%)
547 estimated by the authors, whereas sulfide exhaustion in their model occurs at around $F_B \approx 9\%$. However, as noted
548 by Kinzler and Grove (1993), the model of Niu and Batiza (1991) applied by Lissner et al. (2014) to estimate
549 the melting extent of the SMAR MORB tends to produce somewhat higher values compared to other models
550 using major element systematics. This may partly explain the different observations between our study and
551 Lissner et al. (2014) regarding the effect of partial melting on the observed Se/Te fractionation in MORB. The
552 modelling was also performed using experimental $D_{Se\ or\ Te}^{sulf\ liq-sil}$ of Kiseeva et al. (2017), from which the highest
553 values were taken (850 and 3800 for Se and Te, respectively) considering the FeO content of the equilibrium
554 melts (8.3–5.4 wt.%; Supplementary Material). However, these $D_{Se\ or\ Te}^{sulf\ liq-sil}$ overestimate the Se–Te contents of
555 the melts with a “fertile lherzolite-like” starting Se–Te contents (with $180\ \mu\text{g g}^{-1}\ \text{S}$; Fig. 8a and b). A good match
556 is obtained only after the source Se and Te contents are lowered to 48_{-8}^{+5} and $3.5_{-0.9}^{+0.5}\ \text{ng g}^{-1}$, respectively (Fig. 8
557 and 9a). With this set of $D_{Se\ or\ Te}^{sulf\ liq-sil}$, we obtain $49 \pm 11\ \text{ng g}^{-1}\ \text{Se}$ and $3.5 \pm 1.3\ \text{ng g}^{-1}\ \text{Te}$ on average for the PAR
558 mantle having $170\text{--}200\ \mu\text{g g}^{-1}\ \text{S}$. Considering the difference in experimental $D_{Se\ or\ Te}^{sulf\ liq-sil}$ between Brenan (2015)
559 and Kiseeva et al. (2017), it is uncertain which Se–Te contents actually represent the mantle source composition
560 (Fig. 9a).

561 The role of MSS–silicate melt partitioning on the behavior of Se–Te was investigated by incorporating
562 varying proportions of MSS and sulfide liquid into the bulk sulfide assemblage in the mantle ($180\ \mu\text{g g}^{-1}\ \text{S}$)
563 using experimental $D_{Se\ or\ Te}^{MSS-sil}$ from Brenan (2015) and “fertile lherzolite-like” Se–Te contents for consistency
564 (Supplementary Fig. S6). Due to the similar $D_{Se\ or\ Te}^{MSS-sil}$ of Se and Te (883 and 729, respectively), there is little
565 Se/Te fractionation during the entire melting interval if crystalline MSS is the only controlling sulfide phase
566 (also see Brenan, 2015); besides, both Se–Te concentrations are highly overestimated owing to their high
567 apparent incompatibilities, with $D_{Se\ or\ Te}^{bulk}$ values of $\sim 0.43\text{--}0.01$ and $0.35\text{--}0.01$ for Se and Te, respectively
568 (Supplementary Fig. S6). It shows that Se–Te systematics of the melt can only be reproduced if sulfide liquid is
569 the major controlling phase ($>50\%$; in the case of $180\ \mu\text{g g}^{-1}\ \text{S}$ in the source; Fig. 9a and Supplementary Fig.
570 S6).

571 On the other hand, the modelled Se–Te contents of the residue shows that the variations of Se–Te
572 abundances and Se/Te ratios of worldwide lherzolites (Fig. 9b and c) can be reproduced only when MSS is the
573 dominant, if not only, sulfide phase ($>90\%$) in the mantle. In this case, both Se and Te would be (apparently)
574 incompatible, with Te being more incompatible (e.g., Brenan, 2015). As mentioned earlier, this absolute and
575 relative partitioning during partial melting are in line with the conclusion of some studies (Lissner et al., 2014;
576 König et al., 2014, 2015) but cannot be reconciled with our observations from the perspective of partial melts,

577 which does not require the presence of “residual” crystalline MSS controlling Se–Te partitioning (Fig. 9a) as
578 previously suggested by the Cu–Ag systematics (Jenner et al., 2015; Wang and Becker, 2015b) as well as recent
579 sulfide melting experiments (Zhang Z. and Hirschmann, 2016; Zhang Z. et al., 2018; Fig. 7; Section 5.3.1). We
580 argue that, from the melt perspective, secondary refertilization processes such as addition of metasomatic base
581 metal sulfides and platinum-group minerals have significantly, if not completely, overprinted the original melt
582 depletion signature of lherzolites (i.e., sulfide liquid–silicate melt fractionation; Fig. 9b and c), in line with the
583 conclusions from studies of peridotites (Lorand and Alard, 2010; König et al., 2014, 2015; Luguet et al., 2015;
584 Harvey et al., 2015). Note that this argument is independent of the choice of source Se–Te contents and published
585 experimental $D_{Se\ or\ Te}^{sulf\ liq-sil}$. For instance, the residue composition was also calculated with a source having the
586 maximum “fertile mantle” Se and Te contents (101 and 12.5 ng g⁻¹, respectively; estimated at 4.45 wt.% Al₂O₃;
587 Wang and Becker, 2013) using $D_{Se\ or\ Te}^{bulk}$ from both studies (Brenan, 2015; Kiseeva et al., 2017). Results show
588 that the modelled residue composition still hardly reconciles with the observed Se–Te variation in lherzolites,
589 which likely represent a post-melt depletion refertilization trend (Fig. 9b and c). As for the highly depleted
590 residue after sulfide exhaustion, little is known regarding the quantitative control of Se–Te host phases.
591 Nevertheless, the increasing Se/Te ratios (>15; suprachondritic relative to CI chondrites; Lodders et al., 2009)
592 with progressive melt depletion in refractory harzburgites, which represent the least metasomatically influenced
593 peridotites (König et al., 2014; Luguet et al., 2015), probably reflects the relatively compatible behavior of Se
594 that is preferentially incorporated in platinum-group minerals formed upon sulfide exhaustion (Luguet and
595 Reisberg, 2016; Luguet et al., 2007; Fonseca et al., 2012; König et al., 2015).

596 **5.4. Role of magmatic processes on Se isotope systematics of MORB**

597 Having established the Se (and Te) elemental behavior during partial melting and MORB differentiation,
598 we now discuss the role of these magmatic processes on Se isotopes and estimate a reliable mantle source
599 composition. Note that none of the (secondary) non-magmatic processes, including high-T hydrothermal
600 fluid/sulfide assimilation during magmatic differentiation and volcanic degassing, have measurable effects on
601 Se isotope composition of PAR glasses (Section 5.1).

602 Previous experiments reported significant Se isotopic fractionation (up to 19‰ in ⁸²Se/⁷⁶Se) during abiotic
603 reduction of Se oxyanions (SeO₃²⁻ and SeO₄²⁻) at low temperature conditions (e.g., Krouse and Thode, 1962;
604 Rees and Thode, 1966; Rashid and Krouse, 1985; Johnson et al., 1999; Johnson and Bullen, 2003; Mitchell et
605 al., 2013). In contrast, there is little isotopic fractionation (<0.5‰) associated with oxidation of reduced Se
606 species (Johnson et al., 1999; Johnson, 2004). As discussed in Section 5.1, Se is very likely dissolved in MORB
607 melts as reduced Se²⁻. Since MORB forms and evolves at *f*O₂ around FMQ buffer (Ballhaus, 1993; Bézou and
608 Humler, 2005; Cottrell and Kelley, 2011; Labidi et al., 2014; Zhang H. L. et al., 2018), transition between Se⁴⁺
609 (with/without Se⁶⁺) and Se²⁻ and hence associated Se isotopic fractionation, if any, is expected to be very subtle
610 across the entire MORB evolution starting from the mantle source region.

611 Despite the narrow range in $\delta^{82/76}\text{Se}$ values of the PAR glasses ($-0.16 \pm 0.13\%$), subtle but resolvable
612 differences (up to $\sim 0.25\%$ vs the external reproducibility of 0.09%) is observed between some samples (Fig. 3).
613 These differences seem to be unrelated to the sample latitude, tectonic discontinuity, or ridge axial depth (Fig.
614 2a and b; Supplementary Fig. S1). Hamelin et al. (2011) demonstrated clear latitudinal variations in radiogenic
615 isotopes (He–Sr–Nd–Hf–Pb) along the studied PAR segments ($65\text{--}56^\circ\text{S}$ and $53\text{--}41^\circ\text{S}$), which is interpreted to
616 result from progressive mixing of the depleted Pacific upper mantle and gradually increasing amount of recycled
617 oceanic crust component northwards. However, Se isotope compositions of the northern and southern PAR
618 segments are essentially the same ($-0.14 \pm 0.12\%$ and $-0.19 \pm 0.14\%$, respectively; 2 s.d.) and show no clear
619 latitudinal variation (Fig. 2a). There is also no covariation between $\delta^{82/76}\text{Se}$ (or Se–Te contents) and radiogenic
620 isotope ratios of the samples (not shown). Furthermore, the Se isotopic variations are not correlated with (1) Se
621 content of the melt ($158\text{--}219 \text{ ng g}^{-1}$; Fig. 2c), (2) magmatic differentiation index Mg# ($0.68\text{--}0.40$; Fig. 10a), or
622 (3) Se/Te ratio ($\sim 43\text{--}189$) that is demonstrated above as a direct indicator of sulfide liquid–silicate melt
623 fractionation (Fig. 4c and 10b; Section 5.2.1). Besides, two highly evolved PAR glasses that show clear evidence
624 of magnetite-triggered sulfide fractionation (PAC1DR10-1g and PAC2 DR20-1; Fig. 4c and e) have Se isotope
625 compositions ($-0.24 \pm 0.09\%$ and $-0.15 \pm 0.09\%$) indistinguishable from those of less evolved samples
626 ($\text{MgO} > 5\text{wt.}\%$). As discussed earlier, the predominantly fractionating sulfide phase in response to liquidus
627 magnetite appearance after $\text{MgO} < 5\text{wt.}\%$ is very likely crystalline MSS. Altogether, we suggest that there is no
628 resolvable Se isotopic fractionation within uncertainty (0.09% ; 2 s.d.) during shallow-level magmatic
629 differentiation that involves segregation of silicate crystals and sulfide liquid and/or MSS (i.e., $\Delta^{82/76}\text{Se}_{\text{sulf-sil}} \approx$
630 0.00%). Effects of pressure on Se isotopic partitioning at mantle conditions relevant to MORB petrogenesis (Fig.
631 7) is expected to be negligible (Young et al., 2015), as in the case of S isotopes (Labidi and Cartigny, 2016). We
632 therefore argue that there is negligible $^{82}\text{Se}/^{76}\text{Se}$ fractionation during partial melting of the upper mantle, which
633 also involves equilibrium partitioning of Se between sulfide liquid (probably without MSS) and silicate melt
634 (Fig. 8 and 9; Supplementary Fig. S5; see Section 5.3.3). Accordingly, we use the observed PAR MORB average
635 $\delta^{82/76}\text{Se}$ ($-0.16 \pm 0.13\%$; $n = 27$) to represent the Se isotope composition of the primary melts ($\text{Mg}\# = 0.73$) as
636 well as the mantle source (Fig. 10a and b). The apparent Se isotope variation along the PAR (up to $0.25 \pm 0.13\%$;
637 e.g., Fig. 2 and 3) thus likely reflects intrinsic mantle heterogeneity.

638 The $\delta^{82/76}\text{Se}$ values of the PAR MORBs are systematically lighter than that of all other basaltic lavas from
639 various geological settings (e.g., oceanic/continental intraplate basalts and plume-influenced ocean ridge basalts;
640 Fig. 3; Rouxel et al., 2002; Kurzawa et al., 2017; Yierpan et al., 2018; this study). Four subaerial basalts analyzed
641 by the same technique as in this study have variable Se ($\sim 15\text{--}170 \text{ ng g}^{-1}$) and Te ($1.0\text{--}14.2 \text{ ng g}^{-1}$) contents with
642 Se/Te ratios $\sim 3\text{--}65$ (Fig. 10b; Yierpan et al., 2018), implying that they may have different source compositions
643 and/or experienced different degrees of partial melting and igneous differentiation (see Section 5.2 and 5.3).
644 These petrogenetic processes however should result in no Se isotopic fractionation as discussed above. Their
645 non-chondritic and significantly heavier $\delta^{82/76}\text{Se}$ ($+0.21 \pm 0.15\%$) compared to MORB could thus reflect (1) so

646 far unidentified effects of non-magmatic processes (such as subaerial eruption-related degassing; e.g., Floor and
647 Román-Ross, 2012; Floor et al., 2013) and/or (2) Se isotopic variability among terrestrial igneous reservoirs
648 ($\delta^{82/76}\text{Se}$ between $-0.16 \pm 0.13\%$ and $+0.21 \pm 0.15\%$; Fig. 3 and 10b).

649 **5.5. Implications for the origin of Se and Te in the mantle**

650 The upper mantle abundances of Se, Te, and S have been suggested to be primarily established by addition
651 of volatile-rich chondritic late veneer after core formation (Wang and Becker, 2013) because these elements are
652 predicted to behave as highly siderophile elements during core–mantle differentiation based on the extrapolation
653 of low-P (1–19 GPa) metal–silicate partitioning experiments (Rose-Weston et al., 2009; Steenstra et al., 2017).
654 However, this simple late-veneer origin of S cannot explain the non-chondritic S isotope composition of the
655 mantle, which requires a significant portion of S in the pre-late veneer mantle (Labidi et al., 2013, 2016). This
656 is further supported by more recent partitioning experiments on S (Boujibar et al., 2014; Suer et al., 2017). Suer
657 et al. (2017) showed that S becomes less siderophile with increasing pressure than previously predicted, with the
658 observed $D_S^{\text{metal-silicate}}$ of $\sim 10\text{--}55$ versus ~ 1000 predicted by Rose-Weston et al. (2009), at core forming condition
659 ($\sim 40\text{--}55$ GPa; Jackson et al., 2018). In this context, if the late veneer consisted of volatile-rich materials (e.g.,
660 McDonough and Sun, 1995; Wang and Becker, 2013), suprachondritic S/Se and S/Te ratios should be expected
661 for the mantle because the Se–Te budget was primarily accounted for by late veneer; alternatively, if the pressure
662 dependence of $D_{\text{Se or Te}}^{\text{metal-silicate}}$ determined at <20 GPa (Rose-Weston et al., 2009; Steenstra et al., 2017) was
663 lowered at higher pressure (or temperature) to some extent as in the case of S (Suer et al., 2017) and other
664 elements (e.g., Siebert et al., 2013), the possibility that mantle Se–Te budget represents metal–silicate
665 equilibration would remain open (as suggested for the Moon; Steenstra et al., 2017).

666 As discussed earlier, lithospheric lherzolites that were used to estimate PM Se–Te abundances (Wang and
667 Becker, 2013) preserve little primary melt depletion signature and very likely represent refertilized (previously-
668 depleted) harzburgites (Fig. 9b and c; also see Le Roux et al., 2007; König et al., 2014). Unlike Cu and Ag that
669 show limited fractionation during different petrogenetic processes (e.g., mantle melting, refertilization, and melt
670 transport; Wang and Becker, 2015b), different and non-systematic Se–Te fractionation occurs during these
671 processes depending on the host assemblages controlling the Se–Te behavior (Fig. 4, 6, and 9b and c; Section
672 5.3.3). This implies that the near-chondritic Se/Te ratios (7.9 ± 1.6) in worldwide “fertile lherzolites”, despite
673 the broad correlation between Se–Te and lithophile elements such as Al and Ca (Wang and Becker, 2013), should
674 be considered with great caution as primitive signature of PM.

675 Mantle melts provide an alternative approach to estimate composition of the asthenospheric mantle. The
676 MORB mantle abundances of Se–Te and other strongly chalcophile elements (e.g., Cu; Supplementary Fig. S5)
677 would be essentially identical to that of PM (Fig. 9b and c) because average depleted MORB mantle is only $\sim 2\text{--}$
678 3% melt-depleted from PM (Menzies et al., 1977; Salters and Stracke, 2004; Workman and Hart, 2005; Bodinier
679 and Godard, 2014). However, this approach critically depends on the modelling parameters (Section 5.2.2 and

680 5.3.3) and hence leads to different results (Fig. 8 and 9). We obtain two distinct possible source compositions
681 for the PAR MORB: $80 \pm 17 \text{ ng g}^{-1} \text{ Se}$ and $11 \pm 1.7 \text{ ng g}^{-1} \text{ Te}$ (source 1; “fertile lherzolite-like”; Wang and
682 Becker, 2013) vs $49 \pm 11 \text{ ng g}^{-1} \text{ Se}$ and $3.5 \pm 1.3 \text{ ng g}^{-1} \text{ Te}$ (source 2) due to the difference in $D_{\text{Se or Te}}^{\text{sulf liq-sil}}$
683 published by Brenan (2015) and Kiseeva et al. (2017), respectively (Table 3; Fig. 9 and 10). Note that only
684 $D_{\text{Se or Te}}^{\text{sulf liq-sil}}$ from the latter study successfully reproduces the observed Se–Te variation during MORB
685 differentiation (Fig. 6b and c; Section 5.2.1).

686 On the other hand, $\delta^{82/76}\text{Se}$ of PAR MORB mantle ($-0.16 \pm 0.13\text{‰}$) is well within the range of chondritic
687 values of $-0.30 \pm 0.39\text{‰}$ (Vollstaedt et al., 2016) and $-0.21 \pm 0.31\text{‰}$ (Labidi et al., 2018) (Fig. 3). Combined
688 with the possible Se/Te ratios (7.9 ± 1.6 and 14.0 ± 6.1 for source 1 and 2, respectively), $\delta^{82/76}\text{Se}$ of the PAR
689 mantle appears to overlap with that of both CI chondrites and volatile-depleted carbonaceous (CV and CO) and
690 ordinary chondrites but show a significant offset from enstatite chondrites (Fig. 10b). Yet, the latter have been
691 suggested to be the main constituent of the late veneer based on Ru and Os isotopes (e.g., Meisel et al., 1996;
692 Dauphas, 2017; Fischer-Gödde and Kleine, 2017). Interestingly, all terrestrial rocks/melts show distinctly
693 heavier $\delta^{82/76}\text{Se}$ relative to enstatite chondrites (Fig. 3). At this stage, it is difficult to link the late veneer material
694 to certain chondrite groups because a robust mantle $\delta^{82/76}\text{Se}$ value remains to be established and little is known
695 regarding the role of planetary processes on moderately volatile Se isotopes (e.g., metal–silicate equilibration
696 and vapor loss during accretionary growth of small planetesimals; Labidi et al., 2016; Hin et al., 2017; Norris
697 and Wood, 2017). Our result obtained here however highlights the potential of Se isotopes to contribute new
698 constraints on planetary accretion models regarding the Earth’s volatile delivery.

699 **6. Conclusion**

700 We present the first high-precision Se isotope and Se–Te elemental data for MORB glasses from the PAR
701 ($65\text{--}56^\circ\text{S}$ and $53\text{--}41^\circ\text{S}$) using recently developed analytical techniques (Kurzawa et al., 2017; Yierpan et al.,
702 2018). Almost all PAR basalts have experienced high-temperature hydrothermal fluid assimilation during
703 magmatic differentiation, which significantly overprints the S isotope composition when it is associated with
704 assimilation of hydrothermal sulfides (Labidi et al., 2014). However, neither of these processes affects the Se
705 isotope composition and S–Se–Te abundances. The observed S–Se–Te variation is dominantly controlled by
706 MORB differentiation involving segregation of immiscible sulfide liquid, which are successfully reproduced
707 using the experimentally determined $D_{\text{Se or Te}}^{\text{sulf liq-sil}}$ values from Kiseeva et al. (2017); in the highly evolved melts at
708 magnetite saturation, the dominant fractionating sulfide phase is very likely crystalline MSS, indicated by the
709 abrupt drop in Se/Te and S/Te ratios. The differentiation-corrected Se–Te contents of the primary MORB melts
710 are well reproduced by near-fractional decompression melting of a mantle using experimental $D_{\text{Se or Te}}^{\text{sulf liq-sil}}$ (Brenan,
711 2015; Kiseeva et al., 2017) with a mantle source containing $170\text{--}200 \mu\text{g g}^{-1} \text{ S}$ but distinct Se–Te contents (“fertile
712 lherzolite-like” 80 ± 17 and $11 \pm 1.7 \text{ ng g}^{-1}$ vs 49 ± 11 and $3.5 \pm 1.3 \text{ ng g}^{-1}$ Se and Te, respectively) due to the
713 significant difference in $D_{\text{Se or Te}}^{\text{sulf liq-sil}}$ reported by these groups. Nevertheless, our model suggests that sulfide

714 liquid–silicate melt partitioning, rather than MSS–sulfide liquid or MSS–silicate melt partitioning,
715 predominantly controls the partitioning behavior of chalcophile elements during melting of a MORB mantle, in
716 accordance with recent sulfide melting experiments (Zhang Z. and Hirschmann, 2016; Zhang Z. et al., 2018).
717 This reinforces the notion that Se–Te variations (with broadly-chondritic Se/Te ratios) in “static” lithospheric
718 lherzolites reflect significant, if not complete, metasomatic overprinting (e.g., König et al., 2014), which in turn
719 requires a reassessment of the current PM composition (Wang and Becker, 2013).

720 The observed Se isotope variation along the PAR ($-0.30 \pm 0.09\%$ – $-0.05 \pm 0.09\%$; 2 s.d., $n = 27$) is not
721 systematically related to magmatic differentiation involving sulfide liquid/MSS–silicate melt partitioning or
722 other geochemical parameters, indicating negligible $^{82}\text{Se}/^{76}\text{Se}$ fractionation within uncertainty during
723 decompression melting. The Se isotope composition of the Pacific mantle is thus represented by the average
724 $\delta^{82/76}\text{Se}$ of all MORBs ($-0.16 \pm 0.13\%$). This value is significantly lighter than previously reported $\delta^{82/76}\text{Se}$ for
725 basalts and one peridotite from diverse geodynamic settings (Rouxel et al., 2002; Kurzawa et al., 2017; Yierpan
726 et al., 2018); meanwhile, it overlaps with $\delta^{82/76}\text{Se}$ of carbonaceous (CI and volatile depleted CV and CO) and
727 ordinary chondrites but shows a distinct offset from that of enstatite chondrites (Labidi et al., 2018). Selenium
728 isotope variations between different mantle reservoirs and in additional non-magmatic processes can be resolved
729 and further investigated in order to contribute constraints on the accretion history of terrestrial volatiles.

730

731 **Acknowledgements**

732 This work was supported by the ERC Starting Grant, O2RIGIN (636808), to Stephan König. We are
733 grateful to Timon Kurzawa, Martin Wille, Elmar Reitter, and Ilka Kleinhanns for their generous support in the
734 lab, and Bernd Steinhilber and Johannes Redlinger for the trace element analysis. Laure Dosso kindly provided
735 the PAR MORB samples. The manuscript greatly benefited from careful reviews and constructive comments by
736 three anonymous reviewers as well as editors Shichun Huang, Marc Norman, and Jeffrey Catalano.

737

738 **References**

- 739 Adams R. D. (1964). Thickness of the Earth's Crust beneath the Pacific-Antarctic Ridge. *New Zealand Journal of*
740 *Geology and Geophysics*, **7**(3), 529-542.
- 741 Albut G., Babechuk M. G., Kleinhanns I. C., Bengel M., Beukes N. J., Steinhilber B., Smith A. J. B., Kruger S. J. and
742 Schoenberg R. (2018). Modern rather than Mesoarchaeon oxidative weathering responsible for the heavy stable
743 Cr isotopic signatures of the 2.95 Ga old Ijzermijn iron formation (South Africa). *Geochimica et Cosmochimica*
744 *Acta*, **228**, 157-189.
- 745 Allègre C., Manhès G. and Lewin E. (2001). Chemical composition of the Earth and the volatility control on planetary
746 genetics. *Earth and Planetary Science Letters*, **185**(1-2), 49-69.
- 747 Ariskin A. A., Danyushevsky L. V., Bychkov K. A., McNeill A. W., Barmina G. S. and Nikolaev G. S. (2013).
748 Modeling Solubility of Fe-Ni Sulfides in Basaltic Magmas: The Effect of Nickel. *Economic Geology*, **108**(8),
749 1983-2003.

750 Ariskin A. A., Bychkov K. A., Nikolaev G. S. and Barmina G. S. (2018). The COMAGMAT-5: Modeling the Effect
751 of Fe–Ni Sulfide Immiscibility in Crystallizing Magmas and Cumulates. *Journal of Petrology*, **59**(2), 283-298.

752 Asimow P. D. and Longhi J. (2004). The significance of multiple saturation points in the context of polybaric near-
753 fractional melting. *Journal of Petrology*, **45**(12), 2349-2367.

754 Babechuk M. G., Kamber B. S., Greig A., Canil D. and Kodolanyi J. (2010). The behaviour of tungsten during mantle
755 melting revisited with implications for planetary differentiation time scales. *Geochimica et Cosmochimica Acta*,
756 **74**(4), 1448-1470.

757 Ballhaus C. (1993). Redox states of lithospheric and asthenospheric upper mantle. *Contributions to Mineralogy and
758 Petrology*, **114**(3), 331-348.

759 Ballhaus C., Bockrath C., Wohlgemuth-Ueberwasser C., Laurenz V. and Berndt J. (2006). Fractionation of the noble
760 metals by physical processes. *Contributions to Mineralogy and Petrology*, **152**(6), 667-684.

761 Barnes S.-J., Savard D., Bédard L. P. and Maier W. D. (2009). Selenium and sulfur concentrations in the Bushveld
762 Complex of South Africa and implications for formation of the platinum-group element deposits. *Mineralium
763 Deposita*, **44**(6), 647-663.

764 Bezard R., Fischer-Gödde M., Hamelin C., Brennecke G. A. and Kleine T. (2016). The effects of magmatic processes
765 and crustal recycling on the molybdenum stable isotopic composition of Mid-Ocean Ridge Basalts. *Earth and
766 Planetary Science Letters*, **453**, 171-181.

767 Bézos A. and Humler E. (2005). The Fe³⁺/ΣFe ratios of MORB glasses and their implications for mantle melting.
768 *Geochimica et Cosmochimica Acta*, **69**(3), 711-725.

769 Bézos A., Lorand J. P., Humler E. and Gros M. (2005). Platinum-group element systematics in Mid-Oceanic Ridge
770 basaltic glasses from the Pacific, Atlantic, and Indian Oceans. *Geochimica et Cosmochimica Acta*, **69**(10), 2613-
771 2627.

772 Bockrath C., Ballhaus C. and Holzheid A. (2004). Fractionation of the platinum-group elements during mantle melting.
773 *Science*, **305**(5692), 1951-3.

774 Bodinier J.-L. and Godard M. (2014). Orogenic, Ophiolitic, and Abyssal Peridotites. In: Holland H. D., Turekian K.
775 K. (Eds.), *Treatise on Geochemistry (Second Edition)*. Elsevier, Oxford, pp. 103-167.

776 Boujibar A., Andrault D., Bouhifd M. A., Bolfan-Casanova N., Devidal J.-L. and Trcera N. (2014). Metal–silicate
777 partitioning of sulphur, new experimental and thermodynamic constraints on planetary accretion. *Earth and
778 Planetary Science Letters*, **391**, 42-54

779 Brenan J. M. (2015). Se–Te fractionation by sulfide–silicate melt partitioning: Implications for the composition of
780 mantle-derived magmas and their melting residues. *Earth and Planetary Science Letters*, **422**, 45-57.

781 Brookins D. G. (1988). Eh-pH Diagrams for Geochemistry. Springer-Verlag, Berlin, Heidelberg.

782 Carignan J. and Wen H. J. (2007). Scaling NIST SRM 3149 for Se isotope analysis and isotopic variations of natural
783 samples. *Chemical Geology*, **242**(3-4), 347-350.

784 Castillo P. R., Natland J. H., Niu Y. and Lonsdale P. F. (1998). Sr, Nd and Pb isotopic variation along the Pacific–
785 Antarctic rise/crest, 53–57°S: Implications for the composition and dynamics of the South Pacific upper mantle.
786 *Earth and Planetary Science Letters*, **154**(1-4), 109-125.

787 Choi N. and Cho W. D. (1997). Distribution behavior of cobalt, selenium, and tellurium between nickel-copper-iron
788 matte and silica-saturated iron silicate slag. *Metallurgical and Materials Transactions B*, **28**(3), 429-438.

789 Clog M., Aubaud C., Cartigny P. and Dosso L. (2013). The hydrogen isotopic composition and water content of
790 southern Pacific MORB: A reassessment of the D/H ratio of the depleted mantle reservoir. *Earth and Planetary
791 Science Letters*, **381**, 156-165.

792 Coogan L. A. and Dosso S. E. (2016). Quantifying Parental MORB Trace Element Compositions from the Eruptive
793 Products of Realistic Magma Chambers: Parental MORB are Depleted. *Journal of Petrology*, **57**(11-12),
794 2105-2126.

795 Cottrell E. and Kelley K. A. (2011). The oxidation state of Fe in MORB glasses and the oxygen fugacity of the upper
796 mantle. *Earth and Planetary Science Letters*, **305**(3-4), 270-282.

797 Cutter G. A. and Bruland K. W. (1984). The marine biogeochemistry of selenium: A re-evaluation 1. *Limnology and
798 Oceanography*, **29**(6), 1179-1192.

799 Cutter G. A. and Cutter L. S. (2001). Sources and cycling of selenium in the western and equatorial Atlantic Ocean.
800 *Deep-Sea Research Part II: Topical Studies in Oceanography*, **48**(13), 2917-2931.

801 Dauphas N. (2017). The isotopic nature of the Earth's accreting material through time. *Nature* **541**, 521.

- 802 Dare S. A. S., Barnes S. J. and Beaudoin G. (2012). Variation in trace element content of magnetite crystallized from
803 a fractionating sulfide liquid, Sudbury, Canada: Implications for provenance discrimination. *Geochimica et*
804 *Cosmochimica Acta*, **88**, 27-50.
- 805 Dare S. A. S., Barnes S. J., Beaudoin G., Meric J., Boutroy E. and Potvin-Doucet C. (2014). Trace elements in
806 magnetite as petrogenetic indicators. *Mineralium Deposita*, **49**(7), 785-796.
- 807 Ding S. and Dasgupta R. (2017). The fate of sulfide during decompression melting of peridotite implications for sulfur
808 inventory of the MORB-source depleted upper mantle. *Earth and Planetary Science Letters*, **459**, 183-195.
- 809 Falconer R. K. H. (1972). The Indian-Antarctic-Pacific triple junction. *Earth and Planetary Science Letters*, **17**(1),
810 151-158.
- 811 Fang L. and Lynch D. C. (1987). Evaluation of the Behavior of Selenium in Silicate Slag. *Metallurgical Transactions*
812 *B-Process Metallurgy*, **18**(1), 181-187.
- 813 Fischer-Gödde M. and Kleine T. (2017). Ruthenium isotopic evidence for an inner Solar System origin of the late
814 veneer. *Nature*, **541**, 525.
- 815 Fischer-Gödde M., Becker H. and Wombacher F. (2011). Rhodium, gold and other highly siderophile elements in
816 orogenic peridotites and peridotite xenoliths. *Chemical Geology*, **280**, 365-383.
- 817 Floor G. H. and Román-Ross G. (2012). Selenium in volcanic environments: A review. *Applied Geochemistry*, **27**(3),
818 517-531.
- 819 Floor G. H., Margui E., Hidalgo M., Queralt I., Kregsamer P., Strelci C. and Román-Ross G. (2013). Study of selenium
820 sorption processes in volcanic ash using Total Reflection X-ray Fluorescence (TXRF). *Chemical Geology*, **352**,
821 19-26.
- 822 Floor G. H., Millot R., Iglesias M. and Negrel P. (2011). Influence of methane addition on selenium isotope sensitivity
823 and their spectral interferences. *J Mass Spectrom*, **46**(2), 182-188.
- 824 Fonseca R. O. C., Laurenz V., Mallmann G., Lugué A., Hoehne N. and Jochum K. P. (2012). New constraints on the
825 genesis and long-term stability of Os-rich alloys in the Earth's mantle. *Geochimica et Cosmochimica Acta*, **87**,
826 227-242.
- 827 Francheteau J., Yelles-Chaouche A. and Craig H. (1987). The Juan Fernandez microplate north of the Pacific-Nazca-
828 Antarctic plate junction at 35°S. *Earth and Planetary Science Letters*, **86**(2-4), 253-268.
- 829 Gale A., Dalton C. A., Langmuir C. H., Su Y. and Schilling J.-G. (2013). The mean composition of ocean ridge basalts.
830 *Geochemistry, Geophysics, Geosystems*, **14**, 489-518.
- 831 Geli L., Bougault H., Aslanian D., Briais A., Dosso L., Etoubleau J., LeFormal J. P., Maia M., Ondreas H., Olivet J.
832 L., Richardson C., Sayanagi K., Seama N., Shah A., Vlastelic I. and Yamamoto M. (1997). Evolution of the
833 Pacific-Antarctic Ridge south of the Udintsev fracture zone. *Science*, **278**(5341), 1281-1284.
- 834 Ghiorso M. S., Hirschmann M. M., Reiners P. W. and Kress V. C. (2002). The pMELTS: A revision of MELTS for
835 improved calculation of phase relations and major element partitioning related to partial melting of the mantle to
836 3 GPa. *Geochemistry, Geophysics, Geosystems*, **3**, 1-35.
- 837 Ghiorso M. S. and Sack R. O. (1995). Chemical mass transfer in magmatic processes IV. A revised and internally
838 consistent thermodynamic model for the interpolation and extrapolation of liquid-solid equilibria in magmatic
839 systems at elevated temperatures and pressures. *Contributions to Mineralogy and Petrology*, **119**(2-3), 197-212.
- 840 Greaney A. T., Rudnick R. L., Helz R. T., Gaschnig R. M., Piccoli P. M. and Ash R. D. (2017). The behavior of
841 chalcophile elements during magmatic differentiation as observed in Kilauea Iki lava lake, Hawaii. *Geochimica et*
842 *Cosmochimica Acta*, **210**, 71-96.
- 843 Guo J. F., Griffin W. L. and O'Reilly S. Y. (1999). Geochemistry and origin of sulphide minerals in mantle xenoliths:
844 Qilin, southeastern China. *Journal of Petrology*, **40**(7), 1125-1149.
- 845 Hamelin C., Dosso L., Hanan B., Barrat J.-A. and Ondréas H. (2010). Sr-Nd-Hf isotopes along the Pacific Antarctic
846 Ridge from 41 to 53°S. *Geophysical Research Letters*, **37**(10).
- 847 Hamelin C., Dosso L., Hanan B. B., Moreira M., Kositsky A. P. and Thomas M. Y. (2011). Geochemical portray of
848 the Pacific Ridge: New isotopic data and statistical techniques. *Earth and Planetary Science Letters*, **302**(1-2),
849 154-162.
- 850 Hannington M. D., Peterson S., Herzig P.M. and Jonasson I.R. (2004) A global database of seafloor hydrothermal
851 systems, including a digital database of geochemical analyses of seafloor polymetallic sulfides. *Geological Survey*
852 *of Canada*, Open File, Report 4598, 1 CD-ROM.
- 853 Hart S. R. and Gaetani G. A. (2006). Mantle Pb paradoxes: the sulfide solution. *Contributions to Mineralogy and*

854 *Petrology*, **152**(3), 295-308.

855 Harvey J., König S. and Luguet A. (2015). The effects of melt depletion and metasomatism on highly siderophile and
856 strongly chalcophile elements: S–Se–Te–Re–PGE systematics of peridotite xenoliths from Kilbourne Hole, New
857 Mexico. *Geochimica et Cosmochimica Acta*, **166**, 210-233.

858 Hattori K. H., Arai S. and Clarke D. B. (2002). Selenium, tellurium, arsenic and antimony contents of primary mantle
859 sulfides. *Canadian Mineralogist*, **40**, 637-650.

860 Helmy H. M., Ballhaus C., Wohlgemuth-Ueberwasser C., Fonseca R. O. C. and Laurenz V. (2010). Partitioning of Se,
861 As, Sb, Te and Bi between monosulfide solid solution and sulfide melt - Application to magmatic sulfide deposits.
862 *Geochimica et Cosmochimica Acta*, **74**(21), 6174-6179.

863 Hertogen J., Janssens M. J. and Palme H. (1980). Trace elements in ocean ridge basalt glasses: implications for
864 fractionations during mantle evolution and petrogenesis. *Geochimica et Cosmochimica Acta*, **44**(12), 2125-2143.

865 Hin R. C., Coath C. D., Carter P. J., Nimmo F., Lai Y. J., von Strandmann P. A. E. P., Willbold M., Leinhardt Z. M.,
866 Walter M. J. and Elliott T. (2017). Magnesium isotope evidence that accretional vapour loss shapes planetary
867 compositions. *Nature*, **549**(7673), 511-515.

868 Hofmann A. W. (1988). Chemical Differentiation of the Earth - the Relationship between Mantle, Continental-Crust,
869 and Oceanic-Crust. *Earth and Planetary Science Letters*, **90**(3), 297-314.

870 Jackson C. R. M., Bennett N. R., Du Z., Cottrell E. and Fei Y. (2018). Early episodes of high-pressure core formation
871 preserved in plume mantle. *Nature* **553**(7689), 491-495.

872 Jain J. C., Field M. P., Neal C. R., Ely J. C. and Sherrell R. M. (2000). Determination of the REE in Geological
873 Reference Materials DTS-1 (Dunite) and PCC-1 (Peridotite) by Ultrasonic and Microconcentric Desolvating
874 Nebulisation ICP-MS. *Geostandards and Geoanalytical Research*, **24**(1), 65-72.

875 Jenner F. E. and O'Neill H. S. (2012). Analysis of 60 elements in 616 ocean floor basaltic glasses. *Geochemistry
876 Geophysics Geosystems*, **13**, Q02005.

877 Jenner F. E., Arculus R. J., Mavrogenes J. A., Dyriw N. J., Nebel O. and Hauri E. H. (2012). Chalcophile element
878 systematics in volcanic glasses from the northwestern Lau Basin. *Geochemistry, Geophysics, Geosystems*, **13**,
879 Q06014.

880 Jenner F. E., Hauri E. H., Bullock E. S., König S., Arculus R. J., Mavrogenes J. A., Mikkelsen N. and Goddard C.
881 (2015). The competing effects of sulfide saturation versus degassing on the behavior of the chalcophile elements
882 during the differentiation of hydrous melts. *Geochemistry, Geophysics, Geosystems*, **16**, 1490-1507.

883 Jenner F. E., O'Neill H. S. C., Arculus R. J. and Mavrogenes J. A. (2010). The Magnetite Crisis in the Evolution of
884 Arc-related Magmas and the Initial Concentration of Au, Ag and Cu. *Journal of Petrology*, **53**(5), 1089-1089.

885 Jochum K. P., Nohl L., Herwig K., Lammel E., Stoll B. and Hofmann A. W. (2005). GeoReM: A new geochemical
886 database for reference materials and isotopic standards. *Geostandards and Geoanalytical Research*, **29**(3), 333-
887 338.

888 Johnson T. M. (2004). A review of mass-dependent fractionation of selenium isotopes and implications for other
889 heavy stable isotopes. *Chemical Geology*, **204**(3-4), 201-214.

890 Johnson T. M. and Bullen T. D. (2003). Selenium isotope fractionation during reduction by Fe(II)-Fe(III) hydroxide-
891 sulfate (green rust). *Geochimica et Cosmochimica Acta*, **67**(3), 413-419.

892 Johnson T. M., Herbel M. J., Bullen T. D. and Zawislanski P. T. (1999). Selenium isotope ratios as indicators of
893 selenium sources and oxyanion reduction. *Geochimica et Cosmochimica Acta*, **63**(18), 2775-2783.

894 Katz R. F., Spiegelman M. and Langmuir C. H. (2003). A new parameterization of hydrous mantle melting.
895 *Geochemistry Geophysics Geosystems*, **4**, 1073.

896 Keith M., Haase K. M., Klemm R., Krumm S. and Strauss H. (2016). Systematic variations of trace element and sulfur
897 isotope compositions in pyrite with stratigraphic depth in the Skouriotissa volcanic-hosted massive sulfide deposit,
898 Troodos ophiolite, Cyprus. *Chemical Geology*, **423**, 7-18.

899 Keith M., Haase K. M., Klemm R., Schwarz-Schampera U. and Franke H. (2017). Systematic variations in magmatic
900 sulphide chemistry from mid-ocean ridges, back-arc basins and island arcs. *Chemical Geology*, **451**, 67-77.

901 Kelley K. A., Plank T., Grove T. L., Stolper E. M., Newman S. and Hauri E. (2006). Mantle melting as a function of
902 water content beneath back-arc basins. *Journal of Geophysical Research*, **111**(B9).

903 Kimura J.-I., Gill J. B., van Keken P. E., Kawabata H. and Skora S. (2017). Origin of geochemical mantle components:
904 Role of spreading ridges and thermal evolution of mantle. *Geochemistry, Geophysics, Geosystems*, **18**(2), 697-734.

- 905 Kinzler R. J. and Grove T. L. (1993). Corrections and further discussion of the primary magmas of mid-ocean ridge
906 basalts, 1 and 2. *Journal of Geophysical Research: Solid Earth*, **98**(B12), 22339-22347.
- 907 Kiseeva E. S., Fonseca R. O. C. and Smythe D. J. (2017). Chalcophile Elements and Sulfides in the Upper Mantle.
908 *Elements*, **13**(2), 111-116.
- 909 Kiseeva E. S. and Wood B. J. (2015). The effects of composition and temperature on chalcophile and lithophile
910 element partitioning into magmatic sulphides. *Earth and Planetary Science Letters*, **424**, 280-294.
- 911 Klein E. M. and Langmuir C. H. (1987). Global Correlations of Ocean Ridge Basalt Chemistry with Axial Depth and
912 Crustal Thickness. *Journal of Geophysical Research-Solid Earth and Planets*, **92**(B8), 8089-8115.
- 913 Klingelhofer F., Ondréas H., Briais A., Hamelin C. and Dosso L. (2006). New structural and geochemical
914 observations from the Pacific-Antarctic Ridge between 52°45'S and 41°15'S. *Geophysical Research Letters*,
915 **33**(21).
- 916 König S., Eickmann B., Zack T., Yierpan A., Wille M., Taubald H. and Schoenberg R. (2019). Redox induced sulfur-
917 selenium isotope decoupling recorded in pyrite. *Geochimica et Cosmochimica Acta*, **244**, 24-39.
- 918 König S., Lissner M., Lorand J. P., Bragagni A. and Luguet A. (2015). Mineralogical control of selenium, tellurium
919 and highly siderophile elements in the Earth's mantle: Evidence from mineral separates of ultra-depleted mantle
920 residues. *Chemical Geology*, **396**, 16-24.
- 921 König S., Lorand J. P., Luguet A. and Pearson D. G. (2014). A non-primitive origin of near-chondritic S–Se–Te ratios
922 in mantle peridotites; implications for the Earth's late accretionary history. *Earth and Planetary Science Letters*,
923 **385**, 110-121.
- 924 König S., Luguet A., Lorand J.-P., Wombacher F. and Lissner M. (2012). Selenium and tellurium systematics of the
925 Earth's mantle from high precision analyses of ultra-depleted orogenic peridotites. *Geochimica et Cosmochimica*
926 *Acta*, **86**, 354-366.
- 927 Krouse H. R. and Thode H. G. (1962). Thermodynamic properties and geochemistry of isotopic compounds of
928 selenium. *Canadian Journal of Chemistry*, **40**(2), 367-375.
- 929 Kurzawa T., König S., Labidi J., Yierpan A. and Schoenberg R. (2017). A method for Se isotope analysis of low ng-
930 level geological samples via double spike and hydride generation MC-ICP-MS. *Chemical Geology*, **466**, 219-228.
- 931 Labidi J., Cartigny P., Hamelin C., Moreira M. and Dosso L. (2014). Sulfur isotope budget (³²S, ³³S, ³⁴S and ³⁶S) in
932 Pacific–Antarctic ridge basalts: A record of mantle source heterogeneity and hydrothermal sulfide assimilation.
933 *Geochimica et Cosmochimica Acta*, **133**, 47-67.
- 934 Labidi J. and Cartigny P. (2016). Negligible sulfur isotope fractionation during partial melting: Evidence from Garrett
935 transform fault basalts, implications for the late-veener and the hadean matte. *Earth and Planetary Science Letters*,
936 **451**, 196-207.
- 937 Labidi J., Cartigny P. and Moreira M. (2013). Non-chondritic sulphur isotope composition of the terrestrial mantle.
938 *Nature*, **501**(7466), 208-11.
- 939 Labidi J., König S., Kurzawa T., Yierpan A. and Schoenberg R. (2018). The selenium isotopic variations in chondrites
940 are mass-dependent; Implications for sulfide formation in the early solar system. *Earth and Planetary Science*
941 *Letters*, **481**, 212-222.
- 942 Labidi J., Shahar A., Le Losq C., Hillgren V. J., Mysen B. O. and Farquhar J. (2016). Experimentally determined
943 sulfur isotope fractionation between metal and silicate and implications for planetary differentiation. *Geochimica*
944 *et Cosmochimica Acta*, **175**, 181-194.
- 945 Langmuir C. H., Klein E. M. and Plank T. (1992). Petrological Systematics of Mid-Ocean Ridge Basalts: Constraints
946 on Melt Generation Beneath Ocean Ridges. In: Morgan J. P., Blackman D. K., and Sinton J. M. (Eds.), *Mantle*
947 *Flow and Melt Generation at Mid-Ocean Ridges*, *Geophysical Monograph Series*. American Geophysical Union,
948 Washington, D. C., 183-280.
- 949 Layton-Matthews D., Peter J. M., Scott S. D., Leybourne M. I. (2008). Distribution, mineralogy, and geochemistry of
950 selenium in felsic volcanic-hosted massive sulfide deposits of the Finlayson Lake district, Yukon Territory, Canada.
951 *Economic Geology*, **103**(1), 61-88.
- 952 Layton-Matthews D., Leybourne M. I., Peter J. M., Scott S. D., Cousens B. and Eglington B. M. (2013). Multiple
953 sources of selenium in ancient seafloor hydrothermal systems: Compositional and Se, S, and Pb isotopic evidence
954 from volcanic-hosted and volcanic-sediment-hosted massive sulfide deposits of the Finlayson Lake District,
955 Yukon, Canada. *Geochimica et Cosmochimica Acta*, **117**, 313-331.
- 956 Le Roux V., Bodinier J. L., Tommasi A., Alard O., Dautri, J. M., Vauchez A., Riches A.J.V. (2007). The Lherz spinel
957 lherzolite: refertilised rather than pristine mantle. *Earth and Planetary Science Letters*, **259**, 599-612.

- 958 Lee C. T. A., Luffi P., Plank T., Dalton H. and Leeman W. P. (2009). Constraints on the depths and temperatures of
959 basaltic magma generation on Earth and other terrestrial planets using new thermobarometers for mafic magmas.
960 *Earth and Planetary Science Letters*, **279**(1-2), 20-33.
- 961 Lee C. T., Luffi P., Chin E. J., Bouchet R., Dasgupta R., Morton D. M., Le Roux V., Yin Q. Z. and Jin D. (2012).
962 Copper systematics in arc magmas and implications for crust-mantle differentiation. *Science*, **336**(6077), 64-8.
- 963 Lee D. S. and Edmond J. M. (1985). Tellurium Species in Seawater. *Nature*, **313**(6005), 782-785.
- 964 Li Y. and Audétat A. (2012). Partitioning of V, Mn, Co, Ni, Cu, Zn, As, Mo, Ag, Sn, Sb, W, Au, Pb, and Bi between
965 sulfide phases and hydrous basanite melt at upper mantle conditions. *Earth and Planetary Science Letters*, **355**,
966 327-340.
- 967 Lissenberg C. J. and MacLeod C. J. (2016). A Reactive Porous Flow Control on Mid-ocean Ridge Magmatic Evolution.
968 *Journal of Petrology*, **57**(11-12), 2195-2220.
- 969 Lissner M., König S., Luguët A., le Roux P. J., Schuth S., Heuser A. and le Roex A. P. (2014). Selenium and tellurium
970 systematics in MORBs from the southern Mid-Atlantic Ridge (47–50°S). *Geochimica et Cosmochimica Acta*, **144**,
971 379-402.
- 972 Liu Y. and Brenan J. (2015). Partitioning of platinum-group elements (PGE) and chalcogens (Se, Te, As, Sb, Bi)
973 between monosulfide-solid solution (MSS), intermediate solid solution (ISS) and sulfide liquid at controlled fO_2 –
974 fS_2 conditions. *Geochimica et Cosmochimica Acta*, **159**, 139-161.
- 975 Lodders K., Palme H. and Gail H. P. (2009). Abundances of the elements in the solar system. In: Trumper J. E. (Ed.),
976 *Landolt-Bornstein, New Series*, Berlin, Heidelberg, New York: Springer-Verlag, 560-630.
- 977 Lonsdale P. (1994). Geomorphology and structural segmentation of the crest of the southern (Pacific-Antarctic) East
978 Pacific Rise. *Journal of Geophysical Research: Solid Earth*, **99**(B3), 4683-4702.
- 979 Lorand J. P. (1991). Sulphide Petrology and Sulphur Geochemistry of Orogenic Lherzolites: A Comparative Study of
980 the Pyrenean Bodies (France) and the Lanzo Massif (Italy). *Journal of Petrology*, Special Volume(2), 77-95.
- 981 Lorand J. P. and Alard O. (2010). Determination of selenium and tellurium concentrations in Pyrenean peridotites
982 (Ariege, France): New insight into S/Se/Te systematics of the upper in mantle samples. *Chemical Geology*, **278**(1-
983 2), 120-130.
- 984 Lorand J. P. and Luguët A. (2016). Chalcophile and Siderophile Elements in Mantle Rocks: Trace Elements Controlled
985 By Trace Minerals. *Reviews in Mineralogy and Geochemistry*, **81**(1), 441-488.
- 986 Lorand J. P., Alard O., Luguët A. and Keays R. R. (2003). Sulfur and selenium systematics of the subcontinental
987 lithospheric mantle: Inferences from the Massif Central xenolith suite (France). *Geochimica et Cosmochimica*
988 *Acta*, **67**(21), 4137-4151.
- 989 Lorand J. P., Delpech G., Gregoire M., Moine B., O'Reilly S. Y. and Cottin J. Y. (2004). Platinum-group elements
990 and the multistage metasomatic history of Kerguelen lithospheric mantle (South Indian Ocean). *Chemical Geology*,
991 **208**(1-4), 195-215.
- 992 Lorand J. P., Alard O. and Luguët A. (2010). Platinum-group element micronuggets and refertilization process in
993 Lherz orogenic peridotite (northeastern Pyrenees, France). *Earth and Planetary Science Letters*, **289**(1-2), 298-
994 310.
- 995 Lorand J. P., Luguët A. and Alard O. (2013). Platinum-group element systematics and petrogenetic processing of the
996 continental upper mantle: A review. *Lithos*, **164**, 2-21.
- 997 Luais B. (2012). Germanium chemistry and MC-ICPMS isotopic measurements of Fe–Ni, Zn alloys and silicate
998 matrices: Insights into deep Earth processes. *Chemical Geology*, **334**, 295-311.
- 999 Luguët A. and Reisberg L. (2016). Highly Siderophile Element and ^{187}Os Signatures in Non-cratonic Basalt-hosted
1000 Peridotite Xenoliths: Unravelling the Origin and Evolution of the Post-Archean Lithospheric Mantle. *Reviews in*
1001 *Mineralogy and Geochemistry*, **81**(1), 305-367.
- 1002 Luguët A., Behrens M., Pearson D. G., König S. and Herwartz D. (2015). Significance of the whole rock Re–Os ages
1003 in cryptically and modally metasomatised cratonic peridotites: Constraints from HSE–Se–Te systematics.
1004 *Geochimica et Cosmochimica Acta*, **164**, 441-463.
- 1005 Luguët A., Lorand J. P. and Seyler M. (2003). Sulfide petrology and highly siderophile element geochemistry of
1006 abyssal peridotites: A coupled study of samples from the Kane Fracture Zone (45°W 23°20N, MARK Area,
1007 Atlantic Ocean). *Geochimica et Cosmochimica Acta*, **67**(8), 1553-1570.
- 1008 Luguët A., Lorand J. P., Alard O. and Cottin J. Y. (2004). A multi-technique study of platinum group element
1009 systematic in some Ligurian ophiolitic peridotites, Italy. *Chemical Geology*, **208**(1-4), 175-194.

- 1010 Luguët A., Shirey S. B., Lorand J. P., Horan M. F. and Carlson R. W. (2007). Residual platinum-group minerals from
1011 highly depleted harzburgites of the Lherz massif (France) and their role in HSE fractionation of the mantle.
1012 *Geochimica et Cosmochimica Acta*, **71**(12), 3082-3097.
- 1013 Mathez E. A. (1976). Sulfur solubility and magmatic sulfides in submarine basalt glass. *Journal of Geophysical*
1014 *Research*, **81**(23), 4269-4276.
- 1015 McDonough W. F. (2014). Compositional Model for the Earth's Core. In: Holland H. D., Turekian K. K. (Eds.),
1016 *Treatise on Geochemistry (Second Edition)*. Elsevier, Oxford, 559-577.
- 1017 McDonough W. F. and Sun S. S. (1995). The Composition of the Earth. *Chemical Geology*, **120**(3-4), 223-253.
- 1018 McPhail D. C. (1995). Thermodynamic Properties of Aqueous Tellurium Species between 25 and 350°C. *Geochimica*
1019 *et Cosmochimica Acta*, **59**(5), 851-866.
- 1020 Measures C. I. and Burton J. D. (1980). The Vertical-Distribution and Oxidation-States of Dissolved Selenium in the
1021 Northeast Atlantic-Ocean and Their Relationship to Biological Processes. *Earth and Planetary Science Letters*,
1022 **46**(3), 385-396.
- 1023 Meisel T., Walker R. J. and Morgan J. W. (1996). The osmium isotopic composition of the Earth's primitive upper
1024 mantle. *Nature*, **383**, 517-520.
- 1025 Menzies M., Blanchard D., Brannon J. and Korotev R. (1977). Rare-Earth Geochemistry of Fused Ophiolitic and
1026 Alpine Lherzolites. II. Beni Bouchera, Ronda and Lanzo. *Contributions to Mineralogy and Petrology*, **64**(1), 53-
1027 74.
- 1028 Michael P. J. and Cornell W. C. (1998). Influence of spreading rate and magma supply on crystallization and
1029 assimilation beneath mid-ocean ridges: Evidence from chlorine and major element chemistry of mid-ocean ridge
1030 basalts. *Journal of Geophysical Research: Solid Earth*, **103**(B8), 18325-18356.
- 1031 Mitchell K., Couture R.-M., Johnson T. M., Mason P. R. D., Cappellen P. V. (2013). Selenium sorption and isotope
1032 fractionation: Iron(III) oxides versus iron(II) sulfides. *Chemical Geology*, **342**, 21-28.
- 1033 Moore J. G. and Fabbi B. P. (1971). An estimate of the juvenile sulfur content of basalt. *Contributions to Mineralogy*
1034 *and Petrology*, **33**(2), 118-127.
- 1035 Moore J. G. and Schillín J. G. (1973). Vesicles, Water, and Sulfur in Reykjanes Ridge Basalts. *Contributions to*
1036 *Mineralogy and Petrology*, **41**(2), 105-118.
- 1037 Moreira M. A., Dosso L. and Ondréas H. (2008). Helium isotopes on the Pacific-Antarctic ridge (52.5°–41.5°S).
1038 *Geophysical Research Letters*, **35**(10).
- 1039 Morgan J. W. (1986). Ultramafic xenoliths: Clues to Earth's late accretionary history. *Journal of Geophysical*
1040 *Research*, **91**(B12), 12375-12387.
- 1041 Mungall J. E. and Brenan J. M. (2014). Partitioning of platinum-group elements and Au between sulfide liquid and
1042 basalt and the origins of mantle-crust fractionation of the chalcophile elements. *Geochimica et Cosmochimica Acta*,
1043 **125**, 265-289.
- 1044 Nagamori M. and Mackey P. J. (1977). Distribution equilibria of Sn, Se and Te between FeO-Fe₂O₃-SiO₂-Al₂O₃-
1045 CuO_{0.5} slag and metallic copper. *Metallurgical Transactions B*, **8**(1), 39-46.
- 1046 Nielsen R. L., Forsythe L. M., Gallahan W. E. and Fisk M. R. (1994). Major-Element and Trace-Element Magnetite-
1047 Melt Equilibria. *Chemical Geology*, **117**(1-4), 167-191.
- 1048 Nielsen S. G., Shimizu N., Lee C.-T. A. and Behn M. D. (2014). Chalcophile behavior of thallium during MORB
1049 melting and implications for the sulfur content of the mantle. *Geochemistry, Geophysics, Geosystems*, **15**, 4905-
1050 4919.
- 1051 Niu Y. and Batiza R. (1991). An empirical method for calculating melt compositions produced beneath mid-ocean
1052 ridges: Application for axis and off-axis (seamounts) melting. *Journal of Geophysical Research: Solid Earth*,
1053 **96**(B13), 21753-21777.
- 1054 Norris C. A. and Wood B. J. (2017). Earth's volatile contents established by melting and vaporization. *Nature*,
1055 **549**(7673), 507-510.
- 1056 Ondréas H., Aslanian D., Géli L., Olivet J.-L. and Briais A. (2001). Variations in axial morphology, segmentation,
1057 and seafloor roughness along the Pacific-Antarctic Ridge between 56°S and 66°S. *Journal of Geophysical*
1058 *Research: Solid Earth*, **106**(B5), 8521-8546.
- 1059 O'Neill H. S. and Jenner F. E. (2012). The global pattern of trace-element distributions in ocean floor basalts. *Nature*,
1060 **491**(7426), 698-704.
- 1061 Palme H. and O'Neill H. S. C. (2014). Cosmochemical estimates of Mantle Composition. In: Holland H. D. and

- 1062 Turekian K. K. (Eds.), *Treatise on Geochemistry (Second Edition)*. Elsevier, Oxford, 1-39.
- 1063 Patten C., Barnes S. J. and Mathez E. A. (2012). Textural Variations in MORB Sulfide Droplets Due to Differences
1064 in Crystallization History. *Canadian Mineralogist*, **50**(3), 675-692.
- 1065 Patten C., Barnes S. J., Mathez E. A. and Jenner F. E. (2013). Partition coefficients of chalcophile elements between
1066 sulfide and silicate melts and the early crystallization history of sulfide liquid: LA-ICP-MS analysis of MORB
1067 sulfide droplets. *Chemical Geology*, **358**, 170-188.
- 1068 Patten C. G. C., Pitcairn I. K., Teagle D. A. H. and Harris M. (2016). Sulphide mineral evolution and metal mobility
1069 during alteration of the oceanic crust: Insights from ODP Hole 1256D. *Geochimica et Cosmochimica Acta*, **193**,
1070 132-159.
- 1071 Peach C. L., Mathez E. A. and Keays R. R. (1990). Sulfide melt-silicate melt distribution coefficients for noble metals
1072 and other chalcophile elements as deduced from MORB: Implications for partial melting. *Geochimica et*
1073 *Cosmochimica Acta*, **54**(12), 3379-3389.
- 1074 Plank T., Spiegelman M., Langmuir C. H. and Forsyth D. W. (1995). The meaning of “mean F”: Clarifying the mean
1075 extent of melting at ocean ridges. *Journal of Geophysical Research*, **100**(B8), 15045-15052.
- 1076 Pogge von Strandmann P. A. E., Coath C. D., Catling D. C., Poulton S. W. and Elliott T. (2014). Analysis of mass
1077 dependent and mass independent selenium isotope variability in black shales. *Journal of Analytical Atomic*
1078 *Spectrometry*, **29**(9), 1648-1659.
- 1079 Rashid K. and Krouse H. R. (1985). Selenium isotopic fractionation during SeO_3^{2-} reduction to Se^0 and H_2Se .
1080 *Canadian Journal of Chemistry*, **63**(11), 3195-3199. <https://doi.org/10.1139/v85-528>
- 1081 Rees C. E. and Thode H. G. (1966). Selenium isotope effects in the reduction of sodium selenite and of sodium selenate.
1082 *Canadian Journal of Chemistry*, **44**(4), 419-427.
- 1083 Rehkämper M., Halliday A. N., Fitton J. G., Lee D. C., Wieneke M. and Arndt N. T. (1999). Ir, Ru, Pt, and Pd in
1084 basalts and komatiites: New constraints for the geochemical behavior of the platinum-group elements in the mantle.
1085 *Geochimica et Cosmochimica Acta*, **63**(22), 3915-3934.
- 1086 Righter K., Leeman W. P. and Hervig R. L. (2006). Partitioning of Ni, Co and V between spinel-structured oxides and
1087 silicate melts: Importance of spinel composition. *Chemical Geology*, **227**(1-2), 1-25.
- 1088 Rose-Weston L., Brenan J. M., Fei Y. W., Secco R. A. and Frost D. J. (2009). Effect of pressure, temperature, and
1089 oxygen fugacity on the metal-silicate partitioning of Te, Se, and S: Implications for earth differentiation.
1090 *Geochimica et Cosmochimica Acta*, **73**(15), 4598-4615.
- 1091 Rouxel O., Fouquet Y. and Ludden J. N. (2004). Subsurface processes at the Lucky Strike hydrothermal field, Mid-
1092 Atlantic Ridge: Evidence from sulfur, selenium, and iron isotopes. *Geochimica et Cosmochimica Acta*, **68**(10),
1093 2295-2311.
- 1094 Rouxel O., Ludden J., Carignan J., Marin L. and Fouquet Y. (2002). Natural variations of Se isotopic composition
1095 determined by hydride generation multiple collector inductively coupled plasma mass spectrometry. *Geochimica*
1096 *et Cosmochimica Acta*, **66**(18), 3191-3199.
- 1097 Saal A. E., Hauri E. H., Langmuir C. H. and Perfit M. R. (2002). Vapour undersaturation in primitive mid-ocean-ridge
1098 basalt and the volatile content of Earth's upper mantle. *Nature*, **419**, 451.
- 1099 Salters V. J. M. and Stracke A. (2004). Composition of the depleted mantle. *Geochemistry, Geophysics, Geosystems*,
1100 **5**, Q05B07.
- 1101 Schaefer L. and Fegley B. (2010). Volatile element chemistry during metamorphism of ordinary chondritic material
1102 and some of its implications for the composition of asteroids. *Icarus*, **205**(2), 483-496.
- 1103 Shimizu K., Saal A. E., Myers C. E., Nagle A. N., Hauri E. H., Forsyth D. W., Kamenetsky V. S. and Niu Y. L. (2016).
1104 Two-component mantle melting-mixing model for the generation of mid-ocean ridge basalts: Implications for the
1105 volatile content of the Pacific upper mantle. *Geochimica et Cosmochimica Acta*, **176**, 44-80.
- 1106 Siebert J., Badro J., Antonangeli D. and Ryerson F. J. (2013). Terrestrial accretion under oxidizing conditions. *Science*,
1107 **339**(6124), 1194-1197.
- 1108 Smith P. M. and Asimow P. D. (2005). Adiaabat_1ph: A new public front-end to the MELTS, pMELTS, and pHMELTS
1109 models. *Geochemistry, Geophysics, Geosystems*, **6**, Q02004.
- 1110 Smythe D. J., Wood B. J. and Kiseeva E. S. (2017). The S content of silicate melts at sulfide saturation: New
1111 experiments and a model incorporating the effects of sulfide composition. *American Mineralogist*, **102**(4), 795-
1112 803.
- 1113 Steenstra E. S., Lin Y., Dankers D., Rai N., Berndt J., Matveev S. and van Westrenen W. (2017). The lunar core can

- 1114 be a major reservoir for volatile elements S, Se, Te and Sb. *Scientific Reports*, **7**(1),14552.
- 1115 Stüeken E. E., Foriel J., Nelson B. K., Buick R. and Catling D. C. (2013). Selenium isotope analysis of organic-rich
1116 shales: advances in sample preparation and isobaric interference correction. *Journal of Analytical Atomic*
1117 *Spectrometry*, **28**(11), 1734-1749.
- 1118 Suer T.-A., Siebert J., Remusat L., Menguy N. and Fiquet G. (2017). A sulfur-poor terrestrial core inferred from
1119 metal-silicate partitioning experiments. *Earth and Planetary Science Letters*, **469**, 84-97.
- 1120 Toplis M. J. and Corgne A. (2002). An experimental study of element partitioning between magnetite, clinopyroxene
1121 and iron-bearing silicate liquids with particular emphasis on vanadium. *Contributions to Mineralogy and Petrology*,
1122 **144**(1), 22-37.
- 1123 Vlastélic I., Aslanian D., Dosso L., Bougault H., Olivet J. L. and Geli L. (1999). Large-scale chemical and thermal
1124 division of the Pacific mantle. *Nature*, **399**(6734), 345-350.
- 1125 Vlastélic I., Dosso L., Bougault H., Aslanian D., Géli L., Etoubleau J., Bohn M., Joron J.-L. and Bollinger C. (2000).
1126 Chemical systematics of an intermediate spreading ridge: The Pacific-Antarctic Ridge between 56°S and 66°S.
1127 *Journal of Geophysical Research*, **105**(B2), 2915-2936.
- 1128 Vollstaedt H., Mezger K. and Leya I. (2016). The isotope composition of selenium in chondrites constrains the
1129 depletion mechanism of volatile elements in solar system materials. *Earth and Planetary Science Letters*, **450**,
1130 372-380.
- 1131 Wallace P. J. and Edmonds M. (2011). The Sulfur Budget in Magmas: Evidence from Melt Inclusions, Submarine
1132 Glasses, and Volcanic Gas Emissions. *Sulfur in Magmas and Melts: Its Importance for Natural and Technical*
1133 *Processes*, **73**(1), 215-246.
- 1134 Wang Z. and Becker H. (2013). Ratios of S, Se and Te in the silicate Earth require a volatile-rich late veneer. *Nature*,
1135 **499**(7458), 328-31.
- 1136 Wang Z., Becker H. and Gawronski T. (2013). Partial re-equilibration of highly siderophile elements and the
1137 chalcogens in the mantle: A case study on the Baldissero and Balmuccia peridotite massifs (Ivrea Zone, Italian
1138 Alps). *Geochimica et Cosmochimica Acta*, **108**, 21-44.
- 1139 Wang Z. and Becker H. (2015a). Fractionation of highly siderophile and chalcogen elements during magma transport
1140 in the mantle: Constraints from pyroxenites of the Balmuccia peridotite massif. *Geochimica et Cosmochimica Acta*,
1141 **159**, 244-263.
- 1142 Wang Z. and Becker H. (2015b). Abundances of Ag and Cu in mantle peridotites and the implications for the behavior
1143 of chalcophile elements in the mantle. *Geochimica et Cosmochimica Acta*, **160**, 209-226.
- 1144 Wang Z., Becker H. and Wombacher F. (2015). Mass Fractions of S, Cu, Se, Mo, Ag, Cd, In, Te, Ba, Sm, W, Tl and
1145 Bi in Geological Reference Materials and Selected Carbonaceous Chondrites Determined by Isotope Dilution ICP-
1146 MS. *Geostandards and Geoanalytical Research*, **39**(2), 185-208.
- 1147 Wasson J. T. and Kallemeyn G. W. (1988). Compositions of Chondrites. *Philosophical Transactions of the Royal*
1148 *Society A: Mathematical, Physical and Engineering Sciences*, **325**(1587), 535-544.
- 1149 Watts A. B., Weissel J. K., Duncan R. A. and Larson R. L. (1988). Origin of the Louisville Ridge and its relationship
1150 to the Eltanin Fracture Zone System. *Journal of Geophysical Research*, **93**(B4), 3051-3077.
- 1151 Workman R. K. and Hart S. R. (2005). Major and trace element composition of the depleted MORB mantle (DMM).
1152 *Earth and Planetary Science Letters*, **231**(1-2), 53-72.
- 1153 Wykes J. L., O'Neill H. S. C. & Mavrogenes, J. A. (2011). XANES investigation of selenium speciation in silicate
1154 glasses. Paper presented at Annual V. M. Goldschmidt Conference, Prague, Czech Republic.
- 1155 Wykes J. L., O'Neill H. S. C. and Mavrogenes J. A. (2015). The Effect of FeO on the Sulfur Content at Sulfide
1156 Saturation (SCSS) and the Selenium Content at Selenide Saturation of Silicate Melts. *Journal of Petrology*, **56**(7),
1157 1407-1424.
- 1158 Yamamoto M. (1976). Relationship between Se/S and Sulfur Isotope Ratios of Hydrothermal Sulfide Minerals.
1159 *Mineralium Deposita*, **11**(2), 197-209.
- 1160 Yang A. Y., Zhou M. F., Zhao T. P., Deng X. G., Qi L. and Xu J. F. (2014). Chalcophile elemental compositions of
1161 MORBs from the ultraslow-spreading Southwest Indian Ridge and controls of lithospheric structure on S-saturated
1162 differentiation. *Chemical Geology*, **382**, 1-13.
- 1163 Yi W., Halliday A. N., Alt J. C., Lee D.-C., Rehkämper M., Garcia M. O., Langmuir C. H. and Su Y. (2000). Cadmium,
1164 indium, tin, tellurium, and sulfur in oceanic basalts: Implications for chalcophile element fractionation in the Earth.
1165 *Journal of Geophysical Research*, **105**(B8), 18927.

- 1166 Yierpan A., König S., Labidi J., Kurzawa T., Babechuk M. G. and Schoenberg R. (2018). Chemical Sample Processing
 1167 for Combined Selenium Isotope and Selenium-Tellurium Elemental Investigation of the Earth's Igneous
 1168 Reservoirs. *Geochemistry, Geophysics, Geosystems*, **19**, 516-533.
- 1169 Young E. D., Manning C. E., Schauble E. A., Shahar A., Macris C. A., Lazar C. and Jordan M. (2015). High-
 1170 temperature equilibrium isotope fractionation of non-traditional stable isotopes: Experiments, theory, and
 1171 applications. *Chemical Geology*, **395**, 176-195.
- 1172 Zhang H. L., Cottrell E., Solheid P. A., Kelley K. A. and Hirschmann M. M. (2018). Determination of Fe³⁺ /ΣFe of
 1173 XANES basaltic glass standards by Mössbauer spectroscopy and its application to the oxidation state of iron in
 1174 MORB. *Chemical Geology*, **497**, 166-175.
- 1175 Zhang Z. and Hirschmann M. M. (2016). Experimental constraints on mantle sulfide melting up to 8 GPa. *American
 1176 Mineralogist*, **101**(1-2), 181-192.
- 1177 Zhang Z., von der Handt A. and Hirschmann M. M. (2018). An experimental study of Fe–Ni exchange between sulfide
 1178 melt and olivine at upper mantle conditions: implications for mantle sulfide compositions and phase equilibria.
 1179 *Contributions to Mineralogy and Petrology*, **173**(3), 19.
- 1180 Zhu J.-M., Johnson T. M., Clark S. K. and Zhu X.-K. (2008). High Precision Measurement of Selenium Isotopic
 1181 Composition by Hydride Generation Multiple Collector Inductively Coupled Plasma Mass Spectrometry with a
 1182 ⁷⁴Se-⁷⁷Se Double Spike. *Chinese Journal of Analytical Chemistry*, **36**(10), 1385-1390.

1183

1184 Captions for Tables and Figures

1185 **Table 1.** Selenium isotope composition and Se–Te abundances of geological reference materials and a randomly
 1186 selected PAR MORB glass reported in this study and literature.

1187 **Table 2.** Selenium isotope composition, S–Se–Te abundances, and selected major element composition of the
 1188 studied PAR glasses.

1189 **Table 3.** Summary of model parameters used for the near-fractional melting of a MORB mantle.

1190 **Fig. 1.** Measurements of geological reference materials and a randomly selected moderately evolved PAR glass
 1191 (PAC2 DR33-1; 6.63 wt.% MgO; Table 1) for assessing the external reproducibility (2 s.d.) on the sample
 1192 δ^{82/76}Se (left panel). Each symbol represents an individual measurement with the associated internal precision
 1193 (2 s.e.; over 40 cycles). All sample digests were analyzed once, except for two MORB glass digestions that were
 1194 aliquoted and analyzed twice. Our analytical accuracy and precision is evaluated by the long-term reproducibility
 1195 of inter-laboratory standard MH-495 (open circles; right panel), which yields $-3.26 \pm 0.12\%$ and $-3.25 \pm 0.07\%$
 1196 (2 s.d.) for 15 and 30 ng mL⁻¹ solutions, respectively (Supplementary Table S1; this study; Kurzawa et al., 2017;
 1197 Yierpan et al., 2018). Shown for comparison are literature data on reference materials reported by Kurzawa et
 1198 al. (2017), Yierpan et al. (2018) (measurements in both studies were performed over the course of ~18 months
 1199 at the University of Tübingen; all circles), and Rouxel et al. (2002) (diamonds). Interlaboratory comparison of
 1200 δ^{82/76}Se data on silicate samples remains difficult due to the limited Se isotope studies, and therefore BHVO-2
 1201 and BCR-2 are compared here with BHVO-1 and BCR-1 (only BE-N has been analyzed by two working groups).
 1202 δ^{82/76}Se from Rouxel et al. (2002) that were originally reported relative to MERCK standard are converted
 1203 relative to NIST SRM 3149 following Carignan and Wen (2007) considering error propagation (analytical and
 1204 conversion errors of 0.25‰ and 0.20‰, respectively).

1205 **Fig. 2.** Variation of Se isotope composition of PAR glasses with (a) sample latitude, (b) dredging depth, and (c)
1206 Se abundance. Two ridge sections (north of the Vacquier FZ and south of the Udintsev FZ) display identical
1207 average $\delta^{82/76}\text{Se}$ values within uncertainty (a).

1208 **Fig. 3.** Compilation of Se isotope compositions of PAR MORBs, terrestrial rock standards (7 basalts and
1209 1 peridotite; Rouxel et al., 2002; Kurzawa et al., 2017; Yierpan et al., 2018; this study), basalts from a lava lake
1210 near the Lucky Strike hydrothermal field (n = 2; Rouxel et al., 2004), and main chondrite classes (Vollstaedt et
1211 al., 2016; Labidi et al., 2018). See Fig. 1 and Yierpan et al. (2018) for details on the measured basaltic rock
1212 standards. The peridotite analyzed by Rouxel et al. (2002) is a partially serpentized harzburgite (PCC-1; Jain
1213 et al., 2000). Each shaded field represents the average $\delta^{82/76}\text{Se}$ (black dashed line) with 2 s.d. uncertainties of
1214 chondrite and terrestrial rocks. Red dashed line denotes $\delta^{82/76}\text{Se} = 0\text{‰}$. The overall chondrite average $\delta^{82/76}\text{Se}$
1215 from Labidi et al. (2018) includes all chondrite groups analyzed (enstatite, ordinary, and carbonaceous) except
1216 three weathered CV chondrites. The data from Rouxel et al. (2002, 2004) is converted relative to NIST SRM
1217 3149 following the approach of Carignan and Wen (2007) while considering error propagation (analytical and
1218 conversion uncertainties); the light and dark grey fields represent the uncertainties of the mean with (0.32‰)
1219 and without (0.17‰) error propagation, respectively.

1220 **Fig. 4.** Variations of Se, Te, S, and Cu abundances and/or their ratios with MgO content. Also shown for
1221 comparison are SMAR N- and E-MORBs (Lissner et al., 2014; E-MORB refers to all enriched- and transitional-
1222 type MORBs), as well as global MORBs from Hertogen et al. (1980) and Yi et al. (2000). The SMAR E-MORBs
1223 display distinctly lower Se/Te and S/Te ratios than that of N-MORBs from both PAR and SMAR over almost
1224 the entire magmatic differentiation (c and e), reflecting the Te-enrichment in E-MORB mantle source (Lissner
1225 et al., 2014). The Cu/Se ratio (f) in PAR and SMAR remains fairly constant and remarkably similar prior to ~7–
1226 7.5 wt.% MgO and PAR samples show a smooth decrease afterwards. The change of relative compatibility of
1227 Cu–Se may be related to the FeO content of the silicate melt as noted by Brenan (2015). The vertical dashed
1228 lines represent the onset of magnetite saturation (5 wt.% MgO) and associated sulfide segregation. Prior to this,
1229 the observed apparent compatibilities of these chalcophile elements (Te>Cu>Se>S) in the PAR suite indicate
1230 that they are predominantly controlled by fractionation of sulfide liquid, consistent with previous studies. At
1231 magnetite saturation, except the most evolved sample (PAC2 DR27-1) whose S solubility remains largely
1232 unaffected (Labidi et al., 2014), other two samples show consistent decrease in Se (a) and increase in Te (b) from
1233 the general trend (note the consistent decreases in FeO_T and TiO_2 ; Supplementary Fig. S3). The strong abrupt
1234 decrease in their Se/Te and S/Te ratios (c and e) is argued here as an indicator of the predominant appearance of
1235 crystalline MSS in the segregating sulfide assemblage from the MORB melt (see the text for details).

1236 **Fig. 5.** Variations of $\delta^{34}\text{S}_{\text{V-CDT}}$ (a), $\delta^{82/76}\text{Se}$ (b) and S/Se ratios (c) with Cl/K that is used as a proxy for the extent
1237 of Cl contamination due to the interaction of the magma with brines and hydrothermally altered materials during
1238 magmatic differentiation (Michael and Cornell, 1998; Clog et al., 2013; Labidi et al., 2014). Note that Cl/K The
1239 grey shaded field represents the Cl/K ratio (0.01–0.08) of global MORBs that are unaffected by hydrothermal

1240 fluid assimilation (Michael and Cornell, 1998). The studied PAR basalts that have experienced high-T
1241 hydrothermal sulfide assimilation based on S isotope systematics (Labidi et al., 2014) are shown in red. Other
1242 PAR glass data (Labidi et al., 2014) are shown in grey circles (a). (d) shows the variation of $\delta^{82/76}\text{Se}$ with $\delta^{34}\text{S}_{\text{V-CDT}}$.
1243 Two shaded fields in (d) represent the average $\delta^{82/76}\text{Se}$ of two subsets of samples with and without
1244 assimilating hydrothermal sulfides.

1245 **Fig. 6.** Variations of S, Se, and Te abundances with MgO and/or FeO_T contents in PAR glasses. (a) shows the
1246 calculated SCSS (Smythe et al., 2017) for the primary melts ($n = 10$) as well as across the entire PAR magmatic
1247 differentiation following a similar approach of Ding and Dasgupta (2017). The primary melt major element
1248 compositions and their P–T conditions (on average ~ 10.2 kbar and 1325°C) of last equilibration with mantle
1249 olivine ($\text{Mg}\# = 0.90$) are calculated using the algorithm of Lee et al. (2009). At this condition, their SCSS are
1250 calculated in combination with a variety of equilibrium sulfide compositions ($X_{\text{Fe}} = 0.65\text{--}0.82$; $X_{\text{Fe}} = \text{Fe}/(\text{Fe} +$
1251 $\text{Ni} + \text{Cu})$ atomic ratio) that might be found in the shallow mantle. It shows that even the lowest SCSS value with
1252 $X_{\text{Fe}} = 0.63$ (calculated sulfide composition in equilibrium with the most primitive glass PAC1 DR12-1g
1253 following Kiseeva and Wood (2015)) is still higher than the observed S contents of primitive PAR MORBs,
1254 implying that primary melts may be sulfide-undersaturated. The modelled SCSS (Smythe et al., 2017) across the
1255 entire PAR magmatic differentiation (from ~ 11.8 wt.% MgO) is calculated at 3 kbar (also see Fig. 7 and
1256 Supplementary Fig. S3) with $X_{\text{Fe}} = 0.65$ using major element compositions from alphaMELTS. Also shown for
1257 comparison is the SCSS from COMAGMAT (Ariskin et al., 2013, 2018) for the observed magmatic
1258 differentiation using Ni contents of the silicate melts (other parameters from alphaMELTS; Supplementary Fig.
1259 S3). Both models are in good agreement with the observed S abundances in sulfide-saturated MORBs from the
1260 PAR and global oceanic spreading ridges (Jenner et al., 2012, 2015; Labidi et al., 2014; global MORB data from
1261 Jenner and O'Neill (2012); $n = 233$). (b) and (c) show the modelled Se–Te variations with the calculated $X_{\text{sulf}}^{\text{bulk min}}$
1262 (based on S systematics; Labidi et al., 2014) and the experimentally determined $D_{\text{Se or Te}}^{\text{sulf liq-sil}}$ for basaltic melts with
1263 8–11 wt.% FeO from Kiseeva et al. (2017), which well reproduces the observed Se–Te variations. Calculation
1264 assumes that Se–Te partitioning between the fractionated sulfide liquid and silicate melt is an intermediate
1265 equilibrium process between fractional and batch partitioning, with $S_b = 0.5$ (Rehkämper et al., 1999). The
1266 observed/empirical trends using the observed $D_{\text{Se or Te}}^{\text{bulk}}$ values with S_b of 0 and 1 were shown for comparison.
1267 Each tick mark represents 10% crystal fractionation step. Also shown in (b) and (c) are the primary PAR melt
1268 (~ 11.8 wt.% MgO) Se–Te contents corrected for sulfide + crystal fractionation during later differentiation (S-
1269 saturated; $\text{MgO} < 8.85$ wt.%) and for olivine fractionation during early differentiation (S-undersaturated; 11.8–
1270 8.85 wt.% MgO).

1271 **Fig. 7.** P–T diagram showing the sulfide phase relations determined on a single sulfide composition ($X_{\text{Fe}} = 0.74$,
1272 $\text{metal}/\text{S} = 0.93$, and $\text{Ni}/(\text{Fe} + \text{Ni}) = 0.25$ molar ratio; Bockrath et al., 2004; Zhang Z. and Hirschmann, 2016) and
1273 modelled conditions of PAR MORB differentiation (isobaric fractional crystallization; also see Supplementary

1274 Fig. S3) and near-fractional isentropic decompression melting path of a depleted MORB mantle (Salters and
1275 Stracke, 2004) to the base of the PAR crust (6.5 Km; alphaMELTS; Ghiorso and Sack, 1995; Ghiorso et al.,
1276 2002; Smith and Asimow, 2005). Each tick mark indicates 10% crystal fractionation or 2% melting extent.
1277 Anhydrous lherzolite solidus and bulk melt fraction (F_B) isopleths are calculated after Katz et al. (2003). The P–
1278 T condition of primary melt–mantle equilibration was obtained by the thermobarometer of Lee et al. (2009)
1279 using primitive PAR MORBs (>8.5 wt.% MgO; $n = 10$; Vlastelic et al., 2000; Hamelin et al., 2010), suggesting
1280 that melting at a mantle potential temperature (T_P) of 1350°C (also see Ding and Dasgupta (2017) for other
1281 MORBs) may be adequate for our modelling purpose because each data point for an aggregate primary melt
1282 represents weighted average P–T of melt extraction from all mantle parcels across the triangular melting zone
1283 and thus lies below the polybaric melting path (Asimow and Longhi, 2004; Lee et al., 2009). The primary melt
1284 P–T of MORBs from the Pacific ($n = 55$; Jenner and O’Neill, 2012) and other spreading-ridges ($n = 157$; PetDB)
1285 is shown for comparison. Both sulfide melting experiments (Bockrath et al., 2004; Zhang Z. and Hirschmann,
1286 2016) suggest that sulfide liquid is the dominant fractionating phase across much of low-P MORB differentiation
1287 (red arrow), consistent with previous inferences from behavior of chalcophile elements (see Section 5.2.1).
1288 However, the sulfide liquids estimated by these experiments distinctly vary at P–T conditions relevant to melting
1289 of a depleted mantle with typical T_P between $\sim 1275^\circ\text{C}$ and 1400°C . Under these conditions, a mantle sulfide
1290 may have similar metal/S ratio but much higher Ni/(Fe + Ni) (~ 0.40 – 0.65) compared to the sulfide mentioned
1291 above, resulting in an even lower solidus (Zhang Z. and Hirschmann, 2016; Zhang Z. et al., 2018). This implies
1292 that chalcophile element behavior during decompression melting is entirely controlled by sulfide liquid–silicate
1293 melt fractionation rather than MSS–sulfide liquid or MSS–silicate melt fractionation.

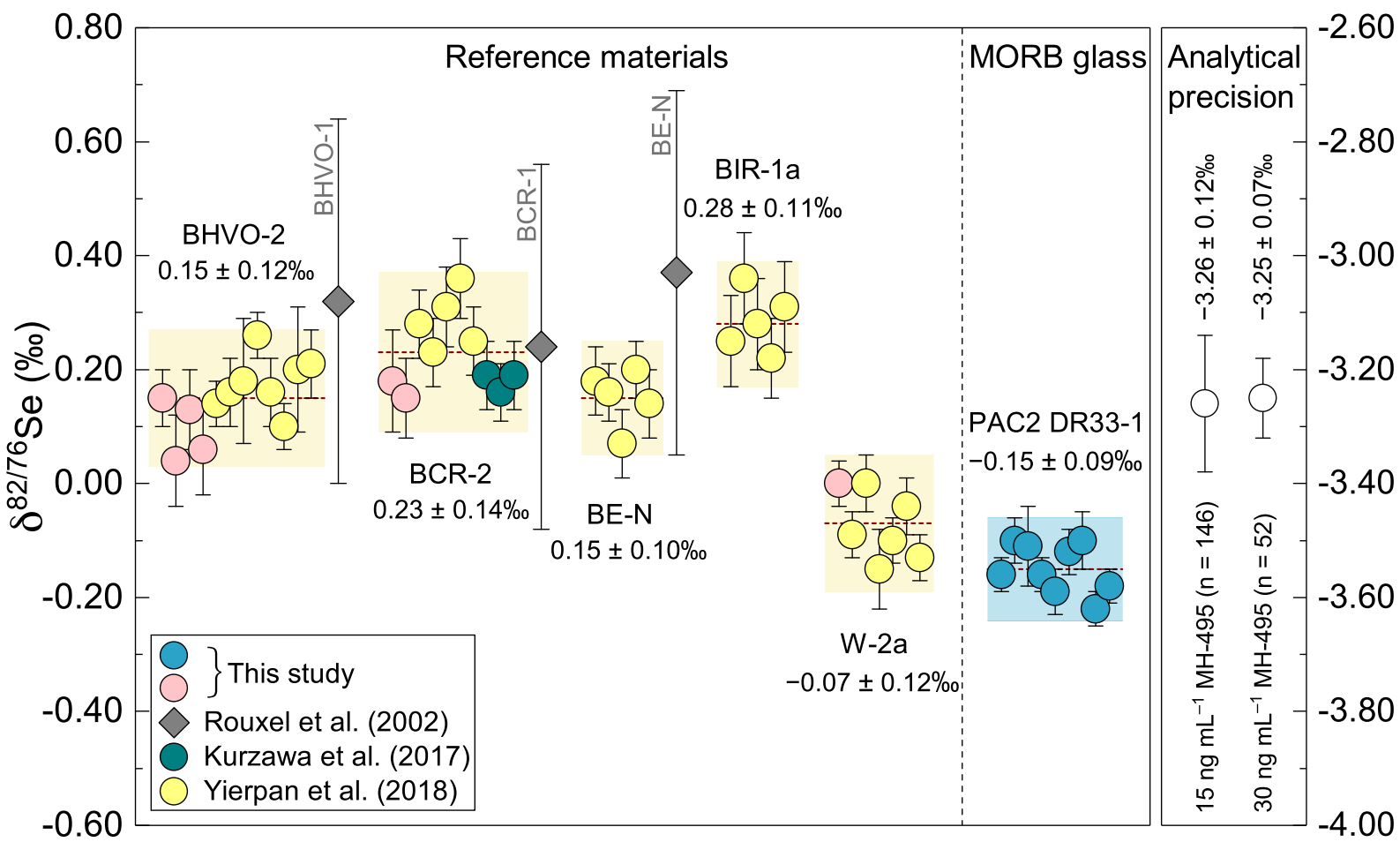
1294 **Fig. 8.** Variations of Se (a) and Te (b) contents and Se/Te ratios (c) of the primary PAR melts (also see Fig. 6b
1295 and c) with their average degree of melting (F_B) estimated by batch melting equation using incompatible trace
1296 element systematics (~ 6.6 – 11.7% ; Supplementary Fig. S4). The vertical and horizontal shaded field represent
1297 the range of F_B (6.5–9.5%) estimated from the forward modelling (near-fractional melting; pMELTS) and
1298 average primary melt composition (150 ± 8 and $3.1 \pm 0.4 \text{ ng g}^{-1}$ Se and Te, respectively; $\text{Se/Te} = 48.4 \pm 6.8$).
1299 The variation in Se–Te concentrations were modelled for a triangular near-fractional melting regime (e.g.,
1300 Rehkämper et al., 1999; Lissner et al., 2014; Brenan, 2015) using “fertile lherzolite-like” Se and Te contents (80
1301 and 11 ng g^{-1} ; Wang and Becker, 2013) and a range of S contents (150 – $200 \mu\text{g g}^{-1}$) previously estimated for the
1302 primitive and/or depleted upper mantle (e.g., Lugué et al., 2003; Lorand et al., 2013; Lorand and Lugué, 2016;
1303 Bézoz et al., 2005; Wang and Becker, 2013; Nielsen et al., 2014; Palme and O’Neill, 2014). $D_{\text{Se or Te}}^{\text{sulf liq-sil}}$ values are
1304 from Brenan (2015) and Kiseeva et al. (2017) (Table 3). The melt major element compositions and P–T
1305 conditions were modelled with pMELTS (see Fig. 7) and used to calculate $D_{\text{Se or Te}}^{\text{sulf liq-sil}}$ (as a function of FeO
1306 content of each equilibrium melt) and SCSS of the melt (Smythe et al., 2017) assuming the melt is in equilibrium
1307 with a calculated upper mantle sulfide ($\text{Fe}_{0.50}\text{Ni}_{0.36}\text{Cu}_{0.07}\text{S}_{1.00}$; Supplementary Fig. S5). (a), (b), and (c) show that
1308 the Se–Te systematics of the primary PAR melts can be broadly reproduced using the selected “fertile lherzolite-

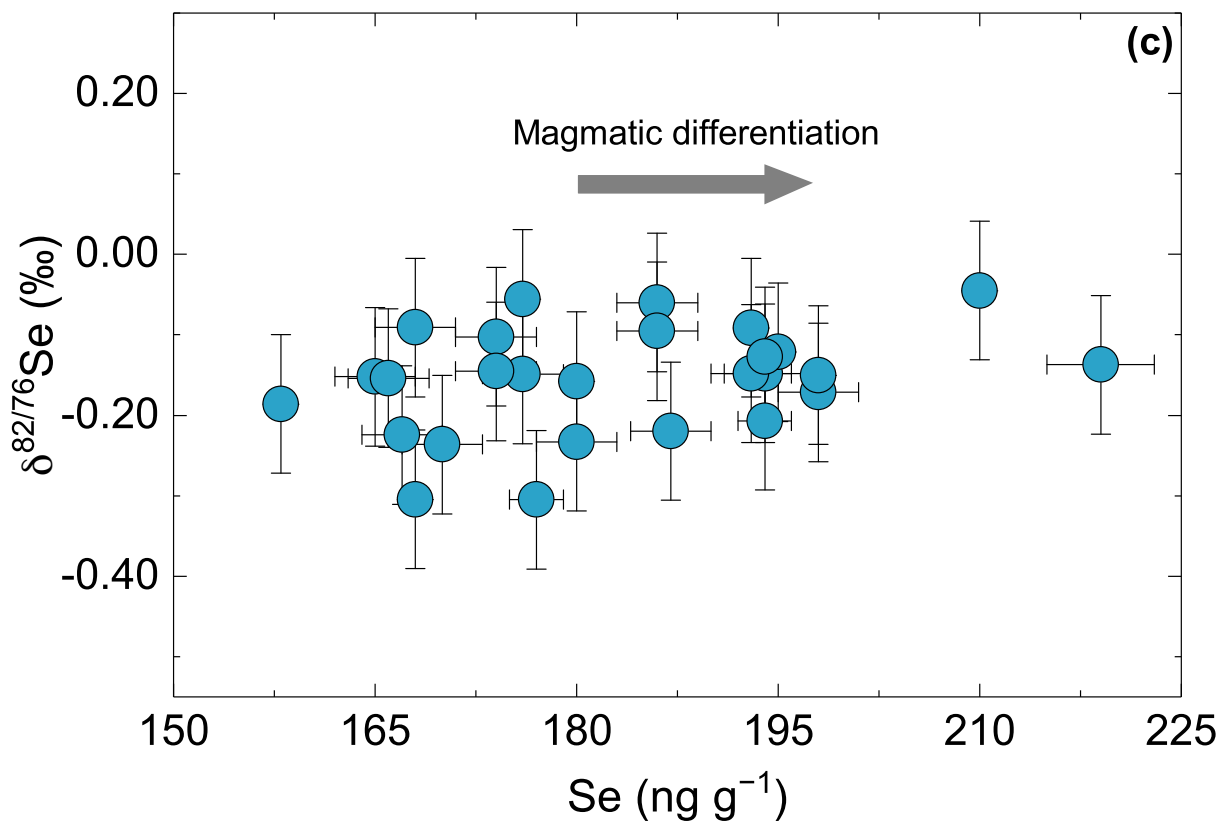
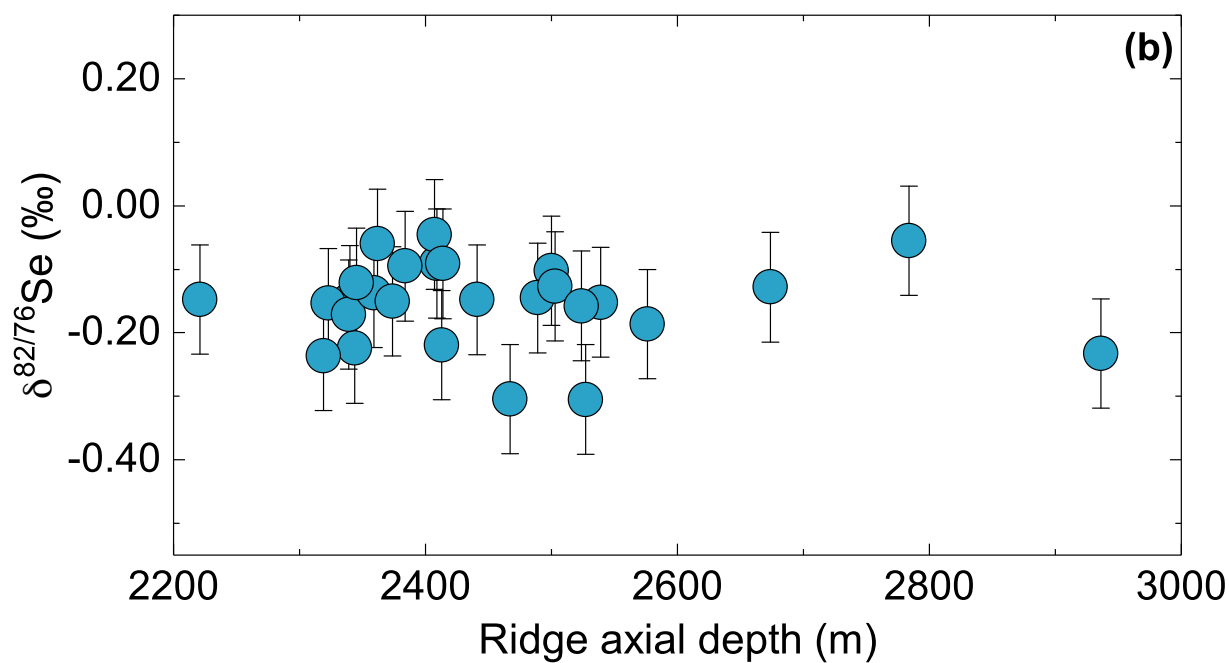
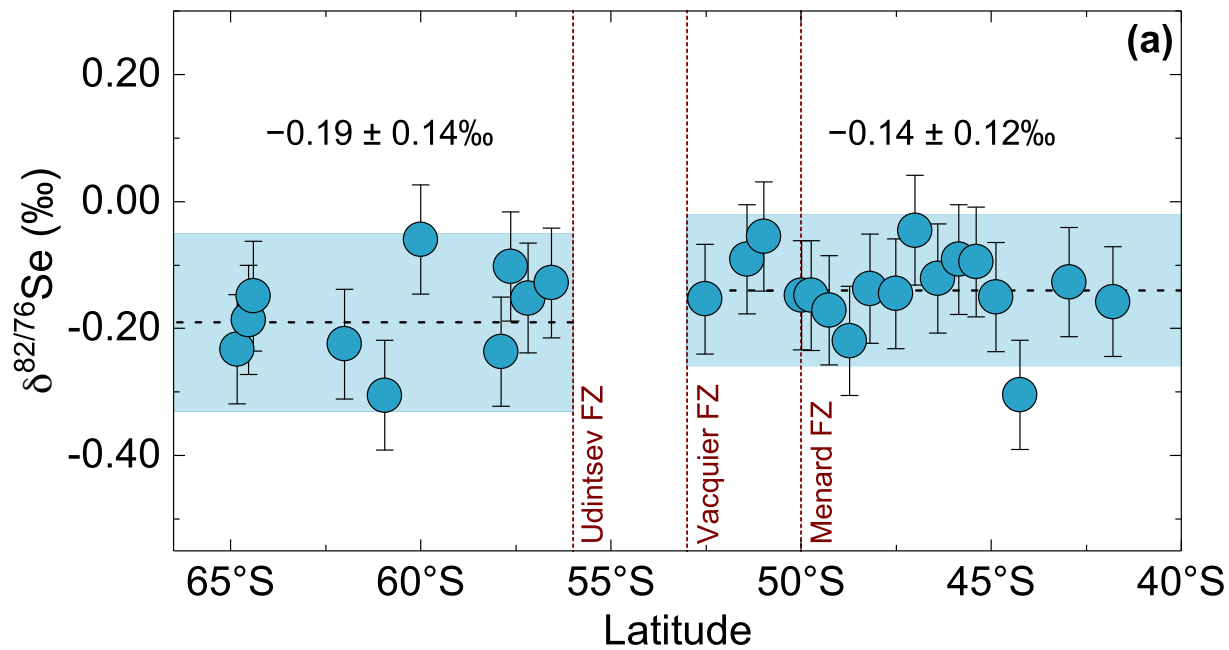
1309 like” Se–Te contents (with 170–200 $\mu\text{g g}^{-1}$ S) and $D_{\text{Se or Te}}^{\text{sulf liq-sil}}$ from Brenan (2015) (black lines). S-undersaturation
 1310 in the aggregate melt occurs at slightly different F_B (~9.5% to 11.5%) depending on the source S content (see
 1311 Supplementary Fig. S5a). With the same starting composition, calculation using $D_{\text{Se or Te}}^{\text{sulf liq-sil}}$ of Kiseeva et al. (2017)
 1312 overestimates the Se–Te contents of the melts (only shown for 180 $\mu\text{g g}^{-1}$ S in the source for simplicity; red
 1313 dashed lines) and only reproduces the observed variations with a significantly lowered source Se and Te contents
 1314 (48 and 3.5 ng g^{-1} , respectively; red solid lines).

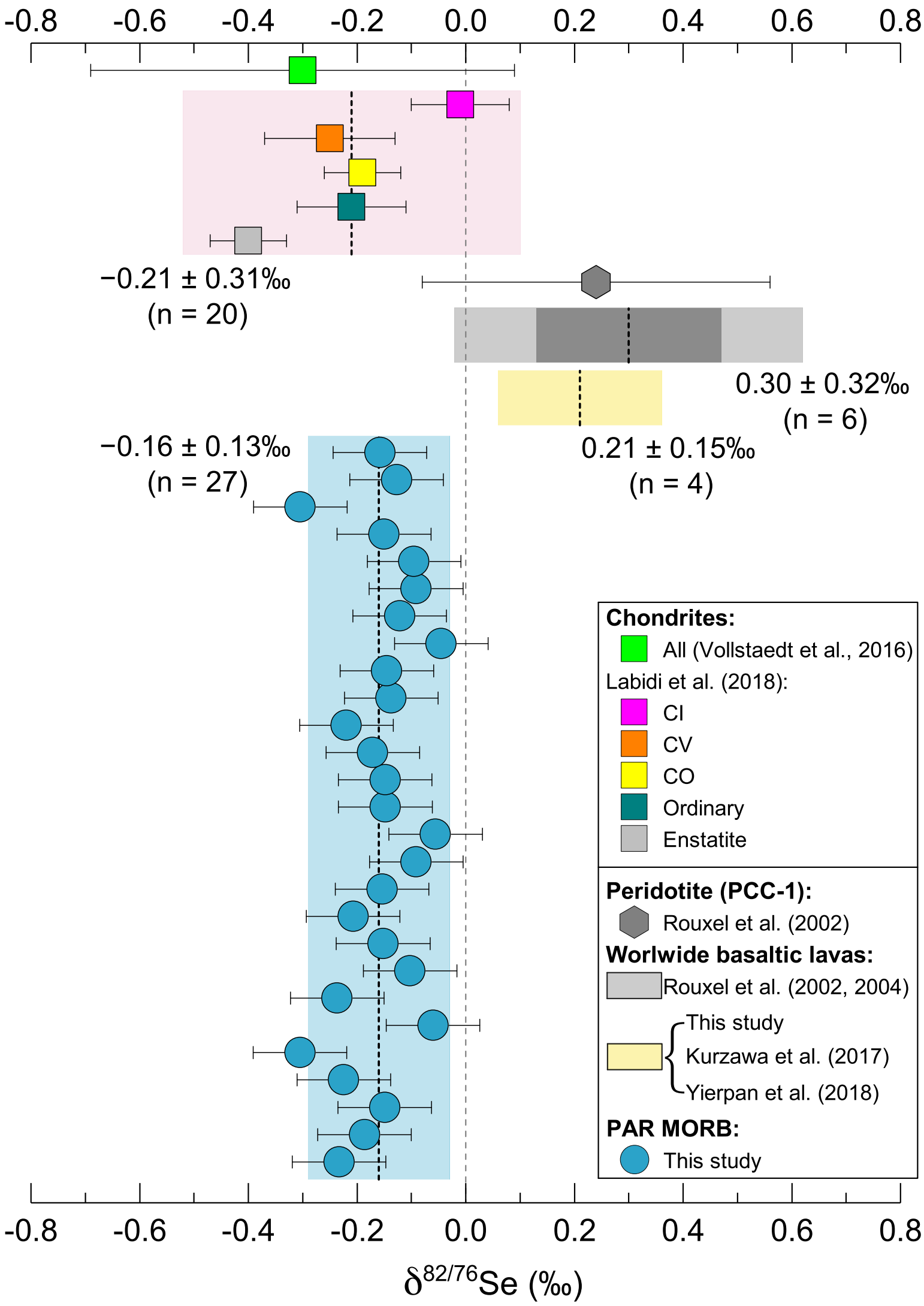
1315 **Fig. 9.** Variations of Se/Te against (a) Te contents of the primary aggregate melts and (b) Te and (c) Al_2O_3
 1316 contents of the mantle residue. The red solid lines and all black lines correspond to the modelled melt
 1317 composition with different proportions of sulfide liquid and crystalline MSS in the mantle having 180 $\mu\text{g g}^{-1}$ S
 1318 but two distinct Se and Te concentrations: (1) 80 ± 17 and 11 ± 1.7 ng g^{-1} , respectively (“fertile mantle”;
 1319 estimated at 3.52 wt.% Al_2O_3 ; Wang and Becker, 2013), in combination with $D_{\text{Se or Te}}^{\text{sulf liq-sil}}$ (changing as a function
 1320 of FeO contents of equilibrium melts) and/or $D_{\text{Se or Te}}^{\text{MSS-sil}}$ (constant) from Brenan (2015); and (2) 48 ± 8 and $3.5 \pm$
 1321 0.9 ng g^{-1} , respectively, which are the best-fit values from the modelling in combination with $D_{\text{Se or Te}}^{\text{sulf liq-sil}}$ (constant)
 1322 from Kiseeva et al. (2017) (see Fig. 8 and Supplementary Fig. S6 for the modelling of partial melt composition).
 1323 Each tick mark indicates 2% F_B (average degree of melting over a triangular melting zone) for the melts and 4%
 1324 melting for a residual melting column (only shown for curves with 100% sulfide liquid or MSS). The modelling
 1325 results are only shown until a mantle column becomes sulfide-exhausted, after which the remaining Se–Te
 1326 budget is controlled by platinum-groups minerals (PGM; see the light blue shaded area in (c); Luguet et al., 2007;
 1327 König et al., 2015). Additionally shown are the melting curves of a source with the maximum “fertile mantle”
 1328 Se and Te contents (101 and 12.5 ng g^{-1} , respectively; estimated at 4.45 wt.% Al_2O_3 by Wang and Becker (2013))
 1329 using experimental $D_{\text{Se or Te}}^{\text{sulf liq-sil}}$ of (1) 1086 and 8789 (used in the melting model of Brenan (2015)) and (2) 850
 1330 and 3800 (same as above; Kiseeva et al., 2017) for Se and Te, respectively. For this modelling, major element
 1331 compositions are from PM of McDonough and Sun (1995) and SCSS is calculated accordingly using parameters
 1332 from pMELTS. The light yellow shaded areas in (c) are the range of residue compositions with a typical fertile
 1333 mantle S content (200 ± 40 $\mu\text{g g}^{-1}$; e.g., Lorand, 1991; Palme and O’Neill, 2014). Our result shows that,
 1334 regardless of the choice of source Se–Te contents and experimental $D_{\text{Se or Te}}^{\text{sulf liq-sil}}$ data, the Se–Te pattern displayed
 1335 by lherzolites is inconsistent with melt depletion involving sulfide liquid–silicate melt fractionation (all solid
 1336 black and red lines; b and c), which is suggested here to control Se–Te partitioning during mantle melting ($D_{\text{Se}}^{\text{bulk}}$
 1337 $\ll D_{\text{Te}}^{\text{bulk}}$; see text for more details). Shown for comparison are the Se–Te contents for the SMAR N- and E-
 1338 MORB primary melts and mantle sources (Lissner et al., 2014). Lherzolite (>1.5 wt.% Al_2O_3) and harzburgite
 1339 (<1.5 wt.% Al_2O_3) data are from Morgan (1986), Lorand and Alard (2010), Wang and Becker (2013), Wang et
 1340 al. (2013), König et al. (2012, 2014, 2015), Luguet et al. (2015), and Harvey et al. (2015).

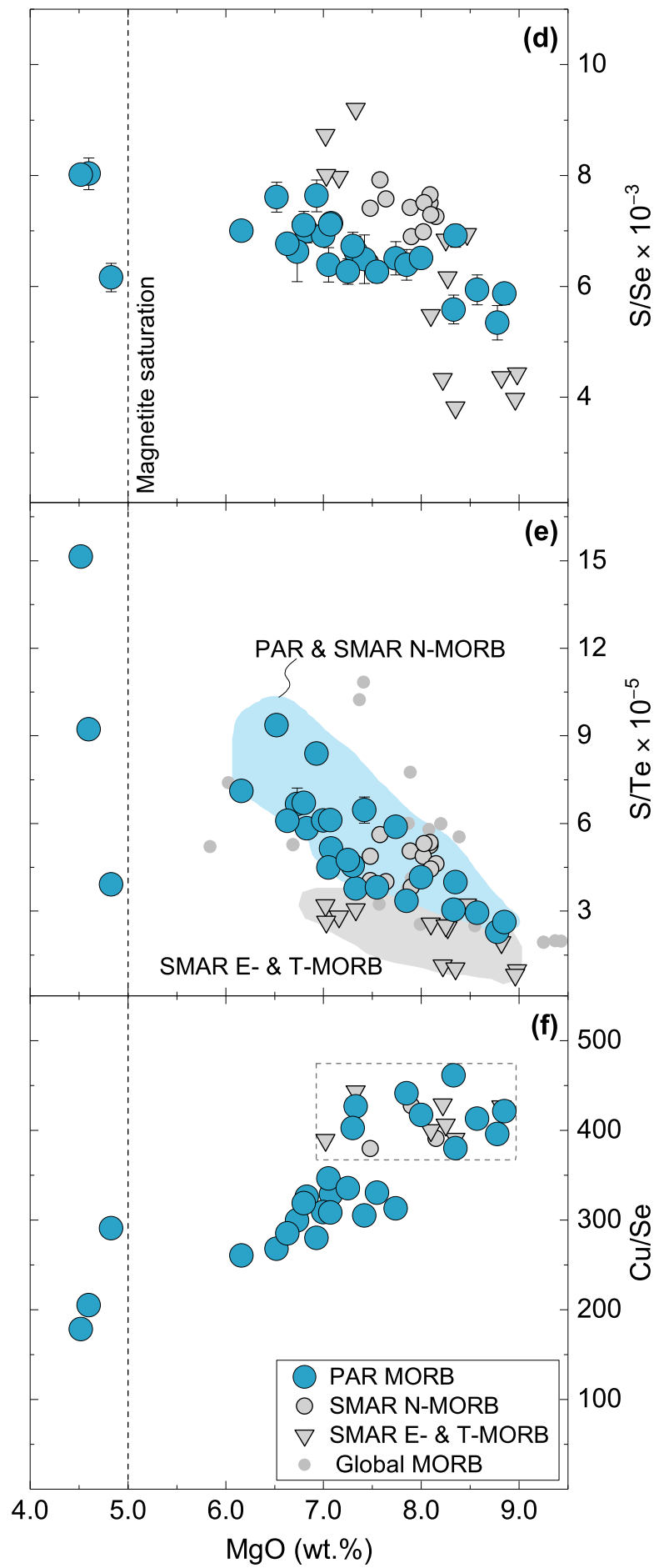
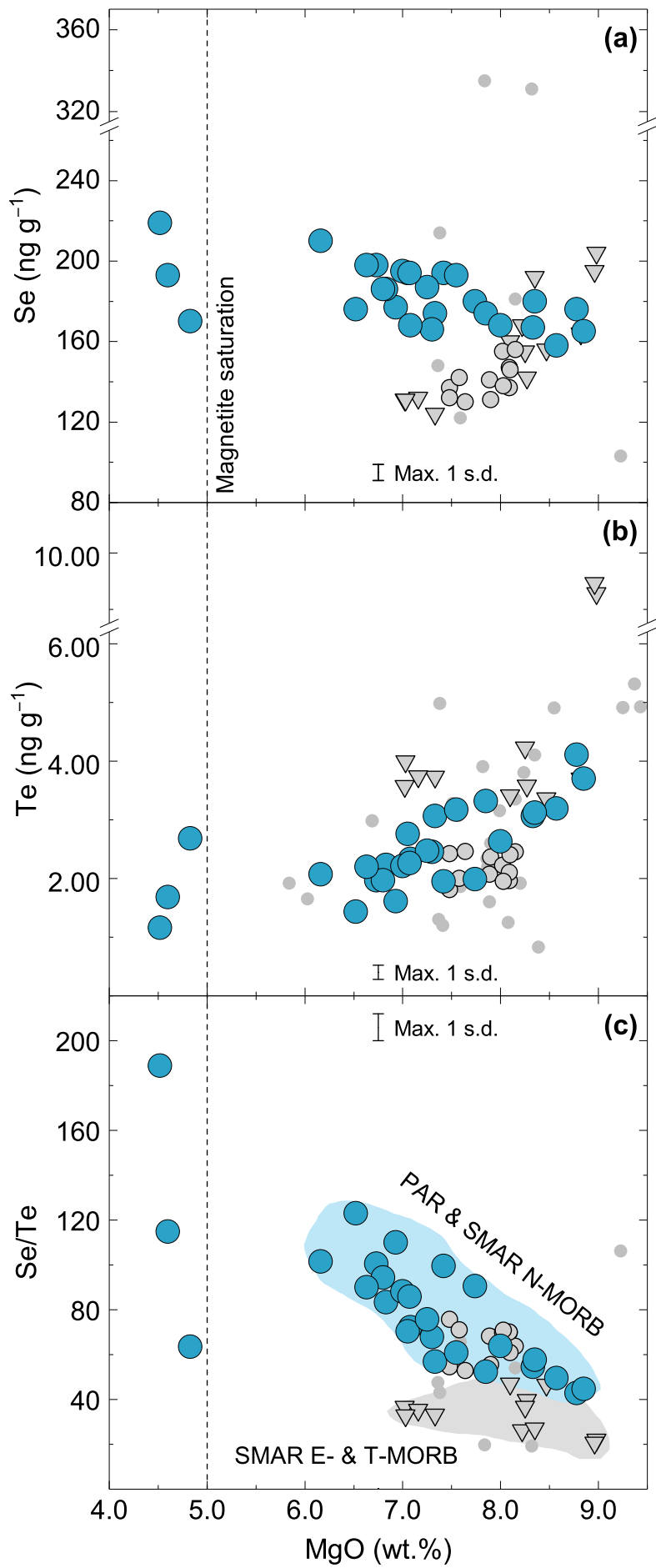
1341 **Fig. 10.** $\delta^{82/76}\text{S}$ plotted against (a) Mg# and (b) Se/Te ratio across the entire MORB evolution according to our
 1342 models of magmatic differentiation and partial melting. Also shown for comparison are $\delta^{82/76}\text{S}$ (± 2 s.d.) and

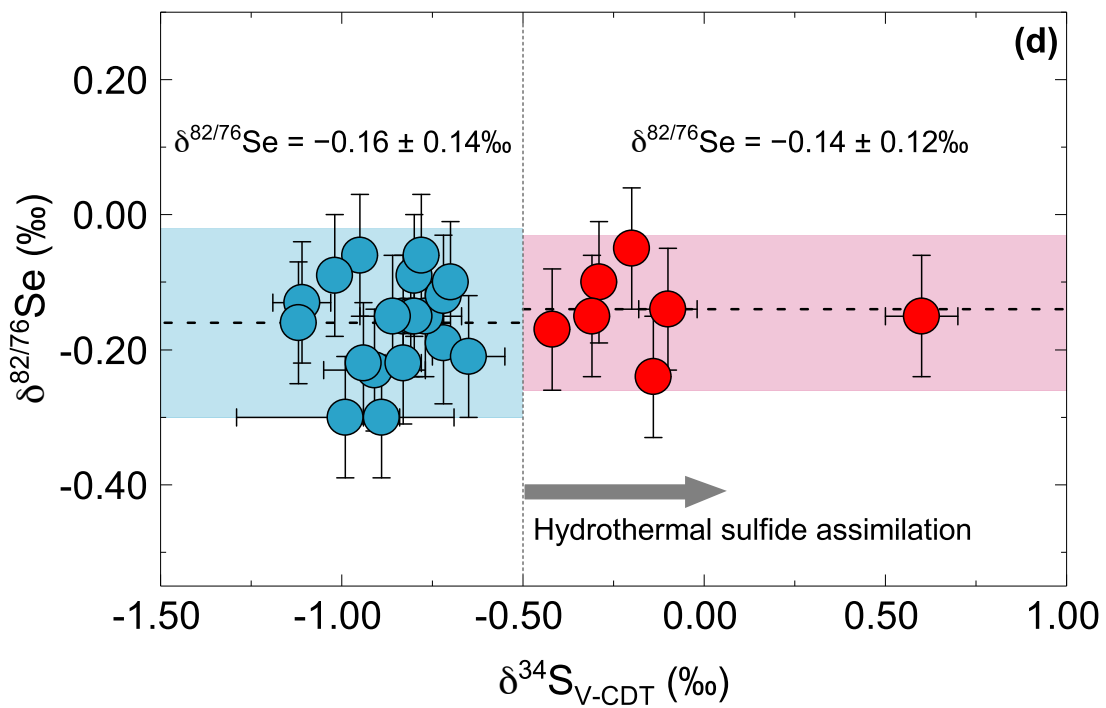
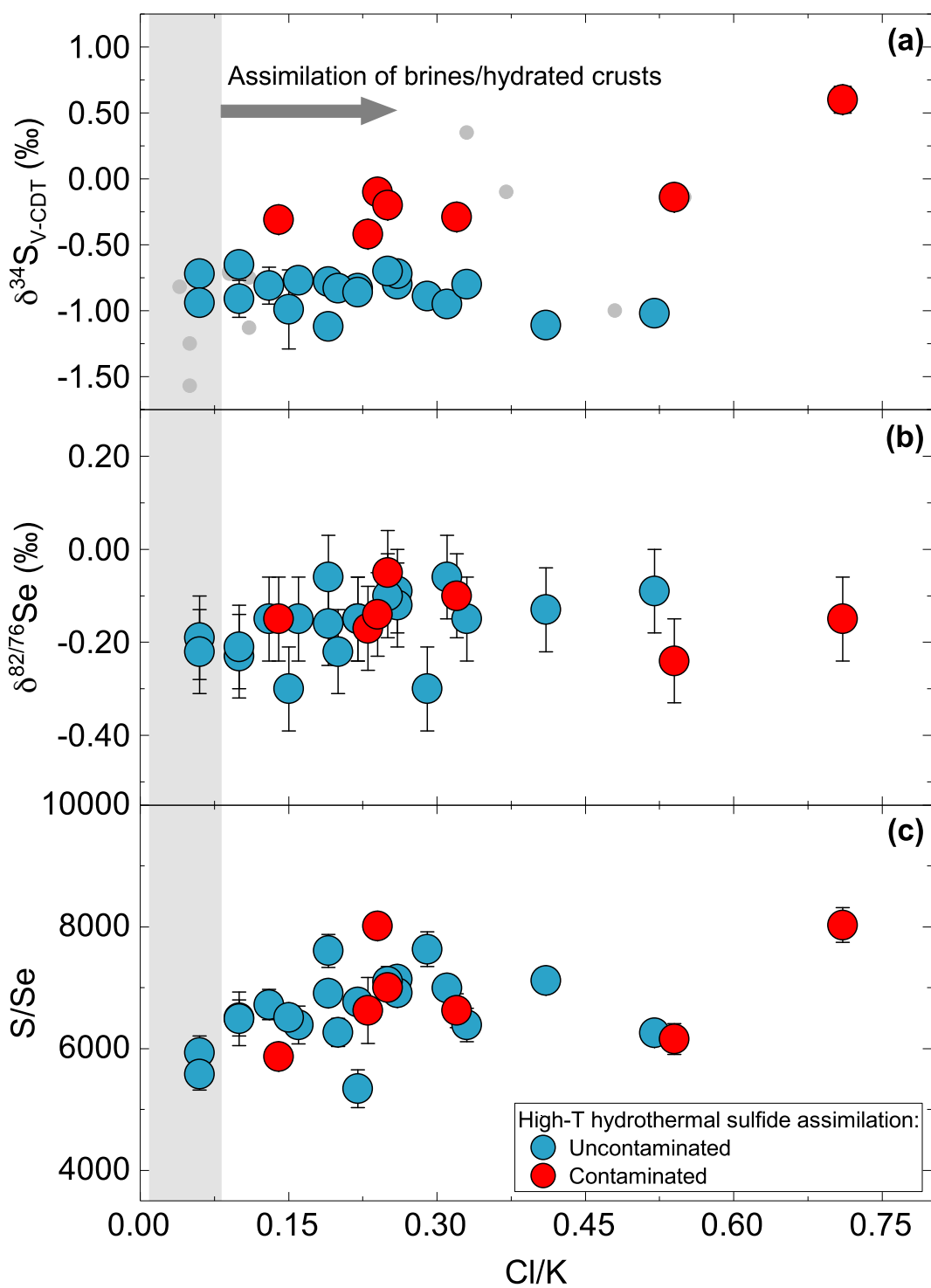
1343 Se/Te (± 1 s.d.) data for basaltic reference materials and main chondrite groups (also see Fig. 3). Each shaded
1344 field represents the average $\delta^{82/76}\text{Se}$ with 2 s.d. uncertainty and range of Mg# (a) or Se/Te (b). The mass fractions
1345 of the fractionated crystals and sulfides are relative to the initial primary melt (a). Selenium isotope compositions
1346 of the primary PAR melt and MORB mantle source are represented by the average $\delta^{82/76}\text{Se}$ value of all PAR
1347 glasses ($-0.16 \pm 0.13\%$; 2 s.d., $n = 27$) based on the demonstrated absence of Se isotope fractionation during Se
1348 partitioning between sulfide (liquid and/or crystalline MSS) and silicate melt ($\Delta^{82/76}\text{Se}_{\text{sulf-sil}} \approx 0.00\%$). Both
1349 mantle source compositions estimated for PAR MROBs were shown: 80 ± 17 and $11 \pm 1.7 \text{ ng g}^{-1}$ (source 1) and
1350 49 ± 11 and $3.5 \pm 1.3 \text{ ng g}^{-1}$ (source 2) Se and Te, respectively (also see Fig. 8 and 9; symbols in (a) were slightly
1351 staggered for clarity). $\delta^{82/76}\text{Se}$ and Se/Te ratios of all basaltic reference materials are from this study and Yierpan
1352 et al. (2018) and $\delta^{82/76}\text{Se}$ of BCR-2 is also taken from Kurzawa et al. (2017) (also see Fig. 1). For chondrites,
1353 $\delta^{82/76}\text{Se}$ are from Labidi et al. (2018) and the Se/Te ratios from Wasson and Kallemeyn (1988), Lodders et al.
1354 (2009), Schaefer and Fegley (2010), and Wang and Becker (2013).

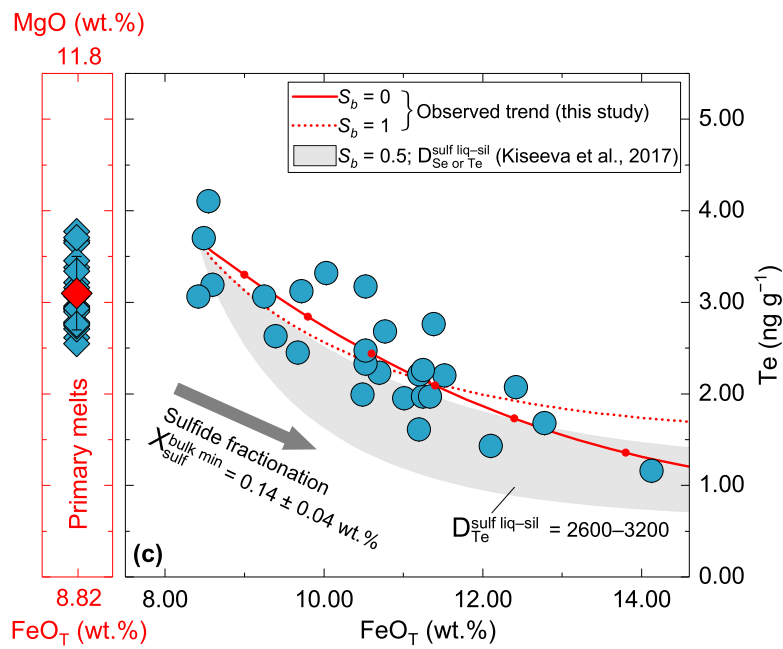
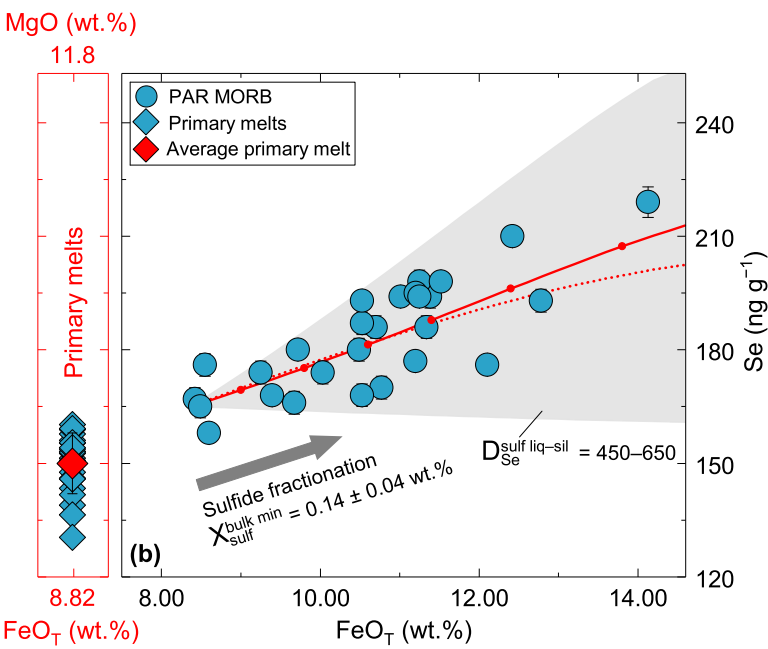
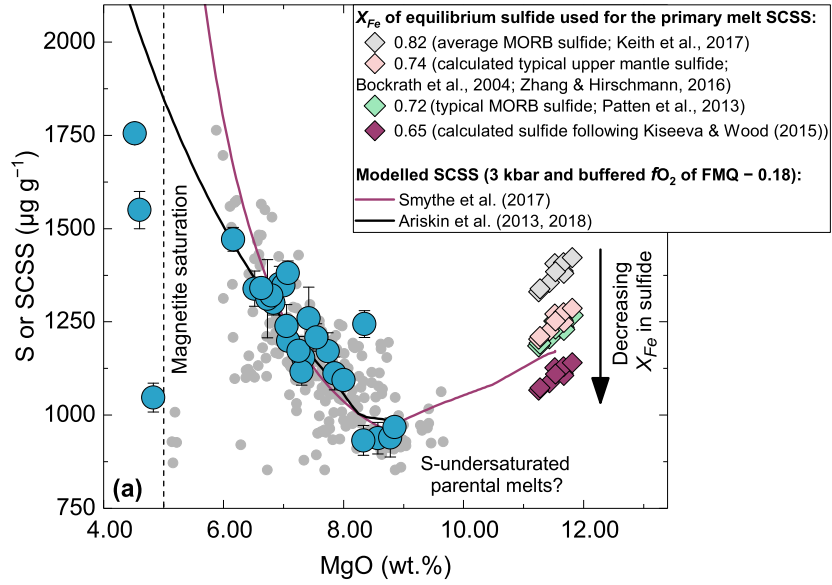


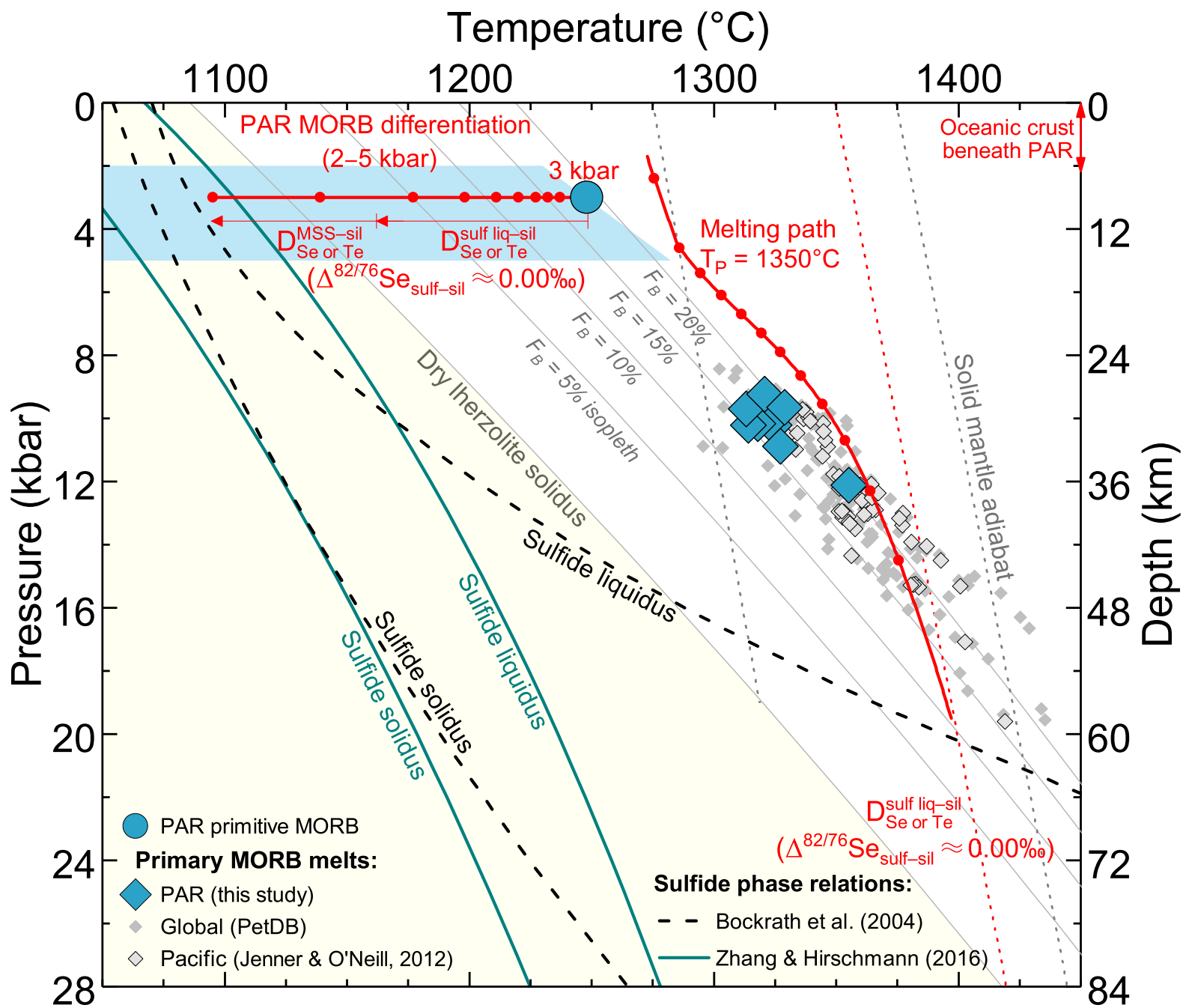


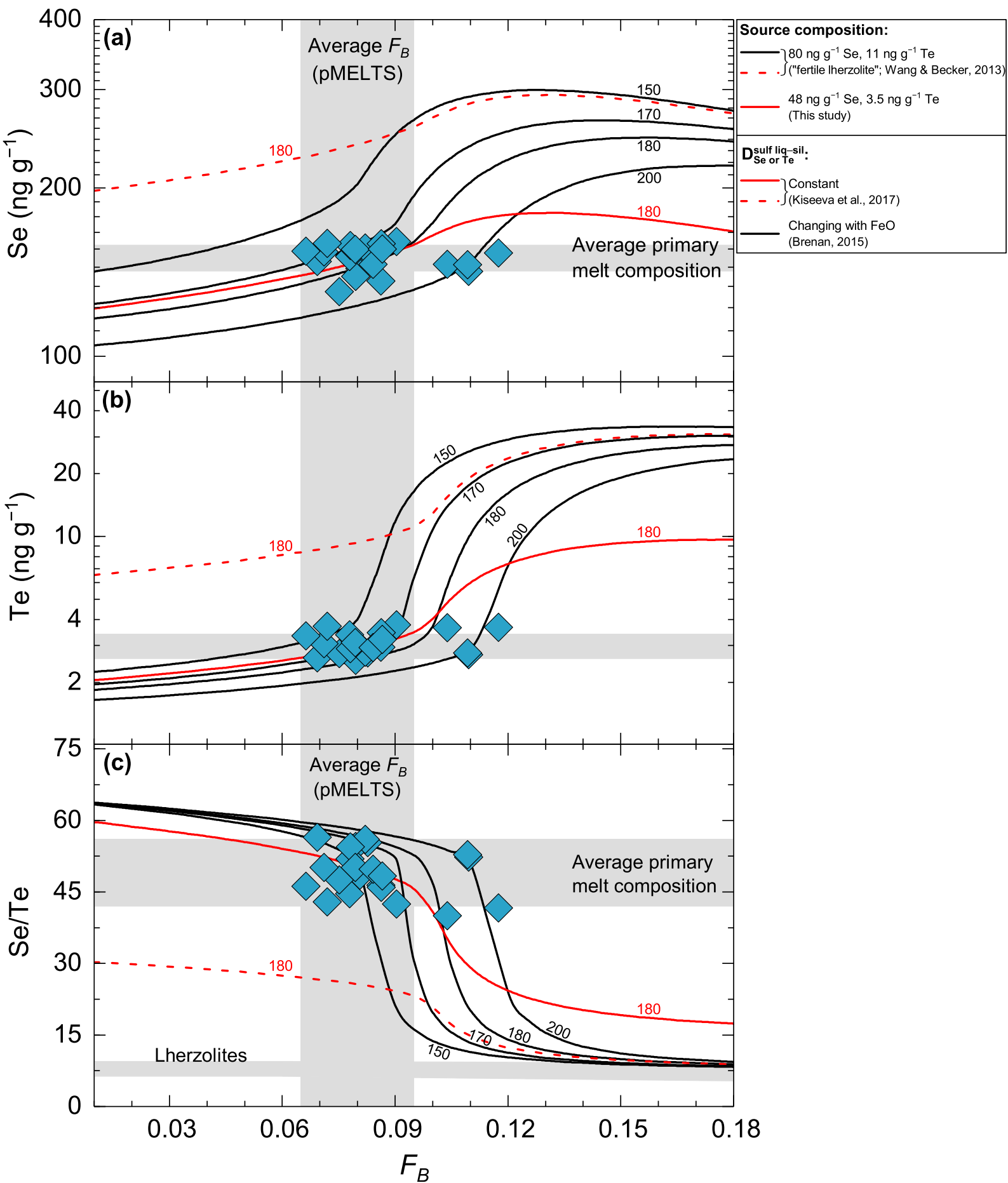


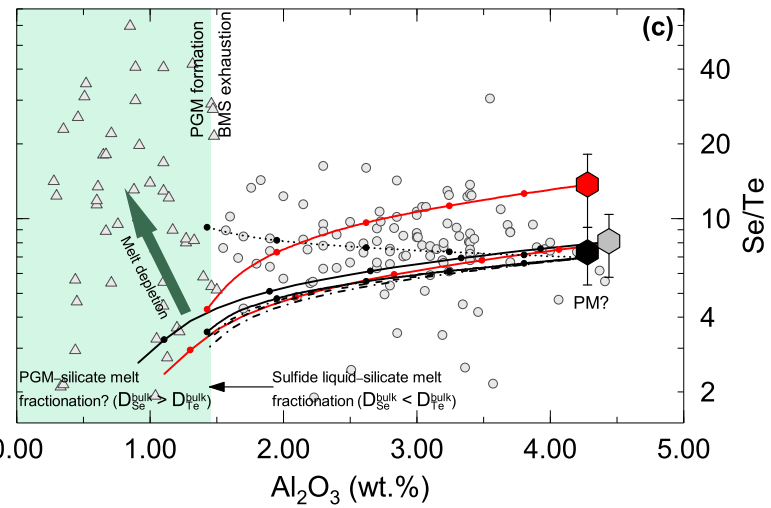
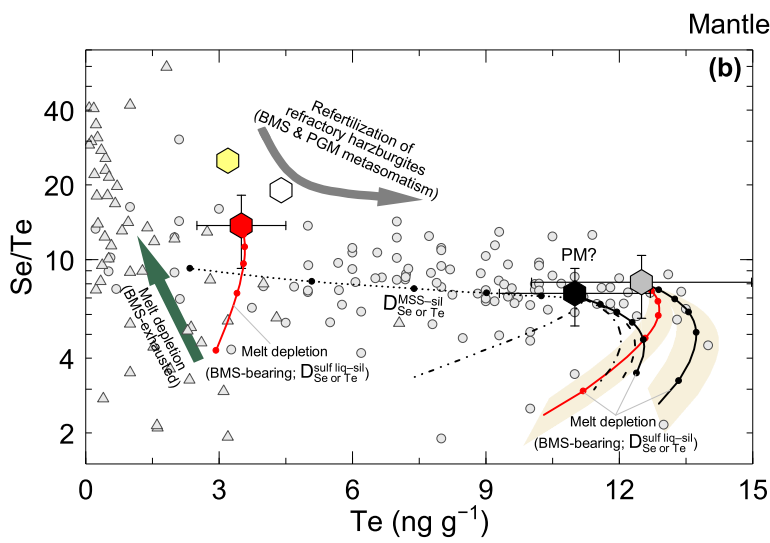
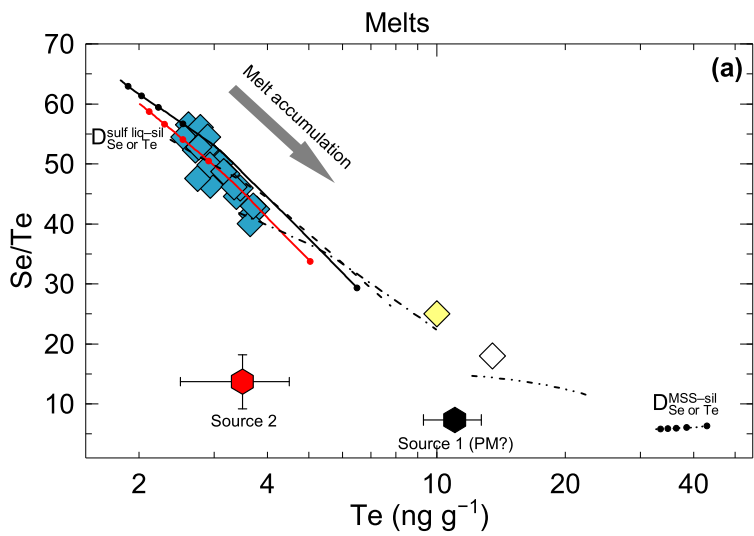


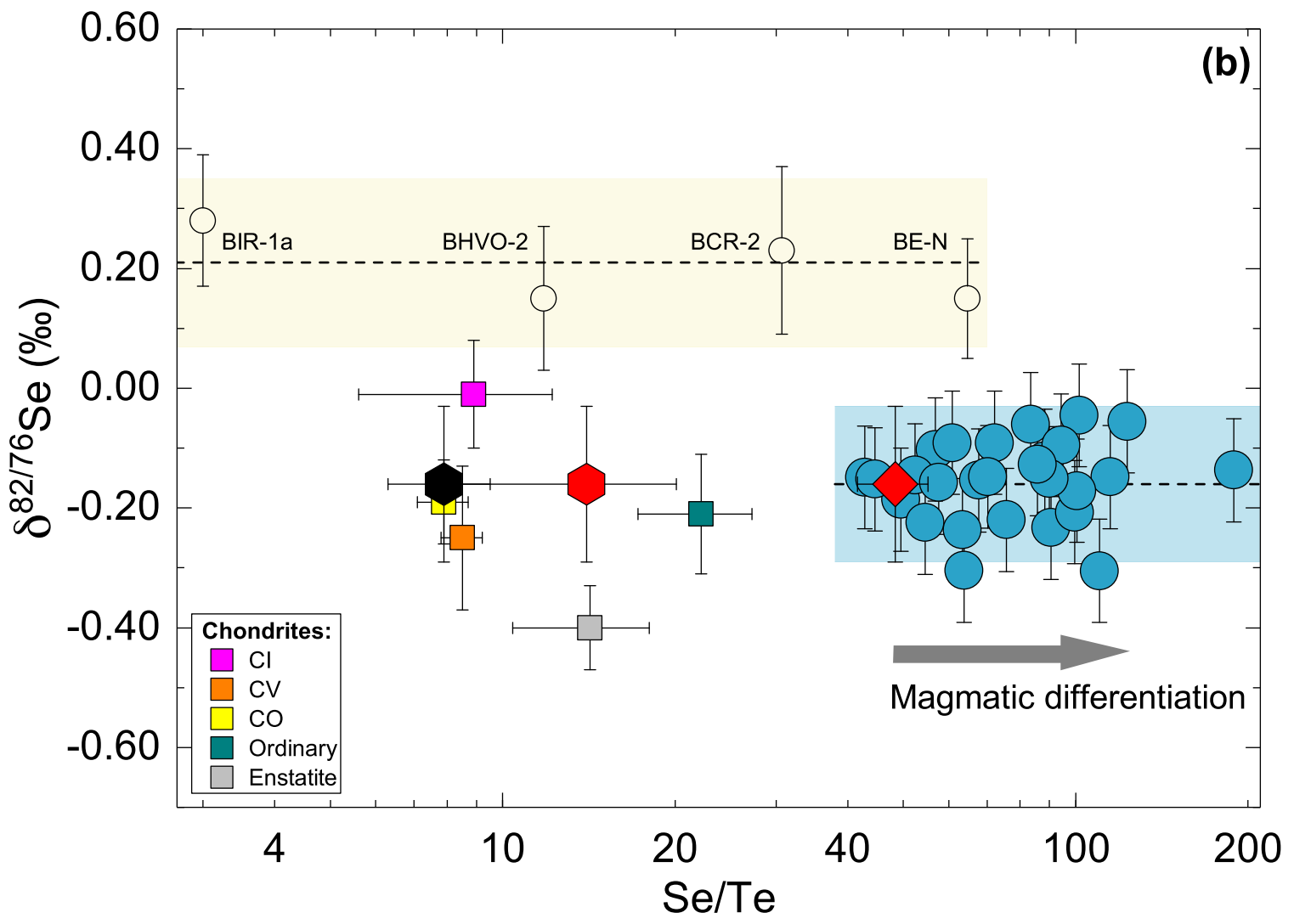
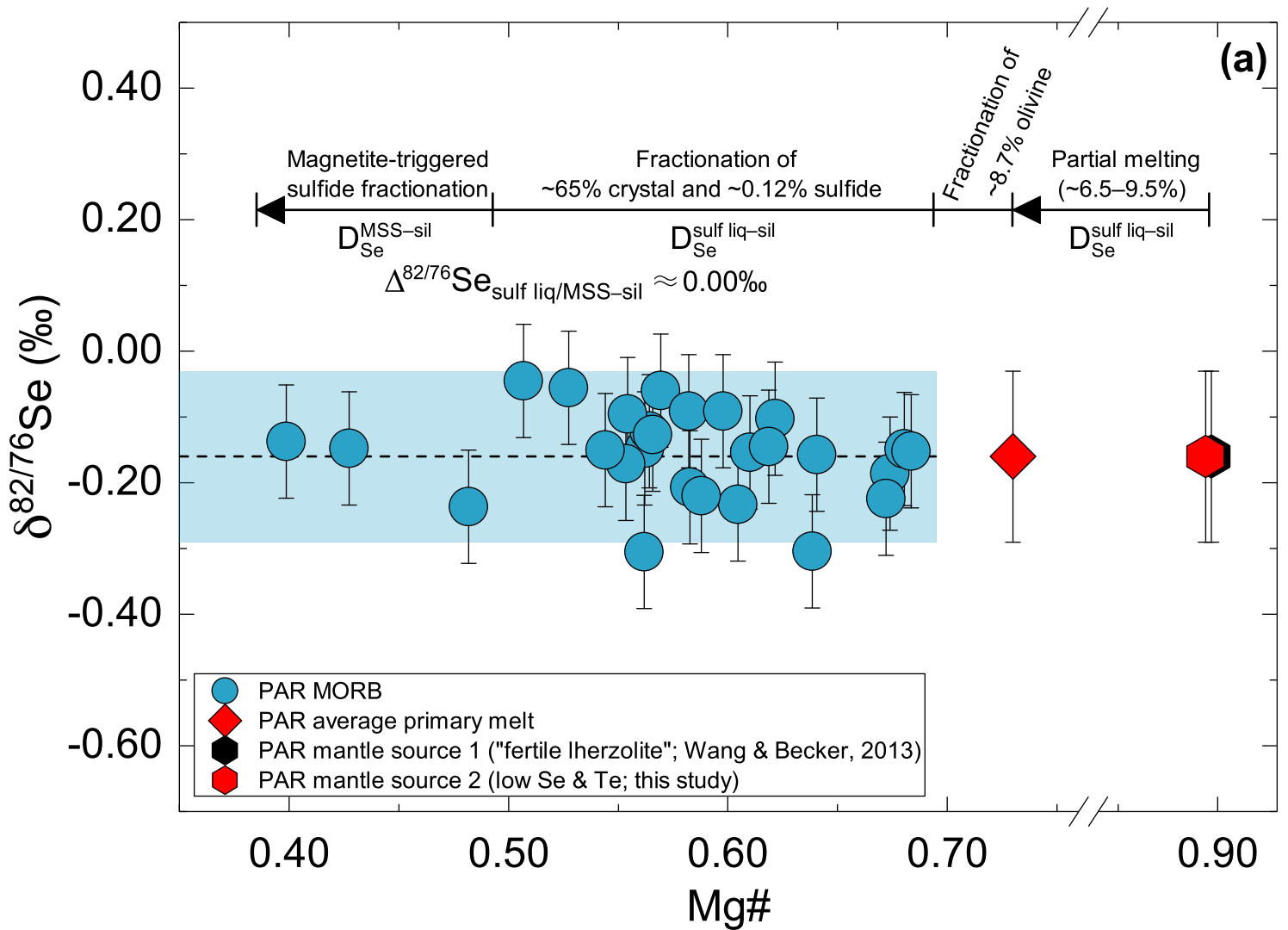












Electronic Annex Supplementary Material for

Selenium isotope and S–Se–Te elemental systematics along the Pacific–Antarctic ridge: Role of mantle processes

Aierken Yierpan^{a,*}, Stephan König^a, Jabrane Labidi^{a,b}, Ronny Schoenberg^{a,c}

^a Isotope Geochemistry, Department of Geosciences, Eberhard Karls University of Tübingen, Wilhelmstrasse 56, 72074 Tübingen, Germany

^b Department of Earth, Planetary, and Space Sciences, University of California Los Angeles, Los Angeles, CA, USA

^c Department of Geology, University of Johannesburg, P.O. Box 524, Auckland Park 2006, South Africa

* Corresponding author (*E-mail*: aierken.yierpan@uni-tuebingen.de; *Tel.*: +49-(0)7071-29-78907)

This Supplementary Material includes

Supplementary Text (S1 and S2)

Supplementary Table Captions (Tables S1–S3 are uploaded separately as an Excel file)

Supplementary Figures (Fig. S1–S6) and Figure Captions

S1. Modelling Se–Te variations during MORB differentiation

The observed major element systematics were first constrained using a simple fractional crystallization model, which is generally considered as a dominant process during low-pressure magmatic evolution, especially in fast spreading ridges (Grove et al., 1992; Sinton and Detrick, 1992; Perfit, 2001) as in the case of the studied PAR segments (see Main Text Section 2). The liquid lines of descents (LLDs) were modelled with alphaMELTS front end (MELTS mode; Version 1.8) run in isobaric mode (Ghiorso and Sack, 1995; Smith and Asimow, 2005). Calculations were performed starting from the most primitive glass PAC1 DR12-1g (Electronic Annex 2 Table S1) at 2–7 kbar along a buffered fO_2 of 0.18 log units below the FMQ buffer (Zhang H. L. et al., 2018). The modelled trends at 2–5 kbar broadly reproduce the observed variations of most major elements (Fig. S3), reflecting a comagmatic origin of the entire PAR on-axis (Vlastélic et al., 2000; Hamelin et al., 2010). The observed Se–Te variations were subsequently modelled using FeO_T as an index of differentiation due to their tight covariations as mentioned in Main Text Section 5.2 (also see Main Text Fig. 6). Note that FeO_T content of the PAR samples monotonically increases with ongoing crystal fractionation prior to magnetite saturation (Fig.

S3). The modelled LLDs for FeO_T yields the best match with the observed trend at 3 kbar and the resulting parameters were used in the subsequent modelling.

The Se–Te partitioning between the bulk fractionated minerals (i.e., silicate crystals + sulfide phase) and silicate melt ($D_{Se\ or\ Te}^{bulk}$) is described by

$$D_{Se\ or\ Te}^{bulk} = \frac{X_{sulf}}{1-f} D_{Se\ or\ Te}^{sulf-sil} + \frac{X_{cryst}}{1-f} D_{Se\ or\ Te}^{cryst-sil} \quad (1)$$

where f , X_{sulf} , and X_{cryst} are the mass fractions of remaining silicate melt, fractionated immiscible sulfide phase, and silicate crystals, respectively, relative to the initial system (i.e., PAC1 DR12-1g); $D_{Se\ or\ Te}^{sulf-sil}$ and $D_{Se\ or\ Te}^{cryst-sil}$ are the sulfide phase–silicate melt and silicate crystal–silicate melt partition coefficients, respectively. As Se–Te are essentially incompatible in silicate crystals (assuming $D_{Se\ or\ Te}^{cryst-sil} = 0.001$; Brenan, 2015), Eq. (1) can be approximated as

$$D_{Se\ or\ Te}^{bulk} = \frac{X_{sulf}}{1-f} D_{Se\ or\ Te}^{sulf-sil} \quad (2)$$

Considering that all fractionated S is exclusively partitioned into sulfide due to its incompatibility in silicate crystals (Labidi et al., 2014), the mass balance allows calculation of X_{sulf} at a given f (directly obtained from alphaMELTS) following

$$X_{sulf} = \frac{C_S^0 - fC_S^l}{C_S^{sulf}} \quad (3)$$

where C_S^0 , C_S^l , and C_S^{sulf} are the S concentrations of the initial high-MgO melts (on average $968 \pm 26 \mu\text{g g}^{-1}$; Main Text Table 2 and Fig. 6a), remaining melt, and segregated sulfides, respectively. The term $\frac{X_{sulf}}{1-f}$ in Eq. (2) represents the proportion of sulfide in the bulk fractionated minerals ($X_{sulf}^{bulk\ min}$). For the studied PAR glasses that have not experienced magnetite saturation-triggered sulfide segregation (see Main Text Section 5.2 and Fig. 6a), we obtain $X_{sulf}^{bulk\ min}$ ranging between 0.09 and 0.20 wt.% averaging at 0.14 ± 0.04 wt.%, consistent with the previous estimate for a larger set of samples (0.19 ± 0.07 wt.%; assuming $C_S^{sulf} = 35$ wt.%; Labidi et al., 2014).

As for $D_{Se\ or\ Te}^{sulf-sil}$, previous studies reported a wide range of values (Peach et al., 1990; Barnes et al., 2009; Patten et al., 2013; Brenan, 2015; Kiseeva et al., 2017). Two partitioning experiments show that $D_{Se\ or\ Te}^{sulf-sil}$ strongly depends on the fractionating sulfide phase (crystalline monosulphide solid solution (MSS) and sulfide liquid) and FeO content of the silicate melt (Brenan, 2015; Kiseeva et al., 2017). Both elements are highly compatible in sulfides relative to silicates, whereas Te is more compatible in sulfide liquid and Se is more compatible in MSS (Brenan, 2015). For sulfide liquid–silicate melt partitioning ($D_{Se\ or\ Te}^{sulf\ liq-sil}$), these studies reported significantly different values. For a basaltic melt with 8–11 wt.% FeO, Kiseeva et al. (2017) reported $D_{Se}^{sulf\ liq-sil} = 450\text{--}650$

and $D_{Te}^{sulf\ liq-sil} = 2600-3200$, much lower than $D_{Se}^{sulf\ liq-sil} = 1050 \pm 360-1460 \pm 400$ and $D_{Te}^{sulf\ liq-sil} = 9720 \pm 1170-13640 \pm 1590$ (1 s.d. propagated error) expected from the formula of Brenan (2015), respectively ($D_{Se\ or\ Te}^{sulf\ liq-sil}$ decreases with increasing FeO content of the silicate melt). In the case of the evolving PAR melts with FeO_T from 8.49 to 12.78 wt.% (Main Text Fig. 6b and c; MgO from ~8.85–5.5 wt.%; Fig. S3), assuming $Fe^{2+}/\Sigma Fe = 0.87$ (Bézos and Humler, 2005; Zhang H. L. et al., 2018), we obtain $1560 \pm 410-1035 \pm 360$ for $D_{Se}^{sulf\ liq-sil}$ and $14430 \pm 1680-9570 \pm 1150$ for $D_{Te}^{sulf\ liq-sil}$ (both 1 s.d.) following Brenan (2015). Both these values and $D_{Se\ or\ Te}^{sulf\ liq-sil}$ from Kiseeva et al. (2017), together with $X_{sulf}^{bulk\ min} = 0.14 \pm 0.04$ wt.%, are used to derive $D_{Se\ or\ Te}^{bulk}$ using Eq. (2). Finally, the model Se–Te concentrations were calculated using the fractional (Eq. 4) and/or batch crystallization (Eq. 5) laws following

$$C_{Se\ or\ Te}^l = C_{Se\ or\ Te}^0 f^{D_{Se\ or\ Te}^{bulk} - 1} \quad (4)$$

and/or

$$C_{Se\ or\ Te}^l = \frac{C_{Se\ or\ Te}^0}{f + D_{Se\ or\ Te}^{bulk}(1 - f)} \quad (5)$$

where $C_{Se\ or\ Te}^l$ and $C_{Se\ or\ Te}^0$ are Se–Te concentrations of the remaining melt at a given f and the initial melt (PAC1 DR12-1g; Main Text Table 2), respectively.

S2. Modelling Se–Te variations during partial melting

The variations of Se–Te during partial melting were modelled for a triangular passive-flow near-fractional melting regime, which has been previously used to explain the Se–Te and highly siderophile element systematics of MORB melts (Rehkämper et al., 1999; Bézos et al., 2005; Mungall and Brenan, 2014; Lissner et al., 2014; Brenan, 2015). The procedures of our model basically follow that detailed by Rehkämper et al. (1999) and Brenan (2015). Briefly, we assume a simplified two-phase mineralogy for the mantle source, which consists of sulfides (sulfide liquid with/without MSS) and bulk silicate minerals. The Se–Te concentrations of each melt increment (1%; relative to the initial system mass) and the residue are calculated by the batch melting equation (Shaw, 1970) with $D_{Se\ or\ Te}^{bulk}$ using experimentally determined $D_{Se\ or\ Te}^{sulf\ liq-sil}$ and/or $D_{Se\ or\ Te}^{MSS-sil}$ values while assuming $D_{Se\ or\ Te}^{cryst-sil} = 0.001$ (Brenan, 2015; Kiseeva et al., 2017; see Section S1). After each equilibrium melting step, 0.1% of the fractional melt is retained (by simple batch mixing) to refertilize the residual mantle column and the rest is extracted. The mineral modes (sulfide and silicate) and composition (S–Se–Te contents) of the residue (i.e., the source for the next melting step) are recalculated accordingly. Finally, the polybaric column-melts produced over the entire two-dimensional melting zone are pooled completely and produce the PAR primary melts at a mean extent of melting F_B (defined as the mass fraction of all melts relative to the initial solid entering the melting region), which is approximated as $\frac{F_{max}}{2}$, where F_{max} is the maximum extent of melting achieved in the

central melting column (Langmuir et al., 1992; Plank et al., 1995; Rehkämper et al., 1999). Sulfur contents of the residue and partial melts at each step depend on the initial S content of the source and SCSS of the aggregate melt in a specific melting column. When the S content of the residue is insufficient to keep the equilibrium melt S-saturated, S starts to behave as an incompatible element (with $D_S^{crys-sil} = 0.001$; Labidi et al., 2014). Upon sulfide exhaustion in a column, S content of the aggregate melt is simply diluted as the subsequent melt increments essentially become S-free. We note that this may be an oversimplification in some cases. For instance, S systematics in the Garrett transform fault lavas, which might have formed by re-melting of a depleted MORB source ($F_B \approx 10\%$ for both melting events; see discussion and Fig. S5a for the typical F_B of S undersaturation in aggregate MORB melts), are similar to those observed in global sulfide-saturated MORBs, requiring that their source (after the first MORB melting event) kept the melts sulfide-saturated (Labidi and Cartigny, 2016). However, generally, MORB melts produced in a triangular melting regime typical for fast-spreading ridges (e.g., Langmuir and Forsyth, 2007; Langmuir et al., 1992; Lin and Morgan, 1992; Brown and Leshner, 2016; and references therein) represent a mixture of S-saturated partial melts (coming from low- F sulfide-bearing mantle columns) and S-undersaturated partial melts (from high- F (e.g., $\sim 20\%$) S-exhausted mantle columns) (also see Ding and Dasgupta, 2017).

The model parameters used here are summarized in Main Text Table 3. The melt major element compositions and pressure-temperature (P–T) conditions for calculating the SCSS of the aggregate melt in a melting column (Smythe et al., 2017) and $D_{Se\ or\ Te}^{sulf\ liq-sil}$ (as a function of FeO; for each incremental/equilibrium melt; Brenan, 2015; Kiseeva et al., 2017) were modelled with alphaMELTS front end run in pMELTS mode (Ghiorso et al., 2002; Smith and Asimow, 2005), following a similar approach used by Ding and Dasgupta (2017). The relevant mantle potential temperature (T_P) for the PAR MORBs was estimated based on the previously determined primary melt–mantle equilibration P–T (on average ~ 10.2 kbar and 1325°C ; Main Text Section 5.2.2), which falls between 1275 and 1350°C , in accordance with the previous estimates for global MORBs (Main Text Fig. 7; Lee et al., 2009; Ding and Dasgupta, 2017). The pMELTS calculation with $T_P = 1350^\circ\text{C}$ may be adequate for our purpose because each P–T data for the aggregate PAR primary melts represents the weighted average P–T of melt extraction from all mantle parcels across the triangular melting zone and thus lies below the polybaric melting path (Main Text Fig. 7; Asimow and Longhi, 2004; Lee et al., 2009). The composition of the depleted MORB mantle were taken from Salters and Stracke (2004) assuming 0.2 wt.% Fe_2O_3 (e.g., Cottrell and Kelley, 2011). We obtain a range of temperature from 1389 to 1294°C for the extent of melting F from 0 to 20% , with the corresponding extraction pressures 17.5 to 5.4 kbar for the incremental melts and 17.5 to 9.4 kbar for the aggregate melts (1-D integration over a single melting column). Under these conditions, the calculated $D_{Se\ or\ Te}^{sulf\ liq-sil}$ values following Brenan (2015) at each melting step are 1414 ± 401 – 1900 ± 435 for $D_{Se}^{sulf\ liq-sil}$ and 13199 ± 1541 – 16811 ± 1940 for $D_{Te}^{sulf\ liq-sil}$ (1 s.d. propagated uncertainty), increasing with progressive melting due to the decreasing FeO content of the fractional melts (~ 8.34 – 5.37 wt.%). These values are considerably higher than that used by Brenan (2015) for the melting model, which are 1086 and 8789 for Se

and Te, respectively (chosen at an empirical FeO content of 10 wt.%). At this range of FeO content, $D_{Se\ or\ Te}^{sulf\ liq-sil}$ values of Kiseeva et al. (2017) should be 550–850 and 3000–3800 for Se and Te, respectively (see Section S1 for the different results between two studies).

As for estimating the average melting degree for the PAR MORBs, we used (incompatible) trace element systematics (Fig. S4). The primary melt compositions (on average ~11.8 wt.% MgO and Mg# = 0.73) were obtained by a similar method used for Se–Te (see Main Text Section 5.2.2). Briefly, measured concentrations (Electronic Annex 2 Table S1) were first corrected to MgO content (8.85 wt.%) of the most primitive glass by linear regression. This was followed by correcting for ~8.7% olivine fractionation considering that these elements are highly incompatible in olivine (e.g., Bédard, 2005). The average melting degree was then estimated in two different approaches: (1) by solving the simple batch melting equation for F_B using concentration of each trace element i (C_i^{melt}) for all primary melts ($n = 24$) and the source (C_i^{mantle} ; depleted MORB mantle; Salters and Stracke, 2004) with empirical mantle–melt bulk partition coefficients ($D_i^{mantle-melt}$) following the approach of Kelley et al. (2006):

$$F_B = \frac{\frac{C_i^{mantle}}{C_i^{melt}} - D_i^{mantle-melt}}{1 - D_i^{mantle-melt}} \quad (5)$$

which yields F_B from ~6.6 to ~11.7% (average $8.5 \pm 1.5\%$; 1 s.d., $n = 24$); and (2) comparing the results obtained from pMELTS for the accumulated melts (over the entire triangular melting region) to our calculated primary melt concentrations, which gives a best match if F_B ranges between 6.5 and 9.5% (Fig. S4). Both results are in excellent agreement and, meanwhile, consistent with the previous estimates for global MORBs (e.g., Klein and Langmuir, 1987; Salters and Stracke, 2004; Workman and Hart, 2005; Kimura et al., 2017). Besides, our calculated primary melt–mantle equilibration P–T for PAR glasses, together with most global MORBs, fall between 10–20% melt fraction isopleths estimated for a fertile lherzolite (Main Text Fig. 7; Katz et al., 2003; Lee et al., 2009). Lower melt fractions would be expected for a depleted MORB source mantle due to its relatively higher solidus (Lee et al., 2009), which may then be broadly consistent with our estimated F_B .

Three different mantle sulfides (Fe–Ni–Cu BMS) were used to calculate the SCSS of the partial melts considering that the equilibrium sulfide chemistry significantly affects the S solubility as FeS activity decreases due to the presence of Ni and Cu, i.e., SCSS decreases with decreasing $X_{Fe} = \frac{Fe}{Fe + Ni + Cu}$ (molar ratio) (e.g., Ariskin et al., 2013, 2018; Ding and Dasgupta, 2017; Ding et al., 2018; Smythe et al., 2017). The calculated chemical formulas are shown in Fig. S5. Sulfide A has a relatively refractory composition and was used in the melting experiments of Bockrath et al. (2004) and Zhang Z. and Hirschmann (2016) to obtain the sulfide solidus and liquidus as shown in Main Text Fig. 7. Sulfide B is calculated assuming 25 wt.% Ni + 5 wt.% Cu (used in the melting model of Ding and Dasgupta (2017)) and metal/S atomic ratio of 0.93 that is typical for shallow mantle sulfides under relatively oxidized conditions (e.g., MORB source mantle; Zhang Z. et al., 2018; also see

Lorand and Luguët, 2016). For sulfide C, we first estimated its $\frac{\text{Ni}}{\text{Ni} + \text{Fe}}$ molar ratio using the Ni and FeO contents of olivine in the residue (~10.06–9.01 wt.% FeO and ~1964–2349 $\mu\text{g g}^{-1}$ Ni for 0–20% melting; from pMELTS) and sulfide melt–olivine Fe–Ni exchange relations following Zhang Z. et al. (2018):

$$\frac{(\text{Ni}/\text{Fe})_{\text{sulfliq}}}{(\text{Ni}/\text{Fe})_{\text{olivine}}} = 14.33 \frac{\text{Ni}}{\text{Ni} + \text{Fe}} + 39.45 \quad (6)$$

which yields 0.53–0.60 (increasing with increasing F). The weight fractions of Fe, Ni, and S are then calculated with a constant $\frac{\text{Ni}}{\text{Ni} + \text{Fe}} = 0.53$ while taking metal/S ratio of 0.93 (Zhang Z. et al., 2018) and 5 wt.% Cu (Kiseeva et al., 2017).

Because there are a large number of model parameters, we first validate our model for the variation of chalcophile elements S and Cu during melting (Fig. S5) because (1) S and Cu abundances in the mantle are relatively well constrained using different approaches by several studies (e.g., Mcdonough and Sun, 1995; Salters and Stracke, 2004; Lorand and Luguët, 2016; Lorand et al., 2013; Wang and Becker, 2013, 2015b; Palme and O'Neill, 2014); (2) their behavior during partial melting has been systematically modelled using experimentally determined partition coefficients (e.g., Lee et al., 2009; Li and Audétat, 2012; Kiseeva and Wood, 2013, 2015; Brenan, 2015) and a large number of analyses in MORB melts (e.g., Jenner and O'Neill, 2012; Labidi et al., 2014) with a variety of SCSS models, source contents, and T_P (Lee et al., 2009; Li and Audétat, 2012; Ding and Dasgupta, 2017). The S of contents used for the PAR MORB source mantle ranges from “PM-like” 200 $\mu\text{g g}^{-1}$ (e.g., Lorand et al., 2013; Palme and O'Neill, 2014; Wang and Becker, 2013) to slightly lower 150 $\mu\text{g g}^{-1}$ as estimated for the depleted MORB mantle (e.g., Luguët et al., 2003; Bézoz et al., 2005; Nielsen et al., 2014; Lorand and Luguët, 2016). A starting Cu content of $30 \pm 6 \mu\text{g g}^{-1}$ is used, as suggested for the PM (Mcdonough and Sun, 1995; Wang and Becker, 2015b) as well as the depleted MORB mantle (Salters and Stracke, 2004). Partition coefficients of Cu between silicate minerals and melt ($D_{\text{Cu}}^{\text{cryst-sil}}$) are taken from Lee et al. (2009). $D_{\text{Cu}}^{\text{sulfliq-sil}}$ is taken as 1000 (Li and Audétat, 2012), which has been used in several studies for modelling the behavior of Cu (e.g., Ding and Dasgupta, 2017; Wang and Becker, 2015b). The primary melt S and Cu contents (after correcting for sulfide + crystal fractionation) are calculated by the same approach used for Se and Te contents (Main Text Section 5.2.2). Our result (Fig. S5) shows that, with the SCSS model of Smythe et al. (2017) and equilibrium sulfide composition B ($X_{\text{Fe}} = 0.54$; $\frac{\text{Ni}}{\text{Ni} + \text{Fe}} = 0.42$; Fig. S5a), the PAR primary melt S concentrations are very well reproduced with our partial melting model for the estimated F_B of the samples using a range of source S content (150–200 $\mu\text{g g}^{-1}$). Note that the chemistry of sulfide B used here is also consistent with typical lherzolite-hosted sulfide compositions (e.g., Lorand and Luguët, 2016) as well as the suggested range of $\frac{\text{Ni}}{\text{Ni} + \text{Fe}}$ value for a shallow mantle Cu-free sulfide (0.4–0.6) by Zhang Z. et al. (2018) at the range of melting depth (from ~50 to 20 km from pMELTS; Maint Text Fig. 7) and $f\text{O}_2$ (~FMQ; Cottrell and Kelley, 2011; Zhang H. L. et al., 2018) estimated for the Pacific–Antarctic MORB. The corresponding model curves also show

a very good fit to the primary melt Cu concentrations with 170–200 $\mu\text{g g}^{-1}$ S and 30 (or 24) $\mu\text{g g}^{-1}$ Cu in the source (Fig. S5b and c). The same parameters are then used for the modelling of Se and Te behavior during partial melting and estimation of the Pacific mantle composition (Fig. S6 and Main Text Fig. 8 and 9).

References

- Ariskin A. A., Bychkov K. A., Nikolaev G. S. and Barmina G. S. (2018). The COMAGMAT-5: Modeling the Effect of Fe–Ni Sulfide Immiscibility in Crystallizing Magmas and Cumulates. *Journal of Petrology*, **59**(2), 283–298. <https://doi.org/10.1093/petrology/egy026>
- Ariskin A. A., Danyushevsky L. V., Bychkov K. A., McNeill A. W., Barmina G. S. and Nikolaev G. S. (2013). Modeling Solubility of Fe–Ni Sulfides in Basaltic Magmas: The Effect of Nickel. *Economic Geology*, **108**(8), 1983–2003. <https://doi.org/10.2113/econgeo.108.8.1983>
- Asimow P. D. and Longhi J. (2004). The significance of multiple saturation points in the context of polybaric near-fractional melting. *Journal of Petrology*, **45**(12), 2349–2367. <https://doi.org/10.1093/petrology/egh043>
- Barnes S.-J., Savard D., Bédard L. P. and Maier W. D. (2009). Selenium and sulfur concentrations in the Bushveld Complex of South Africa and implications for formation of the platinum-group element deposits. *Mineralium Deposita*, **44**(6), 647–663. <https://doi.org/10.1007/s00126-009-0237-3>
- Bédard J. H. (2005). Partitioning coefficients between olivine and silicate melts. *Lithos*, **83**(3–4), 394–419. <https://doi.org/10.1016/j.lithos.2005.03.011>
- Bézos A. and Humler E. (2005). The $\text{Fe}^{3+}/\Sigma\text{Fe}$ ratios of MORB glasses and their implications for mantle melting. *Geochimica et Cosmochimica Acta*, **69**(3), 711–725. <https://doi.org/10.1016/j.gca.2004.07.026>
- Bézos A., Lorand J. P., Humler E. and Gros M. (2005). Platinum-group element systematics in Mid-Oceanic Ridge basaltic glasses from the Pacific, Atlantic, and Indian Oceans. *Geochimica et Cosmochimica Acta*, **69**(10), 2613–2627. <https://doi.org/10.1016/j.gca.2004.10.023>
- Bockrath C., Ballhaus C. and Holzheid A. (2004). Fractionation of the platinum-group elements during mantle melting. *Science*, **305**(5692), 1951–3. <https://doi.org/10.1126/science.1100160>
- Brenan J. M. (2015). Se–Te fractionation by sulfide–silicate melt partitioning: Implications for the composition of mantle-derived magmas and their melting residues. *Earth and Planetary Science Letters*, **422**, 45–57. <https://doi.org/10.1016/j.epsl.2015.04.011>
- Brown E. L. and Leshner C. E. (2016). REEBOXPRO: A forward model simulating melting of thermally and lithologically variable upwelling mantle. *Geochemistry, Geophysics, Geosystems*, **17**(10), 3929–3968. <https://doi.org/10.1002/2016gc006579>
- Cottrell E. and Kelley K. A. (2011). The oxidation state of Fe in MORB glasses and the oxygen fugacity of the upper mantle. *Earth and Planetary Science Letters*, **305**(3–4), 270–282. <https://doi.org/10.1016/j.epsl.2011.03.014>
- Dare S. A. S., Barnes S. J., Beaudoin G., Méric J., Boutroy E. and Potvin-Doucet C. (2014). Trace elements in magnetite as petrogenetic indicators. *Mineralium Deposita*, **49**(7), 785–796. <https://doi.org/10.1007/s00126-014-0529-0>
- Ding S. and Dasgupta R. (2017). The fate of sulfide during decompression melting of peridotite implications for sulfur inventory of the MORB-source depleted upper mantle. *Earth and Planetary Science Letters*, **459**, 183–195. <https://doi.org/10.1016/j.epsl.2016.11.020>
- Ding S., Hough T. and Dasgupta R. (2018). New high pressure experiments on sulfide saturation of high-FeO* basalts with variable TiO_2 contents – Implications for the sulfur inventory of the lunar interior. *Geochimica et Cosmochimica Acta*, **222**, 319–339. <https://doi.org/10.1016/j.gca.2017.10.025>
- Ghiorso M. S., Hirschmann M. M., Reiners P. W. and Kress V. C. (2002). The pMELTS: A revision of MELTS for improved calculation of phase relations and major element partitioning related to partial melting of the mantle to 3 GPa. *Geochemistry, Geophysics, Geosystems*, **3**(5), 1–35. <https://doi.org/10.1029/2001gc000217>
- Ghiorso M. S. and Sack R. O. (1995). Chemical mass transfer in magmatic processes IV. A revised and internally consistent thermodynamic model for the interpolation and extrapolation of liquid–solid equilibria in magmatic systems at elevated temperatures and pressures. *Contributions to Mineralogy and Petrology*, **119**(2–3), 197–212. <https://doi.org/10.1007/bf00307281>

- Grove T. L., Kinzler R. J. and Bryan W. B., 1992. Fractionation of Mid-Ocean Ridge Basalt (MORB). In: Morgan J. P., Blackman D. K., and Sinton J. M. (Eds.), *Mantle Flow and Melt Generation at Mid-Ocean Ridges, Geophysical Monograph Series*. American Geophysical Union, Washington, D. C., 281-310. <https://doi.org/10.1029/GM071p0281>
- Hamelin C., Dosso L., Hanan B., Barrat J.-A. and Ondréas H. (2010). Sr-Nd-Hf isotopes along the Pacific Antarctic Ridge from 41 to 53°S. *Geophysical Research Letters*, **37**(10). <https://doi.org/10.1029/2010gl042979>
- Hofmann A. W. (1988). Chemical Differentiation of the Earth: the Relationship between Mantle, Continental-Crust, and Oceanic-Crust. *Earth and Planetary Science Letters*, **90**(3), 297-314. [https://doi.org/10.1016/0012-821x\(88\)90132-X](https://doi.org/10.1016/0012-821x(88)90132-X)
- Jenner F. E., Arculus R. J., Mavrogenes J. A., Dyriw N. J., Nebel O. and Hauri E. H. (2012). Chalcophile element systematics in volcanic glasses from the northwestern Lau Basin. *Geochemistry, Geophysics, Geosystems*, **13**(6), Q06014. <https://doi.org/10.1029/2012gc004088>
- Jenner F. E., Hauri E. H., Bullock E. S., König S., Arculus R. J., Mavrogenes J. A., Mikkelsen N. and Goddard C. (2015). The competing effects of sulfide saturation versus degassing on the behavior of the chalcophile elements during the differentiation of hydrous melts. *Geochemistry, Geophysics, Geosystems*, **16**(5), 1490-1507. <https://doi.org/10.1002/2014gc005670>
- Jenner F. E. and O'Neill H. S. (2012). Analysis of 60 elements in 616 ocean floor basaltic glasses. *Geochemistry, Geophysics, Geosystems*, **13**, Q02005. <https://doi.org/10.1029/2011GC004009>
- Jenner F. E., O'Neill H. S. C., Arculus R. J. and Mavrogenes J. A. (2010). The Magnetite Crisis in the Evolution of Arc-related Magmas and the Initial Concentration of Au, Ag and Cu. *Journal of Petrology*, **51**(12), 2445-2464. <https://doi.org/10.1093/petrology/egq063>
- Katz R. F., Spiegelman M. and Langmuir C. H. (2003). A new parameterization of hydrous mantle melting. *Geochemistry, Geophysics, Geosystems*, **4**(9). <https://doi.org/10.1029/2002gc000433>
- Kelley K. A., Plank T., Grove T. L., Stolper E. M., Newman S. and Hauri E. (2006). Mantle melting as a function of water content beneath back-arc basins. *Journal of Geophysical Research*, **111**(B9). <https://doi.org/10.1029/2005jb003732>
- Kimura J.-I., Gill J. B., van Keken P. E., Kawabata H. and Skora S. (2017). Origin of geochemical mantle components: Role of spreading ridges and thermal evolution of mantle. *Geochemistry, Geophysics, Geosystems*, **18**(2), 697-734. <https://doi.org/10.1002/2016gc006696>
- Kiseeva E. S., Fonseca R. O. C. and Smythe D. J. (2017). Chalcophile Elements and Sulfides in the Upper Mantle. *Elements*, **13**(2), 111-116. <https://doi.org/10.2113/gselements.13.2.111>
- Kiseeva E. S. and Wood B. J. (2013). A simple model for chalcophile element partitioning between sulphide and silicate liquids with geochemical applications. *Earth and Planetary Science Letters*, **383**, 68-81. <https://doi.org/10.1016/j.epsl.2013.09.034>
- Kiseeva E. S. and Wood B. J. (2015). The effects of composition and temperature on chalcophile and lithophile element partitioning into magmatic sulphides. *Earth and Planetary Science Letters*, **424**, 280-294. <https://doi.org/10.1016/j.epsl.2015.05.012>
- Klein E. M. and Langmuir C. H. (1987). Global Correlations of Ocean Ridge Basalt Chemistry with Axial Depth and Crustal Thickness. *Journal of Geophysical Research-Solid Earth and Planets*, **92**(B8), 8089-8115. [https://doi.org/DOI 10.1029/JB092iB08p08089](https://doi.org/DOI%2010.1029/JB092iB08p08089)
- Labidi J. and Cartigny P. (2016). Negligible sulfur isotope fractionation during partial melting: Evidence from Garrett transform fault basalts, implications for the late-veener and the hadean matte. *Earth and Planetary Science Letters*, **451**, 196-207. <https://doi.org/10.1016/j.epsl.2016.07.012>
- Labidi J., Cartigny P., Hamelin C., Moreira M. and Dosso L. (2014). Sulfur isotope budget (³²S, ³³S, ³⁴S and ³⁶S) in Pacific–Antarctic ridge basalts: A record of mantle source heterogeneity and hydrothermal sulfide assimilation. *Geochimica et Cosmochimica Acta*, **133**, 47-67. <https://doi.org/10.1016/j.gca.2014.02.023>
- Langmuir C. H. and Forsyth D. W. (2007). Mantle Melting Beneath Mid-Ocean Ridges. *Oceanography*, **20**(1), 78-89. <https://doi.org/10.5670/oceanog.2007.82>
- Langmuir C. H., Klein E. M. and Plank T., 1992. Petrological Systematics of Mid-Ocean Ridge Basalts: Constraints on Melt Generation Beneath Ocean Ridges. In: Morgan J. P., Blackman D. K., and Sinton J. M. (Eds.), *Mantle Flow and Melt Generation at Mid-Ocean Ridges, Geophysical Monograph Series*. American Geophysical Union,

- Washington, D. C., 183-280. <https://doi.org/10.1029/GM071p0183>
- Lee C. T. A., Luffi P., Plank T., Dalton H. and Leeman W. P. (2009). Constraints on the depths and temperatures of basaltic magma generation on Earth and other terrestrial planets using new thermobarometers for mafic magmas. *Earth and Planetary Science Letters*, **279**(1-2), 20-33. <https://doi.org/10.1016/j.epsl.2008.12.020>
- Li Y. and Audétat A. (2012). Partitioning of V, Mn, Co, Ni, Cu, Zn, As, Mo, Ag, Sn, Sb, W, Au, Pb, and Bi between sulfide phases and hydrous basanite melt at upper mantle conditions. *Earth and Planetary Science Letters*, **355**, 327-340. <https://doi.org/10.1016/j.epsl.2012.08.008>
- Lin J. and Morgan J. P. (1992). The spreading rate dependence of three-dimensional mid-ocean ridge gravity structure. *Geophysical Research Letters*, **19**(1), 13-16. <https://doi.org/10.1029/91gl03041>
- Lissner M., König S., Luguët A., le Roux P. J., Schuth S., Heuser A. and le Roex A. P. (2014). Selenium and tellurium systematics in MORBs from the southern Mid-Atlantic Ridge (47–50°S). *Geochimica et Cosmochimica Acta*, **144**, 379-402. <https://doi.org/10.1016/j.gca.2014.08.023>
- Lorand J. P., Luguët A. and Alard O. (2013). Platinum-group element systematics and petrogenetic processing of the continental upper mantle: A review. *Lithos*, **164**, 2-21. <https://doi.org/10.1016/j.lithos.2012.08.017>
- Lorand J.-P. and Luguët A. (2016). Chalcophile and Siderophile Elements in Mantle Rocks: Trace Elements Controlled By Trace Minerals. *Reviews in Mineralogy and Geochemistry*, **81**(1), 441-488. <https://doi.org/10.2138/rmg.2016.81.08>
- Luguët A., Lorand J. P. and Seyler M. (2003). Sulfide petrology and highly siderophile element geochemistry of abyssal peridotites: A coupled study of samples from the Kane Fracture Zone (45 degrees W 23 degrees 20N, MARK Area, Atlantic Ocean). *Geochimica et Cosmochimica Acta*, **67**(8), 1553-1570. [https://doi.org/10.1016/S0016-7037\(02\)01133-X](https://doi.org/10.1016/S0016-7037(02)01133-X)
- McDonough W. F. and Sun S.-S. (1995). The Composition of the Earth. *Chemical Geology*, **120**(3-4), 223-253. [https://doi.org/10.1016/0009-2541\(94\)00140-4](https://doi.org/10.1016/0009-2541(94)00140-4)
- Mungall J. E. and Brenan J. M. (2014). Partitioning of platinum-group elements and Au between sulfide liquid and basalt and the origins of mantle-crust fractionation of the chalcophile elements. *Geochimica et Cosmochimica Acta*, **125**, 265-289. <https://doi.org/10.1016/j.gca.2013.10.002>
- Nielsen R. L., Forsythe L. M., Gallahan W. E. and Fisk M. R. (1994). Major- and trace-element magnetite-melt equilibria. *Chemical Geology*, **117**(1-4), 167-191. [https://doi.org/10.1016/0009-2541\(94\)90127-9](https://doi.org/10.1016/0009-2541(94)90127-9)
- Nielsen S. G., Shimizu N., Lee C.-T. A. and Behn M. D. (2014). Chalcophile behavior of thallium during MORB melting and implications for the sulfur content of the mantle. *Geochemistry, Geophysics, Geosystems*, **15**(12), 4905-4919. <https://doi.org/10.1002/2014gc005536>
- Palme H. and O'Neill H. S. C., 2014. Cosmochemical estimates of Mantle Composition. In: Holland H. D. and Turekian K. K. (Eds.), *Treatise on Geochemistry (Second Edition)*. Elsevier, Oxford, 1-39. <https://doi.org/10.1016/B978-0-08-095975-7.00201-1>
- Patten C., Barnes S. J., Mathez E. A. and Jenner F. E. (2013). Partition coefficients of chalcophile elements between sulfide and silicate melts and the early crystallization history of sulfide liquid: LA-ICP-MS analysis of MORB sulfide droplets. *Chemical Geology*, **358**, 170-188. <https://doi.org/10.1016/j.chemgeo.2013.08.040>
- Peach C. L., Mathez E. A. and Keays R. R. (1990). Sulfide melt-silicate melt distribution coefficients for noble metals and other chalcophile elements as deduced from MORB: Implications for partial melting. *Geochimica et Cosmochimica Acta*, **54**(12), 3379-3389. [https://doi.org/10.1016/0016-7037\(90\)90292-S](https://doi.org/10.1016/0016-7037(90)90292-S)
- Perfit M. R., 2001. Mid-Ocean Ridge Geochemistry and Petrology. In: Steele J. H. (Ed.), *Encyclopedia of Ocean Sciences (Second Edition)*. Academic Press, Oxford, 815-825. <https://doi.org/10.1016/b978-012374473-9.00096-5>
- Plank T., Spiegelman M., Langmuir C. H. and Forsyth D. W. (1995). The meaning of “mean F ”: Clarifying the mean extent of melting at ocean ridges. *Journal of Geophysical Research*, **100**(B8), 15045-15052. <https://doi.org/10.1029/95jb01148>
- Rehkämper M., Halliday A. N., Fitton J. G., Lee D. C., Wieneke M. and Arndt N. T. (1999). Ir, Ru, Pt, and Pd in basalts and komatiites: New constraints for the geochemical behavior of the platinum-group elements in the mantle. *Geochimica et Cosmochimica Acta*, **63**(22), 3915-3934. [https://doi.org/10.1016/S0016-7037\(99\)00219-7](https://doi.org/10.1016/S0016-7037(99)00219-7)
- Righter K., Leeman W. P. and Hervig R. L. (2006). Partitioning of Ni, Co and V between spinel-structured oxides and silicate melts: Importance of spinel composition. *Chemical Geology*, **227**(1-2), 1-25.

<https://doi.org/10.1016/j.chemgeo.2005.05.011>

- Salters V. J. M. and Stracke A. (2004). Composition of the depleted mantle. *Geochemistry, Geophysics, Geosystems*, **5**(5), Q05B07. <https://doi.org/10.1029/2003gc000597>
- Shaw D. M. (1970). Trace element fractionation during anatexis. *Geochimica et Cosmochimica Acta*, **34**(2), 237-243. [https://doi.org/10.1016/0016-7037\(70\)90009-8](https://doi.org/10.1016/0016-7037(70)90009-8)
- Sinton J. M. and Detrick R. S. (1992). Mid-ocean ridge magma chambers. *Journal of Geophysical Research*, **97**(B1), 197-216. <https://doi.org/10.1029/91jb02508>
- Smith P. M. and Asimow P. D. (2005). Adibat_1ph: A new public front-end to the MELTS, pMELTS, and pHMELTS models. *Geochemistry, Geophysics, Geosystems*, **6**(2), Q02004. <https://doi.org/10.1029/2004gc000816>
- Smythe D. J., Wood B. J. and Kiseeva E. S. (2017). The S content of silicate melts at sulfide saturation: New experiments and a model incorporating the effects of sulfide composition. *American Mineralogist*, **102**(4), 795-803. <https://doi.org/10.2138/am-2017-5800CCBY>
- Toplis M. J. and Corgne A. (2002). An experimental study of element partitioning between magnetite, clinopyroxene and iron-bearing silicate liquids with particular emphasis on vanadium. *Contributions to Mineralogy and Petrology*, **144**(1), 22-37. <https://doi.org/10.1007/s00410-002-0382-5>
- Vlastélic I., Dosso L., Bougault H., Aslanian D., Géli L., Etoubleau J., Bohn M., Joron J.-L. and Bollinger C. (2000). Chemical systematics of an intermediate spreading ridge: The Pacific-Antarctic Ridge between 56°S and 66°S. *Journal of Geophysical Research*, **105**(B2), 2915-2936. <https://doi.org/10.1029/1999jb900234>
- Wang Z. and Becker H. (2015b). Abundances of Ag and Cu in mantle peridotites and the implications for the behavior of chalcophile elements in the mantle. *Geochimica et Cosmochimica Acta*, **160**, 209-226. <https://doi.org/10.1016/j.gca.2015.04.006>
- Workman R. K. and Hart S. R. (2005). Major and trace element composition of the depleted MORB mantle (DMM). *Earth and Planetary Science Letters*, **231**(1-2), 53-72. <https://doi.org/10.1016/j.epsl.2004.12.005>
- Zhang H. L., Cottrell E., Solheid P. A., Kelley K. A. and Hirschmann M. M. (2018). Determination of Fe³⁺ /ΣFe of XANES basaltic glass standards by Mössbauer spectroscopy and its application to the oxidation state of iron in MORB. *Chemical Geology*, **479**, 166-175. <https://doi.org/10.1016/j.chemgeo.2018.01.006>
- Zhang Z. and Hirschmann M. M. (2016). Experimental constraints on mantle sulfide melting up to 8 GPa. *American Mineralogist*, **101**(1-2), 181-192. <https://doi.org/10.2138/am-2016-5308>
- Zhang Z., von der Handt A. and Hirschmann M. M. (2018). An experimental study of Fe–Ni exchange between sulfide melt and olivine at upper mantle conditions: implications for mantle sulfide compositions and phase equilibria. *Contributions to Mineralogy and Petrology*, **173**(3), 19. <https://doi.org/10.1007/s00410-018-1444-7>

Supplementary Table Captions

Table. S1 Selenium isotope analysis of MH-495 (inter-laboratory standard solution; 30 ng mL⁻¹ Se) during the course of this study.

Table. S2 Compilation of trace element concentrations analyzed in this study (solution iQAP-Qc quadrupole ICP-MS) together with the major/trace element and radiogenic/stable isotope composition in the literature for the studied PAR glasses.

Table. S3 Trace element concentrations of BHVO-2 (USGS reference material) analyzed in this study as a quality control standard.

Supplementary Figure Captions

Fig. S1. Map showing the location of the studied MORB samples from the Pacific–Antarctic ridge (PAR; 65–56°S (n = 10) and 53–41°S (n = 17)). Also shown are the major fracture zones in the southern and northern ridge sections (Vlastélic et al., 2000; Hamelin et al., 2010). The map is generated using the GeoMapApp (<http://www.geomapapp.org>; and references therein).

Fig. S2. Primitive mantle-normalized (McDonough and Sun, 1995) trace element diagram of the studied PAR MORBs. The element order (with increasing compatibility to the right) is after Hofmann (1988) and Jenner et al. (2012). All samples show typical depleted MORB patterns similar to that of the average N-MORB from Gale et al. (2013). Three most evolved samples (blue line) that have experienced magnetite saturation and magnetite-triggered sulfide precipitation (Fig. S3; Main Text Fig. 4 and 6) display abrupt drops in apparently compatible elements Zn, Ga, Ti, V, Sc, and Co due to their strong partitioning into fractionating magnetite and/or sulfide (Nielsen et al., 1994; Toplis and Corgne, 2002; Righter et al., 2006; Dare et al., 2012, 2014; Labidi et al., 2014; Jenner et al., 2010, 2012, 2015).

Fig. S3. Major element variation diagrams versus MgO for all the PAR on-axis samples (between 65–56°S and 53–41°S; Electronic Annex 2 Table S1) as well as the modelled liquid lines of descents (LLDs). The TiO₂ data (a) for the studied glasses are obtained in this study together with other trace elements. All other data along the studied ridge segments are reported by Vlastélic et al. (2000) and Hamelin et al. (2010). The differentiation trends (isobaric fractional crystallization) are modelled with alphaMELTS front end (V 1.8; Ghiorso and Sack, 1995; Smith and Asimow, 2005) along a buffered fO_2 of 0.18 log units below the FMQ buffer (Zhang H. L. et al., 2018) at a variety of pressures (2, 3, 4, 5 and 7 kbar), starting from the most primitive glass PAC1 DR12-1g (8.85 wt.% MgO). Each tick mark indicates 10% crystal fractionation step. Before the magnetite saturation at ~5 wt.% MgO (Vlastélic et al., 2000; Hamelin et al., 2010; Labidi et al., 2014), most major element variations broadly follow the modelled LLDs at 2–5 kbar. The variation of FeO_T is best reproduced at 3 kbar, and the resulting parameters are used in the subsequent modelling in Main Text Fig. 6.

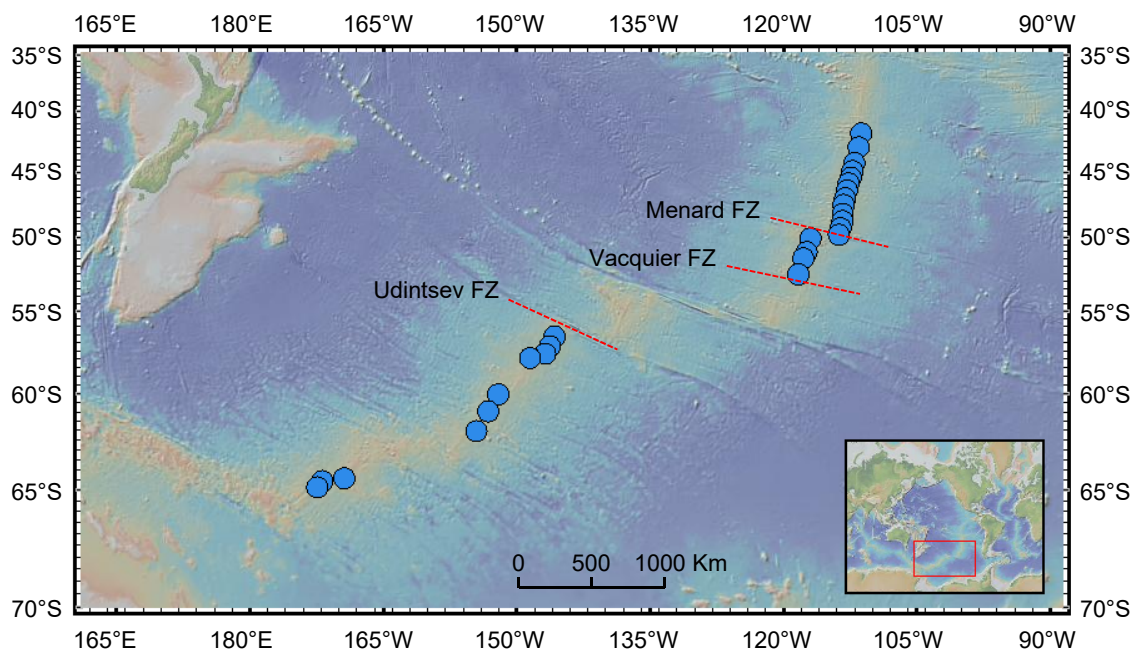
Fig. S4. Primitive mantle-normalized (McDonough and Sun, 1995) incompatible trace element pattern for the model PAR primary magmas (n = 24; at Mg# = 0.73) which were obtained after correcting the observed concentrations for fractional crystallization (see the text for details). Three samples (MgO <5 wt.%) that have experienced magnetite saturation were not included (Fig. S2 and S3 and Main Text Fig. 4). The curves show the best-matched primary melt composition obtained from (1) simple batch melting using average F_B (~8.5%) of the samples, which was first obtained by solving the batch melting equation for F_B for each sample (Eq. 5; following the approach of Kelley et al. (2006)) and (2) pMELTS (near-fractional melting) for the aggregate melts over the entire triangular melting region (F_B : 6.5, 8.0, and 9.5%). The source trace element compositions and empirical bulk partition coefficients were taken from Salters and Stracke (2004) and Kelley et al. (2006),

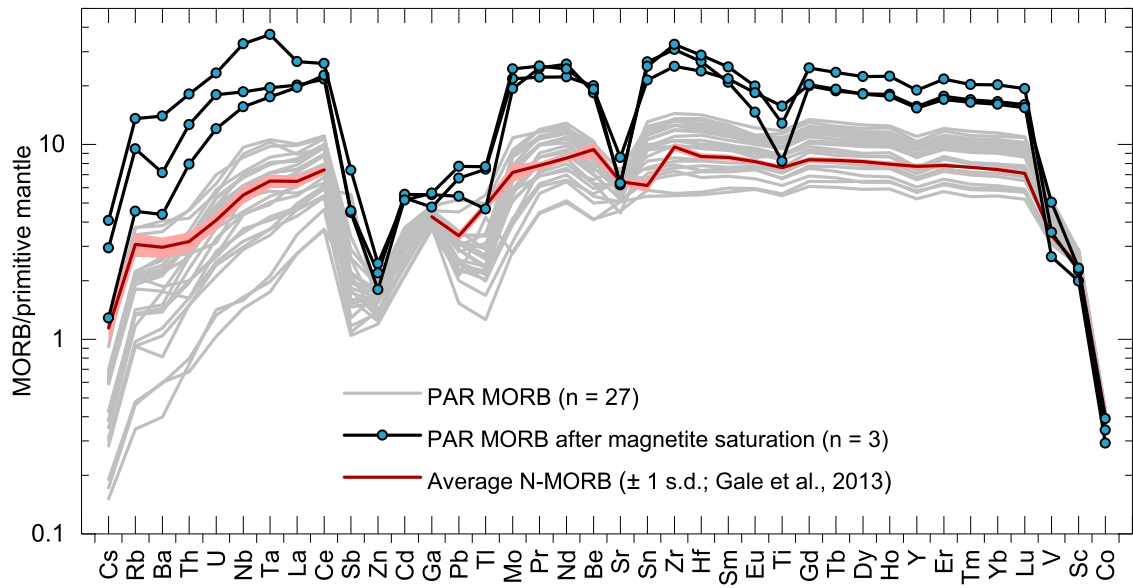
respectively. Both results are in excellent agreement with each other and used for modelling the Se–Te (additionally S–Cu) behavior during partial melting (Fig. S5 and 6; Main Text Fig. 8).

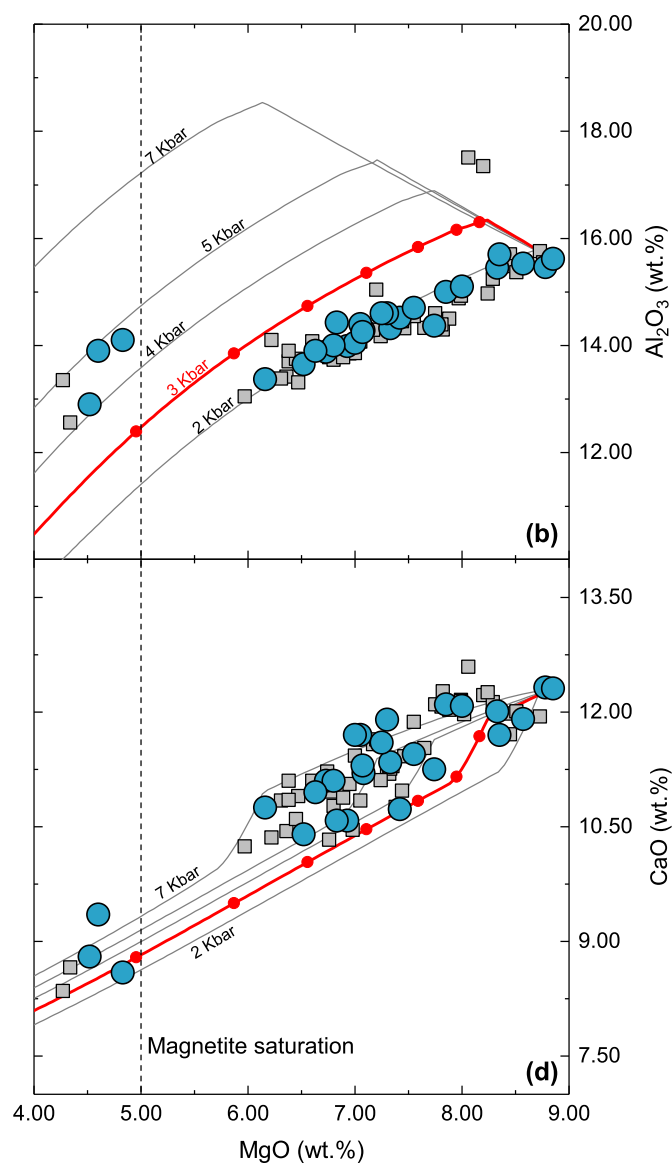
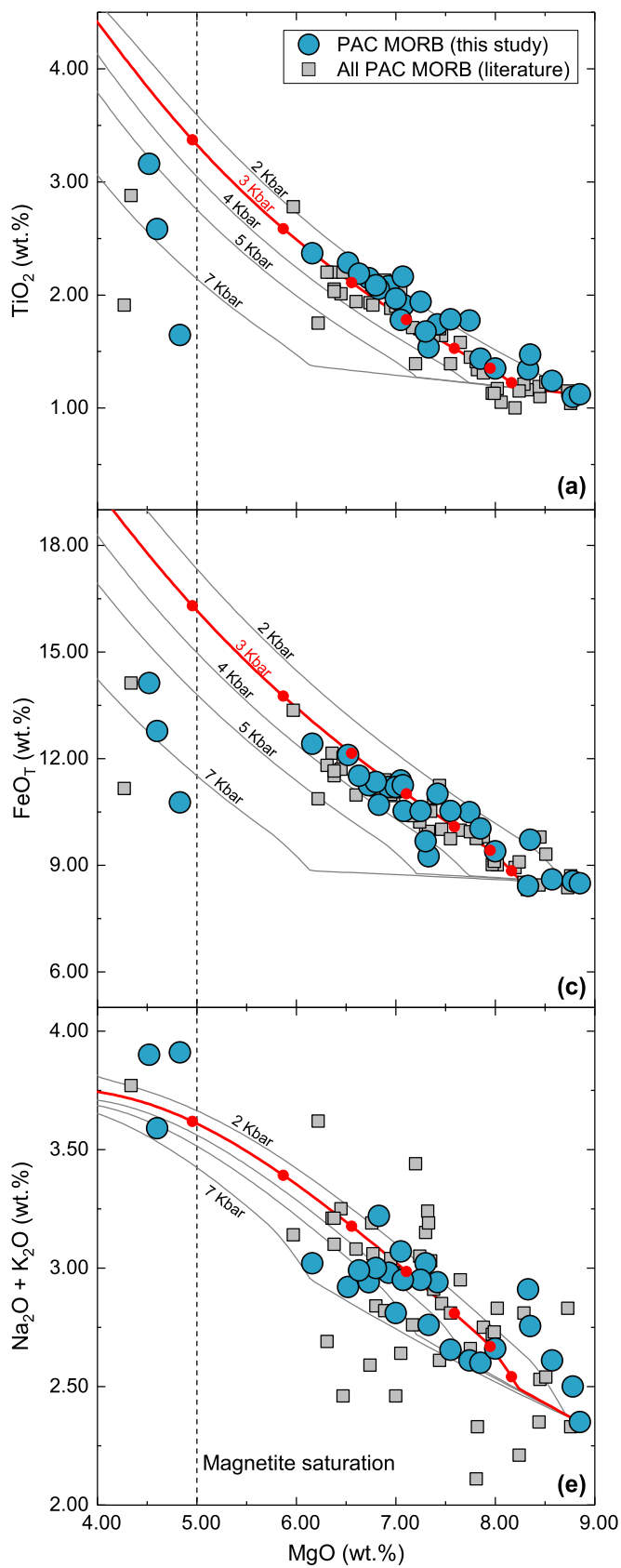
Fig. S5. Variations of S (a) and Cu (b) concentrations of the primary PAR melts with their average degree of melting (F_B ; estimated by batch melting equation Eq. 5 using incompatible trace element systematics; ~6.6–11.7%). The S and Cu concentrations were corrected for sulfide + crystal fractionation by the same approach used for Se and Te concentrations (see Main Text Section 5.2.2 for details). The vertical and horizontal shaded field represent the range of F_B (6.5–9.5%; estimated from the forward modelling (near-fractional melting; pMLETS); also see Fig. S4) and average primary melt composition ($874 \pm 48 \mu\text{g g}^{-1}$ S and $68 \pm 5 \mu\text{g g}^{-1}$ Cu), respectively. Superimposed are modelled S and Cu contents of the primary melt during a near-fractional melting of a depleted MORB mantle in a triangular melting regime (e.g., Rehkämper et al., 1999; Lissner et al., 2014; Brenan, 2015). The major element concentrations, mineral modes, and P–T parameters were obtained from the pMELTS modelling (see Main Text Fig. 7) and used for calculating the SCSS of the silicate melts (Smythe et al., 2017) and D_{Cu}^{bulk} . Three different equilibrium BMS compositions were used to calculate the SCSS (Smythe et al., 2017) of the partial melts (see Section S2 for details). A range of source S contents ($150\text{--}200 \mu\text{g g}^{-1}$) are used for the PAR MORB source mantle according to previous estimates for the primitive and depleted upper mantle (e.g., Lugué et al., 2003; Lorand et al., 2013; Lorand and Lugué, 2016; Bézous et al., 2005; Wang and Becker, 2013; Nielsen et al., 2014; Palme and O'Neill, 2014). The source Cu concentration used here ($30 \pm 6 \mu\text{g g}^{-1}$) has been suggested for both the PM (Wang and Becker, 2015b) and depleted MORB mantle (Salters and Stracke, 2004). $D_{Cu}^{crist-sil}$ (silicate minerals include olivine, orthopyroxene, clinopyroxene, and spinel) from Lee et al. (2009) and $D_{Cu}^{sulf liq-sil} = 1000$ from Li and Audétat (2012). The $D_{Cu}^{sulf liq-sil}$ value was used by Ding and Dasgupta (2017) and Wang and Becker (2015) for modelling the behavior of Cu during melting. It shows that our modelled S variation using the SCSS model of Smythe et al. (2017) combined with equilibrium sulfide B ($X_{Fe} = 0.54$; $\frac{Ni}{Ni+Fe} = 0.42$) successfully reproduces the primary melt S contents with $150\text{--}200 \mu\text{g g}^{-1}$ S in the mantle source (a); meanwhile, the model curves also perfectly match the Cu contents with $170\text{--}200 \mu\text{g g}^{-1}$ S (b and c; also see the light yellow shaded area in c). Additionally shown in (b) and (c) is the modelled Cu content with $24 \mu\text{g g}^{-1}$ Cu (previously used in the model of Ding and Dasgupta (2017)) and $180 \mu\text{g g}^{-1}$ S (dashed black line), in accordance with the source S content used for modelling the Se–Te variation during melting shown in Fig. S6 and Main Text Fig. 8 and 9.

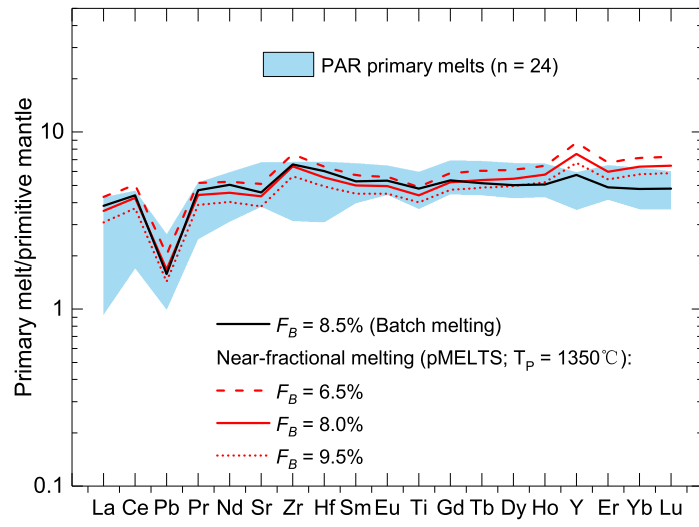
Fig. S6. Variations of Se (a) and Te (b) contents and Se/Te ratios (c) of the primary PAR melts with their average degree of melting (F_B). Here, it shows the effect of varying proportions of sulfide phases (i.e., sulfide liquid and crystalline MSS; assuming congruent melting) in the source with $180 \mu\text{g g}^{-1}$ S. See Main Text Fig. 8 for details of the modelling parameters when the source has only sulfide liquid (e.g., different S–Se–Te contents of the mantle source). The grey shaded areas have the same meaning as in Main Text Fig. 8. $D_{Se or Te}^{sulf liq-sil}$ values are either calculated following Brenan (2015) at each incremental melt (black lines) or taken from Kiseeva et al. (2017)

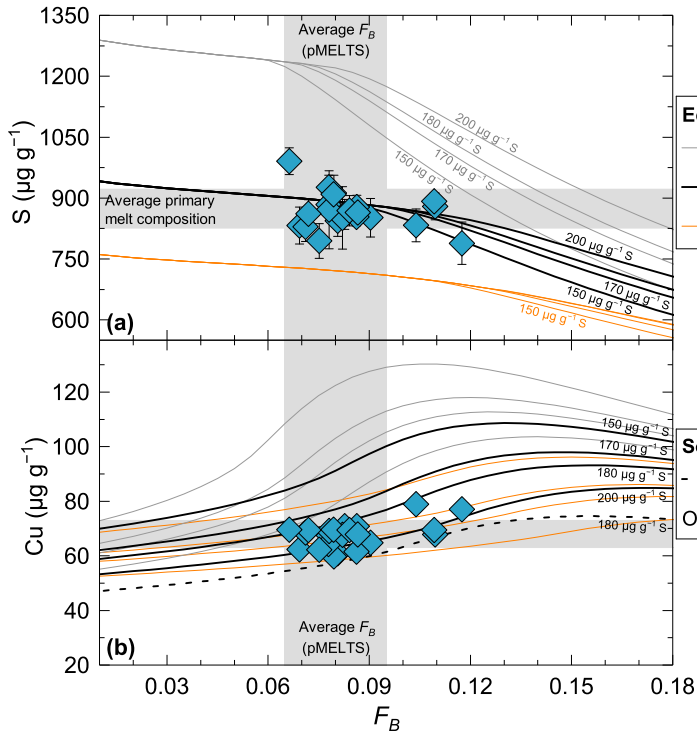
(red lines; $D_{Se}^{sulf\ liq-sil} = 850$ and $D_{Te}^{sulf\ liq-sil} = 3800$) considering the FeO content of the melt increments (also see Section S1 for the difference of $D_{Se\ or\ Te}^{sulf\ liq-sil}$ values between these studies). $D_{Se}^{MSS-sil} = 883$ and $D_{Te}^{MSS-sil} = 729$ (both constant) from Brenan (2015). It shows that the Se–Te fractionation during entire F_B interval is limited if MSS is the only residual sulfide due to the similar $D_{Se\ or\ Te}^{MSS-sil}$ values (also see Main Text Fig. 9; Brenan, 2015). Sulfide liquid is required to be the dominant (>50%), if not only, residual sulfide phase in order to account for the observed Se–Te variations of the primary MORB melts based on the relative partitioning of these elements in sulfide liquid and crystalline MSS (see Main Text for discussion).











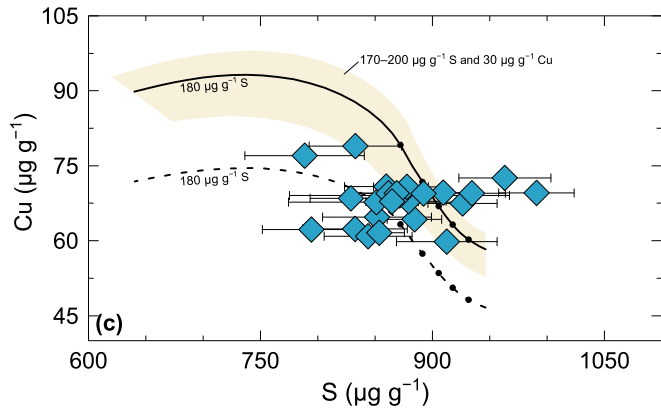
Equilibrium mantle sulfide:

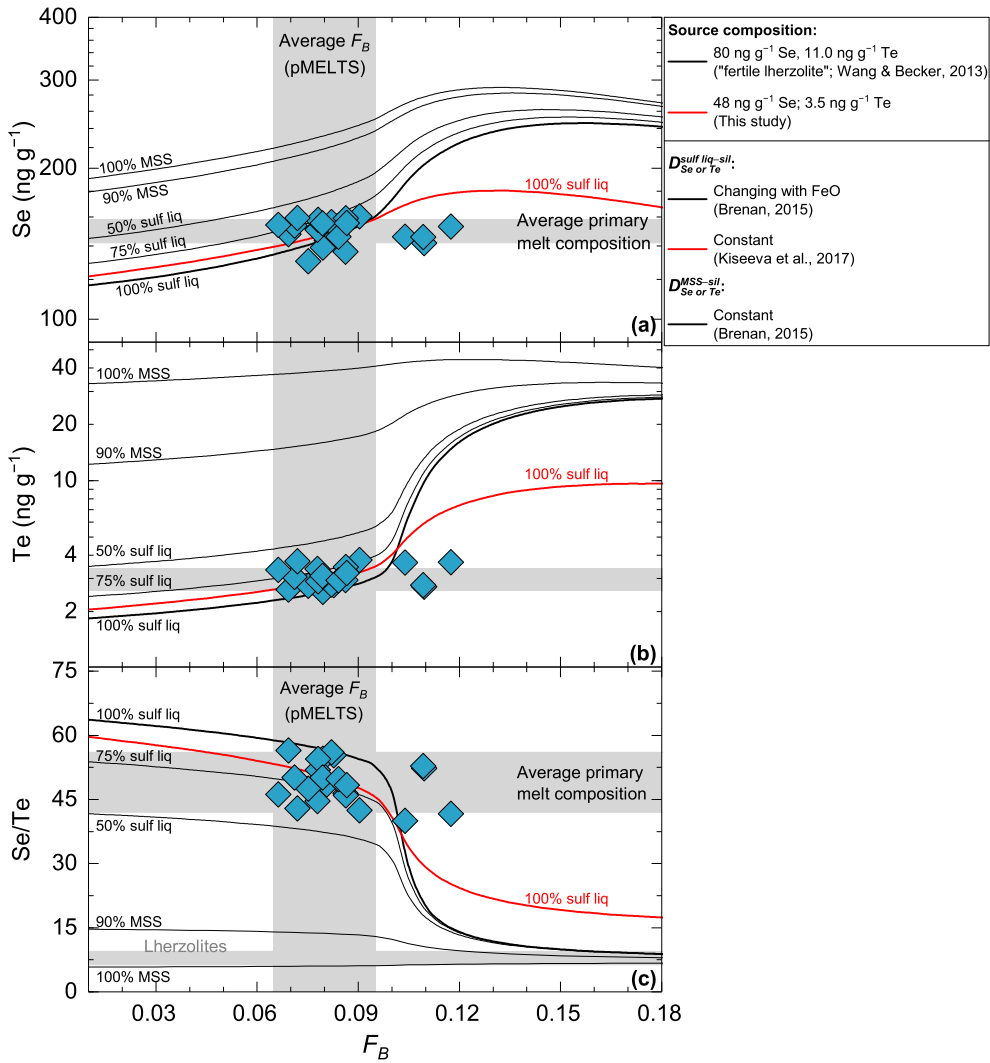
- A ($\text{Fe}_{0.69}\text{Ni}_{0.23}\text{Cu}_{0.01}\text{S}_{1.00}$)
- B ($\text{Fe}_{0.50}\text{Ni}_{0.36}\text{Cu}_{0.07}\text{S}_{1.00}$)
- C ($\text{Fe}_{0.41}\text{Ni}_{0.46}\text{Cu}_{0.07}\text{S}_{1.00}$)

Increasing $X_{\text{Ni}}/(X_{\text{Ni}} + X_{\text{Fe}})$
 Decreasing X_{Fe}
 Decreasing SCSS

Source Cu content:

- - - 24 $\mu\text{g g}^{-1}$ } Salters & Stracke (2004)
- - - Others: 30 $\mu\text{g g}^{-1}$ } Wang & Becker (2015b)





Supplementary Table S1
Selenium isotope analysis of MH-495 (inter-laboratory standard solution; 30 ng mL⁻¹ Se) during the course of this study.

$\delta^{82/76}\text{Se}$ (‰)	2 s.e. (‰) ^a
-3.20	0.04
-3.19	0.05
-3.27	0.05
-3.24	0.04
-3.22	0.06
-3.28	0.05
-3.26	0.05
-3.21	0.05
-3.17	0.07
-3.24	0.05
-3.24	0.05
-3.29	0.04
-3.25	0.06
-3.28	0.05
-3.25	0.06
-3.28	0.04
-3.17	0.05
-3.28	0.05
-3.24	0.05
-3.23	0.05
Average^b	-3.24 ± 0.07
Kurzawa et al. (2017) ^b	-3.27 ± 0.13 (n = 100) (15 ng mL ⁻¹ Se)
Yierpan et al. (2018) ^b	-3.24 ± 0.10 (n = 46) (15 ng mL ⁻¹ Se)
	-3.26 ± 0.06 (n = 32) (30 ng mL ⁻¹ Se)

^a Internal uncertainty of each individual measurement (40 cycles) given in 2 standard error.

^b Uncertainty on the average given in 2 standard deviation.

References:

Kurzawa T., König S., Labidi J., Yierpan A. and Schoenberg R. (2017). A method for Se isotope analysis of low ng-level geological samples via double spike and hydride generation MC-ICP-MS. *Chemical Geology*, **466**, 219-228.
Yierpan A., König S., Labidi J., Kurzawa T., Babelchuk M. G. and Schoenberg R. (2018). Chemical Sample Processing for Combined Selenium Isotope and Selenium-Tellurium Elemental Investigation of the Earth's Igneous Reservoirs. *Geochemistry, Geophysics, Geosystems*, **19**, 516-533.

Supplementary Table S2

Compilation of trace element concentrations analyzed in this study (solution iQAP-Qc quadrupole ICP-MS) together with the

Sample	Latitude (°S)	Longitude (°W)	Dredging Depth (m)	Major elements ^a (wt. %)	SiO ₂	TiO ₂	Al ₂ O ₃	FeO _T	MnO	MgO	CaO
PAC1 CV02-g	<i>64.83</i>	<i>172.43</i>	<i>2936</i>		<i>50.8</i>	<i>1.77</i>	<i>14.4</i>	<i>10.5</i>	<i>0.19</i>	<i>7.74</i>	<i>11.3</i>
PAC1 CV03-g	<i>64.53</i>	<i>171.88</i>	<i>2576</i>		<i>50.7</i>	<i>1.24</i>	<i>15.5</i>	<i>8.60</i>	<i>0.16</i>	<i>8.57</i>	<i>11.9</i>
PAC1 CV04-g	<i>64.40</i>	<i>169.40</i>	<i>2340</i>		<i>50.3</i>	<i>1.10</i>	<i>15.5</i>	<i>8.55</i>	<i>0.16</i>	<i>8.78</i>	<i>12.3</i>
PAC1 DR05-1g	<i>62.00</i>	<i>154.54</i>	<i>2344</i>		<i>51.0</i>	<i>1.34</i>	<i>15.5</i>	<i>8.42</i>	<i>0.15</i>	<i>8.33</i>	<i>12.0</i>
PAC1 DR06-g	<i>60.94</i>	<i>153.21</i>	<i>2527</i>		<i>51.0</i>	<i>2.08</i>	<i>14.0</i>	<i>11.2</i>	<i>0.20</i>	<i>6.93</i>	<i>10.6</i>
PAC1 DR07-1g	<i>60.00</i>	<i>152.08</i>	<i>2362</i>		<i>50.8</i>	<i>2.05</i>	<i>14.4</i>	<i>10.7</i>	<i>0.22</i>	<i>6.83</i>	<i>10.6</i>
PAC1 DR10-1g	<i>57.89</i>	<i>148.50</i>	<i>2319</i>		<i>53.8</i>	<i>1.65</i>	<i>14.1</i>	<i>10.8</i>	<i>0.21</i>	<i>4.83</i>	<i>8.59</i>
PAC1 DR11-1g	<i>57.63</i>	<i>146.80</i>	<i>2500</i>		<i>50.2</i>	<i>1.53</i>	<i>14.3</i>	<i>9.25</i>	<i>0.17</i>	<i>7.33</i>	<i>11.3</i>
PAC1 DR12-1g	<i>57.18</i>	<i>146.29</i>	<i>2539</i>		<i>50.9</i>	<i>1.12</i>	<i>15.6</i>	<i>8.49</i>	<i>0.15</i>	<i>8.85</i>	<i>12.3</i>
PAC1 DR13-2g	<i>56.57</i>	<i>145.74</i>	<i>2674</i>		<i>50.5</i>	<i>1.74</i>	<i>14.5</i>	<i>11.0</i>	<i>0.19</i>	<i>7.42</i>	<i>10.7</i>
PAC2 DR01-1	<i>52.53</i>	<i>118.35</i>	<i>2323</i>		<i>50.2</i>	<i>1.68</i>	<i>14.6</i>	<i>9.67</i>	<i>0.18</i>	<i>7.30</i>	<i>11.9</i>
PAC2 DR04-2	<i>51.43</i>	<i>117.78</i>	<i>2409</i>		<i>50.4</i>	<i>1.91</i>	<i>14.3</i>	<i>10.5</i>	<i>0.20</i>	<i>7.08</i>	<i>11.2</i>
PAC2 DR05-2g	<i>50.98</i>	<i>117.40</i>	<i>2784</i>		<i>49.9</i>	<i>2.28</i>	<i>13.7</i>	<i>12.1</i>	<i>0.22</i>	<i>6.52</i>	<i>10.4</i>
PAC2 DR08-1	<i>49.99</i>	<i>116.97</i>	<i>2221</i>		<i>49.4</i>	<i>1.78</i>	<i>14.4</i>	<i>11.4</i>	<i>0.20</i>	<i>7.05</i>	<i>11.7</i>
PAC2 DR20-1	<i>49.73</i>	<i>113.78</i>	<i>2441</i>		<i>51.2</i>	<i>2.58</i>	<i>13.9</i>	<i>12.8</i>	<i>0.24</i>	<i>4.60</i>	<i>9.35</i>
PAC2 DR21-2	<i>49.26</i>	<i>113.60</i>	<i>2339</i>		<i>50.3</i>	<i>2.15</i>	<i>13.9</i>	<i>11.2</i>	<i>0.21</i>	<i>6.73</i>	<i>11.1</i>
PAC2 DR22-1	<i>48.73</i>	<i>113.37</i>	<i>2413</i>		<i>49.9</i>	<i>1.94</i>	<i>14.6</i>	<i>10.5</i>	<i>0.20</i>	<i>7.25</i>	<i>11.6</i>
PAC2 DR27-1	<i>48.18</i>	<i>113.34</i>	<i>2359</i>		<i>49.8</i>	<i>3.16</i>	<i>12.9</i>	<i>14.1</i>	<i>0.26</i>	<i>4.52</i>	<i>8.80</i>
PAC2 DR28-2	<i>47.51</i>	<i>113.25</i>	<i>2489</i>		<i>49.7</i>	<i>1.44</i>	<i>15.0</i>	<i>10.0</i>	<i>0.19</i>	<i>7.85</i>	<i>12.1</i>
PAC2 DR29-1	<i>47.01</i>	<i>113.09</i>	<i>2407</i>		<i>49.9</i>	<i>2.37</i>	<i>13.4</i>	<i>12.4</i>	<i>0.23</i>	<i>6.16</i>	<i>10.8</i>
PAC2 DR30-1	<i>46.40</i>	<i>112.87</i>	<i>2345</i>		<i>50.0</i>	<i>1.97</i>	<i>14.1</i>	<i>11.2</i>	<i>0.21</i>	<i>7.00</i>	<i>11.7</i>
PAC2 DR31-3	<i>45.85</i>	<i>112.69</i>	<i>2414</i>		<i>49.9</i>	<i>1.78</i>	<i>14.7</i>	<i>10.5</i>	<i>0.19</i>	<i>7.55</i>	<i>11.5</i>
PAC2 DR32-1	<i>45.39</i>	<i>112.43</i>	<i>2384</i>		<i>50.5</i>	<i>2.08</i>	<i>14.0</i>	<i>11.3</i>	<i>0.21</i>	<i>6.80</i>	<i>11.1</i>
PAC2 DR33-1	<i>44.87</i>	<i>112.25</i>	<i>2374</i>		<i>50.2</i>	<i>2.19</i>	<i>13.9</i>	<i>11.5</i>	<i>0.21</i>	<i>6.63</i>	<i>11.0</i>
PAC2 DR34-1	<i>44.24</i>	<i>112.04</i>	<i>2467</i>		<i>50.0</i>	<i>1.35</i>	<i>15.1</i>	<i>9.39</i>	<i>0.18</i>	<i>8.00</i>	<i>12.1</i>
PAC2 DR36-1	<i>42.95</i>	<i>111.56</i>	<i>2503</i>		<i>49.6</i>	<i>2.16</i>	<i>14.3</i>	<i>11.2</i>	<i>0.20</i>	<i>7.07</i>	<i>11.3</i>
PAC2 DR38-1	<i>41.80</i>	<i>111.27</i>	<i>2524</i>		<i>49.1</i>	<i>1.47</i>	<i>15.7</i>	<i>9.72</i>	<i>0.18</i>	<i>8.35</i>	<i>11.7</i>

Note: All literature data are shown in italics.

^a From Vlastélic et al. (2000) and Hamelin et al. (2010).

^b Literature trace element data are mostly from Vlastélic et al. (2000) and Hamelin et al. (2010); Cu, S and Cl data from Labidi et al. (2014); Mo data from

^c Uncertainties (Li to U) are estimated using relative standard deviations (r.s.d.) from 14 analyses of 6 BHVO-2 digestions (4 digested together with the I

^d From Labidi et al. (2014).

^e From Vlastélic et al. (2000), Moreira et al. (2008) and Hamelin et al. (2010, 2011).

References:

- Bezard R., Fischer-Gödde M., Hamelin C., Brennecke G. A. and Kleine T. (2016). The effects of magmatic processes and crustal recycling on the molybdenum isotope composition of MORB: A reassessment. *Earth and Planetary Science Letters*, **438**, 1–12.
- Clog M., Aubaud C., Cartigny P. and Dosso L. (2013). The hydrogen isotopic composition and water content of southern Pacific MORB: A reassessment. *Earth and Planetary Science Letters*, **366**, 1–12.
- Hamelin C., Dosso L., Hanan B., Barrat J.-A. and Ondréas H. (2010). Sr-Nd-Hf isotopes along the Pacific Antarctic Ridge from 41 to 53°S. *Geophysical Research Letters*, **37**, L12302.
- Hamelin C., Dosso L., Hanan B. B., Moreira M., Kositsky A. P. and Thomas M. Y. (2011). Geochemical portrait of the Pacific Ridge: New isotopic data. *Earth and Planetary Science Letters*, **308**, 1–12.
- Labidi J., Cartigny P., Hamelin C., Moreira M. and Dosso L. (2014). Sulfur isotope budget (32S, 33S, 34S and 36S) in Pacific–Antarctic ridge basalts: A reassessment. *Earth and Planetary Science Letters*, **388**, 1–12.
- Moreira M. A., Dosso L. and Ondréas H. (2008). Helium isotopes on the Pacific–Antarctic ridge (52.5°–41.5°S). *Geophysical Research Letters*, **35**(10), L10302.
- Vlastélic I., Dosso L., Bougault H., Aslanian D., Géli L., Etoubleau J., Bohn M., Joron J.-L. and Bollinger C. (2000). Chemical systematics of an intermediate to basaltic MORB: The Pacific–Antarctic ridge. *Earth and Planetary Science Letters*, **181**, 1–12.

major/trace element and radiogenic/stable isotope composition in the literature for the studied PAR glasses.

Na ₂ O	K ₂ O	P ₂ O ₅	Trace elements ^b (μg g ⁻¹)	Li	Be	Sc	Ti	V	Cr
			Uncertainty ^c (%)	1	2	1	2	1	1
2.55	0.06			7.02	0.43	42	10632	358	334
2.53	0.08			4.88	0.38	38	7428	261	255
2.46	0.04			4.69	0.28	39	6585	252	251
2.82	0.09			5.29	0.45	42	8041	267	243
2.86	0.12			7.89	0.60	41	12451	375	366
3.03	0.19			6.76	0.69	40	12308	354	344
3.43	0.48			11.63	1.36	32	9863	217	227
2.70	0.06			6.18	0.43	47	9199	333	294
2.32	0.03			5.16	0.28	38	6720	270	248
2.85	0.09			7.03	0.47	41	10433	325	309
2.82	0.20	0.17		5.56	0.50	44	10050	310	
2.83	0.12	0.18		7.39	0.52	43	11451	343	
2.74	0.18	0.24		8.45	0.62	42	13690	391	
2.87	0.20	0.17		6.31	0.53	44	10660	323	
3.34	0.25	0.42		11.16	1.25	36	15485	290	
2.79	0.15	0.18		7.46	0.59	46	12873	375	
2.78	0.17	0.18		6.96	0.57	44	11625	359	
3.37	0.53	0.46		11.40	1.30	38	18926	414	
2.52	0.08	0.12		5.91	0.37	45	8601	308	
2.83	0.19	0.23		8.53	0.71	46	14192	427	
2.64	0.17	0.20		7.19	0.56	45	11799	371	
2.56	0.10	0.18		6.72	0.48	42	10688	351	
2.84	0.16	0.21		7.37	0.63	46	12493	389	
2.84	0.15	0.22		7.70	0.66	46	13113	401	
2.60	0.06	0.12		5.82	0.34	42	8091	294	
2.80	0.15	0.21		7.58	0.64	45	12952	385	
2.67	0.09	0.14		5.54	0.40	40	8824	285	

m Bezard et al. (2016). Ce data for PAC1 samples are from Clog et al. (2011) PAR samples; see Table S2

denum stable isotopic composition of Mid-Ocean Ridge Basalts. Earth and Planetary Science Letters **453**, 171-181.

t of the D/H ratio of the depleted mantle reservoir. Earth and Planetary Science Letters **381**, 156-165.

Research Letters **37**(10).

and statistical techniques. Earth and Planetary Science Letters **302**(1-2), 154-162.

record of mantle source heterogeneity and hydrothermal sulfide assimilation. Geochimica et Cosmochimica Acta **133**, 47-67.

diate spreading ridge: The Pacific-Antarctic Ridge between 56°S and 66°S. Journal of Geophysical Research **1105**(B2), 2915-2936.

Co	Ni	Cu		Zn	Ga	Rb	Sr		Y	
1	1	1		4	1	1	1		1	
44	100	56	57	92	17	0.55	89		38	37
41	123	65	72	68	15	0.81	132		25	24
42	110	70	85	66	15	0.29	101		23	23
42	91	77	85	72	16	1.33	149		26	25
43	77	50	57	100	19	1.09	107		43	42
41	62	61	69	93	18	2.06	145		41	40
31	29	49	68	99	19	5.70	124		67	71
45	75	74	76	85	17	0.70	122		32	29
43	128	70	82	70	15	0.28	91		24	24
45	92	59	64	95	17	1.25	106		37	35
40	67	67	82	74	17	1.20	137	144	32	39
42	73	55	65	86	17	0.81	114	116	38	43
42	63	47	66	104	18	2.24	113	115	45	50
42	60	67	88	85	17	2.23	145	142	33	36
36	30	40	52	120	22	2.72	126	137	82	89
44	54	59	62	94	18	1.25	122	123	41	44
43	79	63	76	85	18	1.15	127	122	39	43
41	21	39	29	135	23	8.15	170	164	66	72
45	86	77	93	77	17	0.55	101	103	30	32
45	48	55	71	108	19	1.34	119	117	47	51
43	74	60	69	90	18	1.20	115	119	40	45
44	98	64	73	85	17	0.80	104	102	37	41
43	63	59	66	95	18	1.29	132	138	40	45
43	57	56	63	97	18	1.24	131	130	42	47
43	105	70	74	75	16	0.21	102	93	28	32
43	72	60	67	94	18	0.85	124	124	43	49
46	124	68	67	75	16	0.58	127	131	29	33

Zr		Nb		Mo		Cd	Sn	Sb	Cs	Ba
2		1		15		1	2	10	1	1
101	105	1.90	2.13	0.20		0.12	1.22	0.009	0.006	5.36
76	77	2.42	2.21	0.19	0.18	0.09	0.88	0.009	0.009	9.49
57	64	1.08	1.03	0.14		0.08	0.70	0.006	0.004	3.92
82	86	3.54	3.43	0.26		0.10	0.97	0.010	0.015	17.46
132	140	3.57	3.65	0.38		0.13	1.53	0.011	0.012	11.65
141	148	5.64	5.77	0.54		0.14	1.61	0.019	0.025	23.53
323	355	12.26	13.62	1.09		0.21	3.45	0.025	0.062	47.21
90	89	2.09	1.93	0.26	0.19	0.11	1.07	0.008	0.007	11.58
59	62	0.95	0.82	0.14		0.08	0.76	0.012	0.004	3.97
102	107	2.86	2.86	0.28	0.26	0.11	1.25	0.007	0.013	12.30
104	112	3.76	3.74	0.33	0.32	0.12	1.13	0.014	0.013	14.54
115	120	2.90	3.13	0.28		0.12	1.27	0.009	0.009	9.27
142	153	6.38	6.83	0.45		0.15	1.53	0.014	0.024	25.32
109	116	5.89	6.03	0.36		0.12	1.30	0.010	0.019	26.74
342	305	10.28	10.70	0.97	0.80	0.22	3.27	0.025	0.027	28.83
131	139	4.60	4.92	0.39		0.13	1.45	0.008	0.012	15.16
124	128	4.05	4.28	0.37	0.46	0.13	1.38	0.011	0.013	13.98
265	279	21.66	22.42	1.22	1.19	0.21	2.79	0.041	0.085	92.44
80	83	1.96	2.36	0.21		0.10	0.92	0.006	0.006	6.87
152	161	4.77	5.12	0.47		0.15	1.70	0.016	0.014	16.79
125	133	4.04	4.40	0.37		0.13	1.38	0.010	0.013	14.64
110	117	2.98	3.15	0.30	0.28	0.11	1.25	0.009	0.008	9.13
132	138	4.52	4.61	0.43		0.14	1.48	0.012	0.014	15.84
139	145	4.44	4.79	0.43		0.14	1.54	0.012	0.013	14.13
73	77	1.05	1.17	0.16		0.09	0.85	0.006	0.003	2.63
140	149	3.87	4.23	0.45	0.39	0.14	1.55	0.011	0.008	9.90
86	91	2.32	2.32	0.29	0.23	0.10	0.99	0.030	0.007	7.52

La		Ce		Pr		Nd		Sm		Eu
1		1		1		1		1		2
3.00	<i>3.01</i>	10.27	<i>10.5</i>	1.88		10.55		3.83	<i>4.03</i>	1.32
2.98	<i>2.88</i>	9.14	<i>8.7</i>	1.55		8.20		2.78	<i>2.83</i>	1.03
1.79	<i>1.97</i>	6.08	<i>6.3</i>	1.12		6.28		2.31	<i>2.51</i>	0.91
3.64	<i>3.77</i>	10.61		1.75		9.20		3.05	<i>3.08</i>	1.15
4.68	<i>4.58</i>	14.65	<i>5.2</i>	2.54		13.66		4.64	<i>4.67</i>	1.58
6.42	<i>6.11</i>	18.08	<i>10.5</i>	2.94		15.09		4.86	<i>5.02</i>	1.64
13.05	<i>14.27</i>	36.30	<i>39.6</i>	5.62		27.84		8.48	<i>9.50</i>	2.25
3.22	<i>3.11</i>	10.30	<i>9.6</i>	1.83		9.95		3.48	<i>3.45</i>	1.27
1.78	<i>1.87</i>	6.17	<i>6.0</i>	1.14		6.42		2.42	<i>2.58</i>	0.91
3.54	<i>3.79</i>	11.42	<i>11.1</i>	2.02		11.10		3.92	<i>3.92</i>	1.39
4.49	<i>4.94</i>	13.29	<i>14.4</i>	2.19	<i>2.22</i>	11.38	<i>12.32</i>	3.78	<i>3.94</i>	1.38
4.16	<i>3.98</i>	13.15	<i>12.8</i>	2.30	<i>2.14</i>	12.34	<i>11.94</i>	4.27	<i>4.13</i>	1.54
6.50	<i>6.37</i>	18.58	<i>17.6</i>	3.02	<i>2.82</i>	15.52	<i>15.10</i>	5.12	<i>4.89</i>	1.72
5.77	<i>5.57</i>	16.05	<i>15.8</i>	2.53	<i>2.41</i>	12.76	<i>12.29</i>	4.00	<i>3.87</i>	1.47
12.72	<i>11.92</i>	38.04	<i>34.2</i>	6.27	<i>5.69</i>	32.38	<i>28.95</i>	10.16	<i>9.29</i>	3.07
5.34	<i>4.64</i>	16.31	<i>14.0</i>	2.78	<i>2.32</i>	14.63	<i>12.61</i>	4.82	<i>4.41</i>	1.71
4.81	<i>4.81</i>	14.84	<i>14.6</i>	2.54	<i>2.41</i>	13.33	<i>12.94</i>	4.46	<i>4.42</i>	1.58
17.27	<i>16.13</i>	43.61	<i>40.3</i>	6.41	<i>5.87</i>	30.53	<i>28.60</i>	8.82	<i>8.49</i>	2.84
2.78	<i>2.77</i>	8.98	<i>8.6</i>	1.59	<i>1.50</i>	8.73	<i>8.40</i>	3.10	<i>3.02</i>	1.19
5.86	<i>5.61</i>	17.94	<i>17.1</i>	3.04	<i>2.79</i>	16.12	<i>14.87</i>	5.33	<i>5.14</i>	1.87
4.84	<i>4.79</i>	14.97	<i>14.9</i>	2.53	<i>2.43</i>	13.45	<i>13.16</i>	4.55	<i>4.51</i>	1.59
3.93	<i>3.91</i>	12.55	<i>12.7</i>	2.19	<i>2.09</i>	11.73	<i>11.46</i>	4.05	<i>4.00</i>	1.43
5.33	<i>5.26</i>	16.21	<i>16.2</i>	2.71	<i>2.68</i>	14.24	<i>14.33</i>	4.72	<i>4.77</i>	1.67
5.48	<i>5.44</i>	16.79	<i>16.2</i>	2.81	<i>2.70</i>	14.70	<i>14.32</i>	4.85	<i>4.83</i>	1.70
2.23	<i>2.27</i>	7.76	<i>8.1</i>	1.42	<i>1.43</i>	8.04	<i>8.24</i>	2.93	<i>3.03</i>	1.14
5.09	<i>5.15</i>	16.13	<i>16.2</i>	2.77	<i>2.75</i>	14.78	<i>14.80</i>	4.97	<i>4.99</i>	1.71
3.07	<i>3.14</i>	9.89	<i>10.2</i>	1.74	<i>1.74</i>	9.44	<i>9.64</i>	3.26	<i>3.34</i>	1.23

	Gd		Tb		Dy		Ho		Er	
	1		1		2		1		1	
	5.54		0.99		6.59		1.47		4.23	
	3.75		0.67		4.31		0.95		2.72	
	3.31		0.60		3.96		0.88		2.51	
	4.10		0.72		4.65		1.02		2.91	
	6.36		1.12		7.37		1.62		4.61	
	6.40		1.13		7.31		1.61		4.57	
	10.87		1.87		12.29		2.70		7.74	
	4.95		0.87		5.84		1.29		3.67	
	3.52		0.64		4.36		0.96		2.77	
	5.68		1.02		6.77		1.52		4.33	
<i>1.56</i>	5.11	<i>5.00</i>	0.90	<i>0.93</i>	5.88	<i>6.22</i>	1.29	<i>1.32</i>	3.70	<i>3.71</i>
<i>1.54</i>	6.02	<i>5.63</i>	1.06	<i>1.03</i>	7.03	<i>6.89</i>	1.56	<i>1.51</i>	4.44	<i>4.33</i>
<i>1.74</i>	7.08	<i>6.57</i>	1.23	<i>1.20</i>	8.15	<i>8.03</i>	1.81	<i>1.76</i>	5.14	<i>5.07</i>
<i>1.38</i>	5.31	<i>5.01</i>	0.93	<i>0.90</i>	6.07	<i>5.96</i>	1.35	<i>1.30</i>	3.81	<i>3.69</i>
<i>2.78</i>	13.46	<i>11.64</i>	2.32	<i>2.11</i>	15.04	<i>14.10</i>	3.34	<i>3.08</i>	9.50	<i>8.82</i>
<i>1.60</i>	6.68	<i>5.73</i>	1.18	<i>1.04</i>	7.65	<i>7.13</i>	1.72	<i>1.57</i>	4.85	<i>4.50</i>
<i>1.55</i>	5.95	<i>5.64</i>	1.05	<i>1.02</i>	6.91	<i>6.81</i>	1.52	<i>1.50</i>	4.32	<i>4.29</i>
<i>2.65</i>	11.06	<i>10.50</i>	1.90	<i>1.82</i>	12.24	<i>11.81</i>	2.63	<i>2.54</i>	7.47	<i>7.23</i>
<i>1.19</i>	4.47	<i>3.97</i>	0.81	<i>0.77</i>	5.43	<i>5.40</i>	1.20	<i>1.13</i>	3.48	<i>3.30</i>
<i>1.78</i>	7.32	<i>6.83</i>	1.29	<i>1.26</i>	8.48	<i>8.26</i>	1.86	<i>1.78</i>	5.29	<i>5.21</i>
<i>1.60</i>	6.16	<i>6.16</i>	1.10	<i>1.11</i>	7.24	<i>7.31</i>	1.60	<i>1.60</i>	4.53	<i>4.62</i>
<i>1.42</i>	5.59	<i>5.38</i>	0.99	<i>0.99</i>	6.58	<i>6.65</i>	1.45	<i>1.43</i>	4.13	<i>4.20</i>
<i>1.70</i>	6.30	<i>6.19</i>	1.12	<i>1.13</i>	7.30	<i>7.52</i>	1.61	<i>1.59</i>	4.54	<i>4.58</i>
<i>1.70</i>	6.49	<i>6.21</i>	1.15	<i>1.13</i>	7.50	<i>7.59</i>	1.66	<i>1.64</i>	4.70	<i>4.85</i>
<i>1.19</i>	4.22	<i>4.12</i>	0.76	<i>0.78</i>	5.06	<i>5.21</i>	1.12	<i>1.14</i>	3.18	<i>3.28</i>
<i>1.74</i>	6.75	<i>6.58</i>	1.19	<i>1.21</i>	7.85	<i>7.97</i>	1.73	<i>1.71</i>	4.90	<i>4.87</i>
<i>1.29</i>	4.47	<i>4.41</i>	0.80	<i>0.82</i>	5.26	<i>5.41</i>	1.15	<i>1.17</i>	3.29	<i>3.37</i>

Tm	Yb		Lu		Hf		Ta		W	Tl
2	2		2		3		2		20	8
0.63	4.09		0.60		2.74		0.13		0.11	0.007
0.40	2.57		0.38		1.92		0.15		0.09	0.007
0.37	2.39		0.35		1.56		0.07		0.09	0.015
0.42	2.70		0.40		2.08		0.21		0.11	0.008
0.69	4.38		0.65		3.37		0.23		0.09	0.009
0.66	4.25		0.63		3.53		0.36		0.12	0.019
1.15	7.32		1.08		7.53		0.72		0.14	0.026
0.54	3.45		0.51		2.36		0.14		0.06	0.009
0.41	2.61		0.39		1.61		0.06		0.08	0.004
0.64	4.12		0.60		2.78		0.19		0.06	0.008
0.55	3.48	3.72	0.51	0.50	2.70	2.89	0.24		0.04	0.008
0.67	4.18	4.10	0.63	0.60	3.16	3.23	0.18	0.32	1.17	0.011
0.76	4.84	4.78	0.73	0.69	3.84	3.86	0.39	0.29	0.06	0.010
0.55	3.50	3.49	0.53	0.50	2.85	2.98	0.38	0.52	0.07	0.008
1.38	8.93	8.26	1.31	1.24	8.14	7.87	0.65	0.62	0.15	0.016
0.70	4.53	4.22	0.68	0.63	3.59	3.69	0.30	0.88	0.09	0.012
0.64	4.11	3.98	0.61	0.60	3.29	3.36	0.26	0.41	0.04	0.010
1.12	7.11	6.80	1.04	0.99	6.73	6.66	1.36	0.36	0.23	0.027
0.52	3.31	3.18	0.49	0.48	2.20	2.15	0.14	1.35	0.59	0.008
0.79	5.06	4.85	0.74	0.72	4.03	4.18	0.32	0.15	0.07	0.017
0.68	4.36	4.47	0.64	0.65	3.34	3.55	0.26	0.44	0.10	0.009
0.62	3.97	3.97	0.58	0.57	2.97	3.13	0.20	0.34	1.37	0.008
0.67	4.37	4.29	0.63	0.63	3.48	3.56	0.30	0.27	0.80	0.012
0.70	4.47	4.48	0.65	0.64	3.59	3.75	0.29	0.35	1.23	0.012
0.47	3.02	3.17	0.44	0.45	2.05	2.13	0.08	0.48	0.71	0.006
0.73	4.68	4.71	0.69	0.67	3.75	3.74	0.27	0.10	1.39	0.010
0.49	3.13	3.24	0.46	0.46	2.33	2.40	0.16	0.31	0.02	0.008

Pb		Th		U		(La/Sm) _N	Se (ng g ⁻¹)	1 s.d. (ng g ⁻¹)	Te (ng g ⁻¹)
6		5		4					
0.37		0.12		0.04		0.490	180	4	1.99
0.34		0.16		0.05		0.671	158	1	3.19
0.32		0.06		0.03		0.485	176	4	4.10
0.43		0.22		0.06		0.747	167	3	3.06
0.47		0.22		0.09		0.632	177	2	1.61
0.68		0.37		0.14		0.828	186	4	2.23
1.01		1.01		0.37		0.965	170	3	2.68
0.48		0.13		0.05		0.579	174	3	3.06
0.23		0.05		0.02		0.461	165	3	3.70
0.37		0.16		0.06		0.566	194	2	1.95
0.36	6.51	0.21	0.27	0.09	0.10	0.744	166	3	2.45
0.42	0.46	0.15	0.20	0.07	0.07	0.610	168	3	2.33
0.54	1.35	0.37	0.43	0.13	0.16	0.796	176	4	1.43
0.43	0.63	0.33	0.38	0.11	0.14	0.904	194	4	2.76
0.81	1.04	0.63	0.69	0.24	0.25	0.785	193	4	1.68
0.45	0.60	0.24	0.29	0.10	0.10	0.693	198	4	1.97
0.47	0.51	0.25	0.26	0.10	0.10	0.675	187	4	2.47
1.16	1.31	1.44	1.41	0.47	0.43	1.227	219	4	1.16
0.33	0.34	0.12	0.12	0.05	0.06	0.562	174	3	3.32
0.78	0.59	0.29	0.29	0.12	0.12	0.688	210	4	2.07
0.46	0.47	0.25	0.26	0.10	0.10	0.667	195	1	2.21
0.38	0.44	0.18	0.19	0.08	0.08	0.608	193	4	3.17
0.51	0.62	0.26	0.28	0.11	0.11	0.708	186	4	1.97
0.52	0.53	0.25	0.27	0.11	0.11	0.708	199	1	2.20
0.30	0.42	0.06	0.06	0.03	0.06	0.476	168	1	2.63
0.47	0.49	0.21	0.22	0.09	0.09	0.642	194	1	2.26
0.34	0.61	0.13	0.13	0.06	0.12	0.590	180	1	3.12

1 s.d. (ng g ⁻¹)	S (μg g ⁻¹)	1 s.d. (ng g ⁻¹)	Cl (μg g ⁻¹)	Cl/K	δ ^{82/76} Se _{SRM3149} (‰)	2 s.d. (‰)	δ ³⁴ S _{V-CDT} (‰) ^d	1 s.d. (‰) ^d	Radiogenic ^d and stable isotopes
0.06	1171	50	49	0.10	-0.23	0.09	-0.91	0.14	
0.10	938	42	38	0.06	-0.19	0.09	-0.72	0.02	
0.12	940	52	75	0.22	-0.15	0.09	-0.83	0.04	
0.09	932	40	47	0.06	-0.22	0.09	-0.94		
0.05	1351	48	290	0.29	-0.30	0.09	-0.89	0.05	
0.07	1301	33	494	0.31	-0.06	0.09	-0.95	0.01	
0.08	1047	39	2163	0.54	-0.24	0.09	-0.14	0.03	
0.09	1153	44	162	0.32	-0.10	0.09	-0.29	0.03	
0.11	968	26	36	0.14	-0.15	0.09	-0.31	0.01	
0.06	1259	84	75	0.10	-0.21	0.09	-0.65	0.10	
0.07	1116	36	225	0.13	-0.16	0.09	-0.81	0.14	
0.07	1199	24	264	0.26	-0.09	0.09	-0.80		
0.04	1339	47	292	0.19	-0.06	0.09	-0.78	0.04	
0.08	1239	57	266	0.16	-0.15	0.09	-0.77	0.02	
0.05	1550	50	1475	0.71	-0.15	0.09	0.60	0.10	
0.06	1312	105	287	0.23	-0.17	0.09	-0.42	0.03	
0.07	1172	39	281	0.20	-0.22	0.09	-0.83	0.05	
0.03	1755	14	1047	0.24	-0.14	0.09	-0.10	0.08	
0.10	1112	44	223	0.33	-0.15	0.09	-0.80	0.01	
0.06	1471	32	404	0.25	-0.05	0.09	-0.20	0.01	
0.07	1348	21	373	0.26	-0.12	0.09	-0.72		
0.10	1208	37	435	0.52	-0.09	0.09	-1.02	0.01	
0.06	1321	41	335	0.25	-0.10	0.09	-0.70	0.04	
0.05	1340	25	277	0.22	-0.15	0.09	-0.86	0.01	
0.08	1094	22	77	0.15	-0.30	0.09	-0.99	0.30	
0.07	1381	32	514	0.41	-0.13	0.09	-1.11	0.08	
0.09	1244	36	141	0.19	-0.16	0.09	-1.12	0.02	

$^{87}\text{Sr}/^{86}\text{Sr}$	$^{143}\text{Nd}/^{144}\text{Nd}$	$^{176}\text{Hf}/^{177}\text{Hf}$	$^3\text{He}/^4\text{He}$ (R/Ra)	$^{206}\text{Pb}/^{204}\text{Pb}$	$^{207}\text{Pb}/^{204}\text{Pb}$	$^{208}\text{Pb}/^{204}\text{Pb}$
0.702568	0.513135	0.283175	7.6	18.395	15.491	37.916
0.702406	0.513117	0.283170		18.497	15.498	38.093
0.702512	0.513144	0.283173	8.1	18.152	15.453	37.596
0.702407	0.513132	0.283168		18.491	15.507	37.998
0.702502	0.513126		8.0	18.504	15.505	37.987
0.702472	0.513099	0.283144		18.632	15.498	38.074
0.702473	0.513112	0.283149		18.435	15.510	37.968
0.702435	0.513125	0.283171		18.401	15.494	37.862
0.702310	0.513150	0.283235		18.015	15.473	37.506
0.702556	0.513142	0.283204	7.6	18.500	15.497	37.966
0.702422	0.513090	0.283133	7.6	18.822	15.547	38.199
0.702367	0.513134	0.283163	7.7	18.531	15.513	37.942
0.702524	0.513098	0.283135	7.5	18.634	15.504	38.024
0.702483	0.513077	0.283132	7.3	18.796	15.550	38.237
0.702493	0.513092	0.283126	7.1	18.749	15.540	38.168
0.702483	0.513088	0.283125	7.1	18.768	15.544	38.189
0.702465	0.513100	0.283131	7.25	18.726	15.539	38.153
0.702643	0.513035	0.283094	6.1	19.174	15.585	38.634
0.702468	0.513070	0.283102	7.1	18.725	15.539	38.121
0.702504	0.513059	0.283117	7.2	18.798	15.538	38.208
0.702472	0.513060	0.283106	6.8	18.887	15.565	38.311
0.702479	0.513066	0.283112	7.3	18.858	15.580	38.300
0.702516	0.513078	0.283100	7.2	18.809	15.539	38.202
0.702488	0.513082	0.283111	7.3	18.817	15.562	38.236
0.702392	0.513108	0.283145	7.3	18.798	15.549	38.234
0.702479	0.513066	0.283119	7.5	18.724	15.538	38.117
0.702465	0.513108	0.283125	7.2	18.671	15.533	38.039

Supplementary Table S3

Trace element concentrations of BHVO-2 (USGS reference material) analyzed in this study as a quality control standard.

Trace elements	Concentration ^a (ng g ⁻¹)	Uncertainty ^b (%)
Li	4536	1
Be	1019	2
Sc	32716	1
Ti	16994990	2
V	325386	1
Cr	309103	1
Co	45747	1
Ni	119380	1
Cu	125876	1
Zn	100302	4
Ga	21049	1
Rb	9131	1
Sr	397697	1
Y	24508	1
Zr	165858	2
Nb	18450	1
Mo	4114	15
Cd	121	1
Sn	2016	2
Sb	101	10
Cs	96	1
Ba	131906	1
La	15330	1
Ce	37955	1
Pr	5421	1
Nd	24686	1
Sm	6098	1
Eu	2073	2
Gd	6307	1
Tb	944	1
Dy	5308	2
Ho	1012	1
Er	2547	1
Tm	341	2
Yb	1999	2
Lu	278	2
Hf	4302	3
Ta	1151	2
W	229	20
Tl	19	8
Pb	1580	6
Th	1159	5
U	416	4

^a Average concentration of 14 analyses of 6 separate digestions (4 digested together with PAR glasses).^b Expressed as relative standard deviation.